IMPACT OF COSMOLOGICAL SATELLITE GALAXIES ON THE DYNAMICS OF THE MILKY WAY DISC

REZA MOETAZEDIAN

Printed in September 2016
Cover picture: 411 Star Dust, Nila Taylor (2015)
"Even with sails furled, we continue to sail towards the light of the past, to learn our future."

Dissertation
submitted to the
Combined Faculties of the Natural Sciences and Mathematics
of the Ruperto-Carola-University of Heidelberg. Germany
for the degree of
Doctor of Natural Sciences

Put forward by
Reza Moetazedian
born in: Shiraz, Iran
Oral examination: 16 November 2016

IMPACT OF COSMOLOGICAL SATELLITE GALAXIES ON THE DYNAMICS OF THE MILKY WAY DISC

Referees: Prof. Dr. Andreas Just
Prof. Dr. Volker Springel

Abstract

I present a high resolution study of the impact of realistic satellite galaxies, extracted from cosmological simulations of Milky Way-like haloes including 6 Aquarius and one Via Lactea II suites, on the dynamics of the Galactic disc. The initial conditions for the multi-component Milky Way galaxy were generated, to ensure an isolated system in a dynamical equilibrium state. After analysing the statistical properties of the subhaloes, candidates likely to impact the disc with the initial mass, $M_{\rm tid} \sim 10^8 M_\odot$, were identified, inserted into our high resolution N-body simulations and evolved for 2 Gyr. I quantified the vertical heating due to such impacts by measuring the disc thickness and squared vertical velocity dispersion σ_z^2 across the disc.

According to our analysis, the strength of the heating is strongly dependent on the high mass end of the subhalo distribution from cosmological simulations. The mean increase of the vertical dispersion is $\approx 20\,\mathrm{km^2\,s^{-2}\,Gyr^{-1}}$ for $R > 5$ kpc with a flat radial profile. Excluding Aq-F2 results with a very massive perturber $M_{\rm tid}$ [$7 \times 21^{10} M_\odot$, the mean heating is less than $12\,\mathrm{km^2\,s^{-2}\,Gyr^{-1}}$. These heating values correspond to 28% and 17% of the observed vertical heating rate in the solar neighbourhood, respectively. Taking into account the statistical dispersion around the mean, we miss the observed heating rate by more than 3σ. I observed a general flaring of the disc height in the case of all 7 simulations in the outer parts.

The dynamics of the disc in the presence of satellites was also studied in the final two chapters where the selected runs were extended to 4 Gyr. The infall of satellites can be responsible for delaying/advancing the bar-formation, depending on the crossing epoch. The passage influences the bar-formation, if the passage occurs between the end of the shot noise regime T_1 (0.75 Gyr) and before the exponential growth T_2. The Aq-F2 run with the most massive candidate, induces localised vertical heating in the outer disc with $R > 26$ kpc.

I also observed signatures of radial oscillatory behaviour in the outer disc plane, with features similar to that of the Monoceros ring. Disc warping is prominent after 3 Gyr of evolution, reaching $z_{\rm median} \approx 5$ kpc. The asymmetric m [2 mode is dominant for $R > 26$ kpc in the form of vertical motion, with the m [3 mode influencing the rotation of disc particles.

Zusammenfassung

In der vorliegenden Arbeit untersuche ich den Einfluss realistischer Satellitengalaxien auf die Dynamik der galaktischen Scheibe. Die Satelliten wurden aus kosmologischen Simulationen milchstraßenähnlicher Halos entnommen; sechs aus “Aquarius” und einer aus “Via Lactea II”. Die Anfangsbedingungen für die mehrkomponentige milchstraßenartige Galaxie wurden so generiert, dass sie sich wie ein isoliertes System im dynamischen Gleichgewicht befindet. Nach statistischer Analyse der Subhalos wurden solche mit einer Anfangsmasse $M_{\rm tid} \sim 21^8 M_\odot$ ausgewählt, die wahrscheinlich Scheibenebene kreuzen. Diese Kandidaten wurden in die hochauflösende N-Body-Simulation eingef gt und für 3 Gyr simuliert. Ich quantifiziere die vertikale Aufheizung durch solche Interaktionen, indem ich die Scheibenhöhe und das Quadrat der vertikalen Geschwindigkeitsdispersion σ_z^2 messe.

Meine Ergebnisse zeigen, dass die Stärke der vertikalen Aufheizung stark von der oberen Massengrenze der Subhaloverteilung der kosmologischen Simulation abhängt. Der mittlere Anstieg der vertikalen Geschwindigkeitsdispersion ist ungefähr 31 $\mathrm{km^2 s^{-2} Gyr^{-1}}$ für $R > 5$ kpc mit einem flachen radialen Profil. Bei Ausschluss der Resultate von Aq-F2 mit einer sehr massereichen Störgalaxie mit $M_{\rm tid}$ [7 ×$21^{10} M_\odot$ liegt die mittlere Aufheizung bei weniger als 23 $\mathrm{km^2 s^{-2} Gyr^{-1}}$. Diese Werte entsprechen 28% bzw. 17% der beobachteten vertikalen Aufheizung in Sonnennähe. In Anbetracht der statistischen Verteilung um den Mittelwert liegt der aus der Simulation gewonnene Wert um mehr als 4σ unter dem beobachteten. Ich finde ein Flackern der Scheibenh he in den äußeren Scheibenregionen in allen sieben untersuchten Fällen.

In den abschließenden zwei Kapiteln wird die Scheibendynamik unter Einfluss der Satellitengalaxien untersucht, indem die Simulationen auf 5 Gyr ausgedehnt werden. Der Einfall der Satelliten kann eine Verzögerung oder Beschleunigung der Ausbildung des Galaxienbalken bewirken, je nach Zeitpunkt des Durchgangs durch die Scheibe. Der Durchgang beeinflusst die Balkenbildung, wenn er zwischen dem Ende des “shot noise regimes” T_1 (0.75 Gyr) und vor dem exponentiellen Wachstum T_2 geschieht. Die Simulation Aq-F2 mit dem massereichsten Satelliten bewirkt eine lokale vertikale Aufheizung in der äußeren Scheibenregion bei $R > 26$ kpc.

Wir beobachten weiterhin radiale Schwingung in der äußeren Scheibenregion, die den Strukturen des Monoceros-Rings ähneln. Eine Verformung der Scheibe ist nach 3 Gyr nachweisbar und erreicht $z_{\rm median} \gg 5$ kpc. Die asymmetrische m [2 Mode dominiert die Scheibe bei R [26 kpc in Form von vertikaler Bewegung, die m [3 Mode bestimmt die Rotation der Teilchen in der Scheibe.

To my parents,
for all your sacrifices.

تقدیم به پدر و مادرم

به خاطر تمام از خودگذشتنی‌ها

Acknowledgments

As the final touch on my thesis, I would like to dedicate this note to all the people who have supported me throughout the last three and a half years. It would have not been possible to get to this point without you.

I would like to thank my supervisor, Andreas Just, for his continued guidance, encouragement and advice since the start. Also for granting me the trust and freedom to work and follow my instincts at times. I wish to thank Volker Springel for willingly agreeing to referee this thesis. I would like to express my gratitude to Luca Amendola and Thorsten Lisker for accepting to join my examination committee. I am grateful to Andrea Macciò and Volker Springel for providing us with VLII and Aquarius simulation data. Their fruitful comments and discussions, both as part of my thesis committee and also the carried out research, have always been appreciated. Thank you Evgeny Polyachenko for all your helpful comments and discussions throughout our collaboration on the topic of satellite impacts on dynamics of the disc, together with being a generous host. Also, my thanks to Peter Berczik for taking care of our simulation runs and always gladly agreeing to accommodate any concerns or issues regarding the runs.

I must thank Christian Fendt for all his efforts in coordinating the International Max Planck Research School (IMPRS) and providing the chance for students from different institutes to get together. I enjoyed all the social activities, particularly the retreats which we attended every year. Special acknowledgement to the IMPRS '13 generation, it has been a great pleasure knowing you all.

To all my friends, thank you for supporting me during this entire period. My special gratitudes to María Jesús Jiménez, Sara Rezaei Khoshbakht, Peter Zeidler, Clio Bertelli Motta, Anna Schauer, Chiara Mazzucchelli, Veronica Lora, Steffen Brinkmann, Faezeh Shabani, Carolin Wittmann, Alberto Nardin, Steffi Yen, Jan Rybizki and Maria

C. Ramírez. You guys have made Heidelberg a special place for me. Thank you for the great friendships, help, inspirations and every single memory. Also my brilliant officemates over the years: Difeng Guo, Taras Panamarev and Ioanna Koutsouridou. I have enjoyed my time at the ARI, thanks to Avon Huxor, Gustavo Morales, John Vickers and Hendrik Heinl. It has been an absolute blast.

To my parents and brother, Amirpasha, your comfort and love have guided me through this adventurous journey. My dear Roxana, thank you for being there in the last stressful phase of the PhD, putting up with all the complaints. Finally, I would like to thank María Jesús Jiménez, Peter Zeidler, Clio Bertelli Motta, Anna Schauer, Veronica Lora and Roxana Botezatu for proofreading my thesis and all your constructive comments.

This project was funded by the German Research Foundation (DFG) under the Collaborative Research Center SFB 881 "The Milky Way System" through subproject A1/A2. Numerical simulations were performed on the Milky Way supercomputer, which is funded by the DFG SFB 881 subproject Z2 and hosted and co-funded by the Jülich Supercomputing Center (JSC).

"Set your life on fire. Seek those who fan your flames"

- Jalaluddin Rumi

Overview

This thesis summarises the work I have done as part of my Doctorate degree on the topic of satellite galaxies interaction with the Galactic disc using collisionless N–body simulations. The most important aspect of my research has been to investigate the contribution of satellites' infall towards the vertical heating of the Milky Way's disc and the process of bar formation. The properties of the dark matter (sub)haloes, including the host halo, are extracted from cosmological simulations of Milky Way–like haloes (Diemand et al., 2008; Springel et al., 2008).

Chapter 1 is an introduction to the topic, including the cosmology, Milky Way's structure and possible heating mechanisms. The characteristics of the DM subhaloes together with an analysis of their statistics are provided in chapter 2. Section 3.1 includes an overview of the multi–component Model we have used for the purpose of describing the Milky Way and the satellite candidates. Results from the heating analysis and comparison of the measured vertical heating from different simulations are discussed in chapter 3. The role of satellite crossing on delaying or advancing the process of bar-formation is investigated in chapter 4. In addition, localisation of vertical heating due to an infall of Sagittarius-like subhalo has been the focus of chapter 5. Within the framework of this chapter, we also looked into excitation of asymmetric and symmetric unstable modes. The thesis is finalised with a careful summary and outlook (chapter 6).

The majority of chapters 2 and 3, together with certain parts of the introduction and conclusion are published as a paper in (Moetazedian and Just, 2016).

Contents

Listing of Figures

Listing of tables

"Where there is ruin, there is hope for a treasure."

- Jalaluddin Rumi

1 Introduction

1.1 Cosmology

The 21st century can be regarded as the era of precise cosmology. With the success of missions such as Wilkinson Microwave Anisotropy Probe (hereafter WMAP) (Hinshaw et al., 2013) and Planck satellites (Planck Collaboration et al., 2014), we now have very accurate measurements of the parameters, describing the *standard cosmological model* of our Universe. This model is based on Einstein's theory of general relativity (GR), which dates back to 1915. GR is described by a set of 10 field equations (Einstein, 1915). This theory was formulated based on the impact of matter density on the curvature of, so called *space–time*. Prior to this, the Newtonian mechanics was believed to be the only model to describe gravitational laws (Newton, 1687). In the Newtonian model, the Universe is static and flat; as a consequence, the shortest distance between two points in space is always a straight line. However, Newton's laws of gravity failed at describing the dynamics of objects with speeds comparable to the speed of light c and proved to be inconsistent with Maxwell's equations of electromagnetism. Such contradictions motivated Einstein to publish his theory of special relativity (SR) in 1905 (Einstein, 1905), which can be thought of as a special case of general

relativity, where the curvature of space-time due to gravity is insignificant. In other words, SR and GR can be regarded as extensions of Newtonian gravity, in order to include relativistic speeds and high gravitational fields. Only two years after introducing GR, Einstein proposed the static Universe model via applying his field equations and presented the cosmological constant Σ (Einstein, 1917). This quantity was devised in order to prevent the Universe from collapsing under gravity via opposing negative pressure. This work served as the starting point for the field of cosmology.

During the next decade, Friedmann, Lemaître, Robertson and Walker derived a solution of Einstein's field equations, referred to as Friedmann-Lemaître-Robertson-Walker metric (Friedmann, 1922; Lemaître, 1927; Robertson, 1929; Walker, 1935). Such metric would allow for an expanding or contracting Universe. The term 'expanding Universe' was first proposed by Lemaître (1927), and later supported by Hubble (1929). Hubble measured the velocity at which galaxies are moving away from us. He derived a linear relation between the object's distance and the recessional velocity, the so-called Hubble's law. A useful quantity is the redshift z, which is determined by measuring the shift in wavelength of transition lines ,such as Hα, relative to a stationary reference frame. In modern cosmology, the most popular cosmological model of the Universe is the *Big Bang* theory. Lemaître (1931) extrapolated this phenomena back in time and proposed the model in which, the expanding Universe should have started initially as a finite single point. This theory was subject to extensive discussions until 1965, with the discovery of the cosmic microwave background (hereafter CMB) radiation by Penzias and Wilson (1965). They approved the CMB model, first proposed by Alpher, Follin, and Herman (1953). Other phenomena for which the Big Bang theory provides inclusive explanation, includes Big Bang nucleosynthesis (BBN) (Gamow, 1946), Hubble's law and large-scale structure formation. BBN refers to the process responsible for creation of elements heavier than ^{1}H during the early phases of the Universe. The elements that were produced during the primordial BBN, exclusively are ^{4}He, D (^{2}H), ^{3}He, ^{7}Li, T (^{3}H) and ^{7}Be.

The CMB has the form of thermal radiation of a black body and corresponds to the light, which permeates the Universe since the epoch of last scattering. At this point in time when z [2211, photons and baryons (electrons and protons) decoupled due to cooling of the Universe, as a result of expansion (Liddle and

Loveday, 2009). The measured temperature of the CMB is about 2.7 K. According to the cosmological principles, the Universe is *homogeneous* and *isotropic* on large enough scales. Meaning, there are no special places and directions in the Universe. In 1967, Silk (1967) expressed the need for primordial fluctuations in CMB which was soon supported by (Sachs and Wolfe, 1967; Peebles and Yu, 1970; Sunyaev and Zeldovich, 1970). These fluctuations are believed to be responsible for the structure formation we observe today. It was the COBE satellite (Smoot et al., 1992) which provided the first high resolution evidence for the existence of CMB anisotropy. About a decade earlier than COBE results, cosmologists realised that the very small fluctuations in the CMB can not be explained in the presence of only baryonic matter, which can be coupled to the CMB radiation (photons). Therefore, they suspected the existence of an exotic form of matter which does not interact electromagnetically and only experiences gravity (Peebles, 1982). Such a form of matter can collapse under the force of gravity at much smaller density scales than baryons; meaning, the growth of perturbations which have resulted in today's CMB anisotropies have started at much earlier times, compared to a baryonic dominated Universe. Already in 1933, Fritz Zwicky found a discrepancy between the calculated mass of the Coma galaxy cluster, using virial theorem, and the mass derived from the observed luminosity (Zwicky, 1933). The mass, determined from the internal velocity dispersions of cluster members, was a factor of ≈ 400 larger than the observed value, providing an early evidence for the existence of an invisible form of matter. The next step was to determine the characteristics of the "dunkle Materie" (Zwicky, 1933), referred to as *dark matter* (DM). Initially, scientists regarded DM as neutrinos with insignificant mass and capable of reaching speeds close to that of light, and considered to be "hot". This means that all the small scale overdensities would have been wiped out at early times and we would only observe structure formation on scales greater than galaxy clusters. This theory was later overshadowed by the so called "cold" dark matter, which is not relativistic and might be made of supersymmetric particles. This form of DM was able to explain structure formation on different scales. Studies, based on different methods such as weak gravitational lensing effects seen in the case of the Bullet cluster (Clowe et al., 2004), also supported the theory of *cold dark matter* (CDM).

In our current understanding from both theoretical and observational works, we know the Universe consists of four constituents, at the present time: baryonic matter, dark matter, radiation – including neutrinos – and dark energy Σ. The

exact contribution from each component is subject to subtle differences, depending on the observational data set. Yet, the dark energy Σ makes up $\approx 68\%$ of the Universe today; while, baryonic and DM each have a contribution of $\approx 5\%$ and 27% (Planck Collaboration et al., 2015), respectively. These results favour an almost flat observable Universe, dominated by Σ. In 1998, Riess et al. (1998) determined the expansion rate of the Universe using observations of Supernova type Ia (SNIa), and proved that we are living in a Σ dominated Universe with an accelerating expansion rate. This rate is referred to as the Hubble expansion rate H_0, which has a value in the range 68–73 $\mathrm{km\,s^{-1}\,Mpc^{-1}}$. The calculated age of the Universe is about 13.7 billion years old. These measurements are mostly based on analysis of the angular power spectrum, obtained by mapping the CMB temperature anisotropy (Torbet et al., 1999; O'Dwyer et al., 2004) together with BBN observations. CMB is regarded as being highly isotropic, with fluctuations on a 10^{-5} scale. This power spectrum consists of several peaks, corresponding to acoustic oscillations of the CMB. Such oscillations are the result of density perturbations producing standing acoustic waves in the plasma, prior to the decoupling era. features of the power spectrum, such as peak height and angular scale, allows us to determine the matter budget of the Universe together with information about its curvature.

In order to fully describe and quantify the "standard cosmological model", we require a collection of parameters, consisting of: background cosmological parameters, initial conditions parameters and some additional quantities describing the physical effects. The cosmological background parameters are $^{-}$, $^{-}{}_{b}$, $^{-}{}_{m}$ and $^{-}{}_{\Lambda}$, which represent the ratios of total energy, baryonic, matter and vaccum energy (Σ) densities to the critical density ρ_{crit} [$9\pi/4{H_0}^2$, respectively. The Hubble parameter h plays an important role in defining the background cosmology and is determined using distance ladder and SNIa measurements (Riess et al., 1998). This quantity is related to H_0 following, H_0 [h ×211 $\mathrm{km\,s^{-1}\,Mpc^{-1}}$. The total matter budget $^{-}$ [$^{-}{}_{b}$ 0 $^{-}{}_{m}$ 0 $^{-}{}_{\Lambda}$ sets the curvature of the Universe, with $^{-}$ $>$ 2, $^{-}$ $<$ 2 and $^{-}$ [2 corresponding to an open, closed or flat Universe, respectively. $^{-}{}_{b}$, constrained by the comparison of chemical abundance observations in high z gas clouds and primordial BBN models, is important in determining the scale of the acoustic peak amplitudes. In addition, this quantity is solely responsible for measuring the sound speed, which fixes the sound horizon and hence affects the acoustic modes wavelengths. The matter density $^{-}{}_{m}$ is calculated using constraints such as gravitational lensing. This quantity together with $^{-}{}_{b}$ corresponds to the total matter

density $^{-}{}_{0}$, which is essential in deriving the epoch of matter–radiation equality in the form $^{-}{}_{0}h^{2}$ and directly impacts the size of DM fluctuations. The size of the horizon at recombination era ($z \propto 1089$) is solely dependent on $^{-}{}_{0}h^{2}$. This is the epoch after Big Bang when protons and electrons became bound to form neutral H atoms, setting total scale of acoustic oscillations, . The vacuum density $^{-}{}_{\Lambda}$ allows us to measure the expansion/contraction rate of the Universe. Falco et al. (1998) has set an upper limit of $\Sigma \geq 1.8$ on this quantity, using gravitational lensing measurements due to quasars. $^{-}{}_{0}h$ together with Σh are responsible for determining the angular diameter distance to the surface of last scattering. On the other hand, the initial conditions parameters include: the power law index n, corresponding to the initial adiabatic density fluctuations, the fluctuations' amplitude Q and few more parameters. Studies of CMB have shown n to have a value close to unity. Fig. 1.1.1 shows the acoustic temperature power spectrum of CMB, measured by (Planck Collaboration et al., 2015). Other physical parameters include, considerable neutrino mass m_{ν}, number of neutrinos N_{ν} and reionization redshift z_{r}. During the Reionization epoch which was completed around z [7 (Becker et al., 2001), the transparent Universe was re–ionized as objects collapsed and released energy, ionizing neutral Hydrogen atoms. Observations of Lyman–α forest – series of absorption lines – in distant quasars' spectra, indicate the presence of neutral H atoms/clouds.

1.1.1 Cosmological simulations

In the Σ cold dark matter (ΣCDM) Universe, smaller overdensities collapse under gravity earlier than their more massive counterparts, and form DM substructures. The most well known theory which describes the conditions for collapse of density perturbations to first approximation, is the *spherical top–hat collapse* model. During the matter dominated era, fluctuations grow linearly with the expansion of the Universe which scales as $t^{2/3}$ with time (Padmanabhan, 1993). Once the linear overdensity, $\delta =)\rho_{m}$ $\not{k}_{m} + \not{k}_{m}$, has reached a value of 1.68, the *turnaround point*, the expansion stops and the perturbation collapses non–linearly under self–gravity. Here $\not{k}_{m}$ refers to the mean matter density within a given radius and ρ_{m} being the density at that radius. Instead of theoretical collapse to an infinite density point, the overdensity reaches a virial equilibrium state. Virialisation occurs, once the kinetic and gravitational energy satisfy the virial condition $|U| = 2K$. The density contrast at the virial point is Λ [$\rho_{m}/\not{k}_{m} \gg 178$. However, in our Σ dominated Universe, it

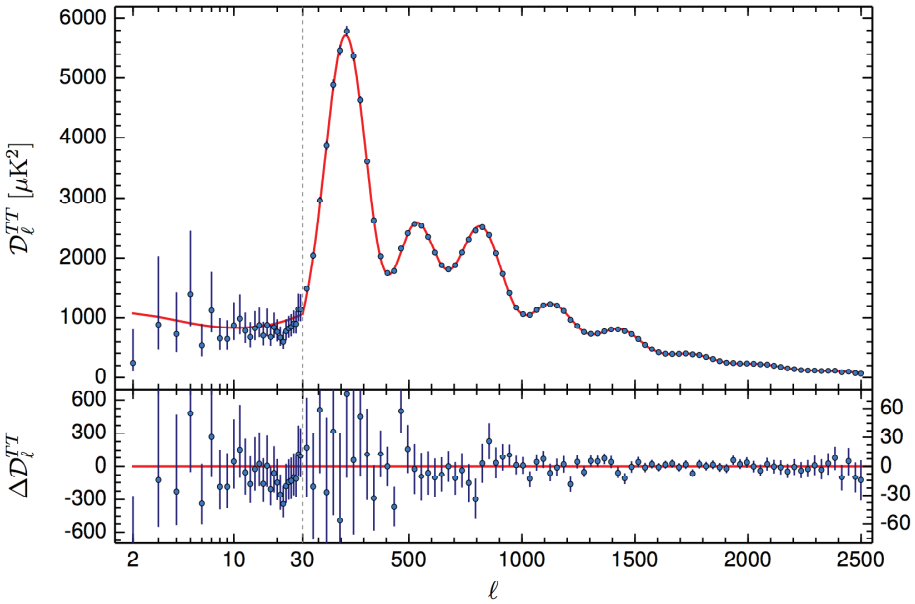

Figure 1.1.1: Acoustic temperature power spectrum of the Cosmic Microwave Background (CMB), measured by Planck (Planck Collaboration et al., 2015). The residuals with respect to the best fitted model are shown in the bottom panel.

is unrealistic to assume that only matter is driving the perturbation collapse. Also, such overdensities are most likely to have non-spherical geometry. Therefore, we require a more comprehensive theory in order to explain structure formation. These bound DM substructures are referred to as *subhaloes*, which are residing within another halo. According to the ΣCDM model, structure formation in the Universe follows a hierarchical scenario; where dark matter halo growth occurs via the infall of smaller systems (e.g. White and Rees 1978; Moore et al. 1999). In 1976, Schechter (1976) proposed a distribution function, describing the number density of galaxies as a function of luminosity/stellar mass. This important quantity provides us with a statistical measure of galaxies distribution in the Universe. Fig. 1.1.2 shows the cosmic timeline from the Big Bang to the Universe today.

The development of numerical approaches, together with observations of high redshift objects in the last decade has expanded our knowledge of structure formation. Currently, using numerical hydrodynamic techniques, cosmologists are able to model galaxy formation in the ΣCDM context. In principle, the Universe can be represented as a set of point masses which interact with each other via the force

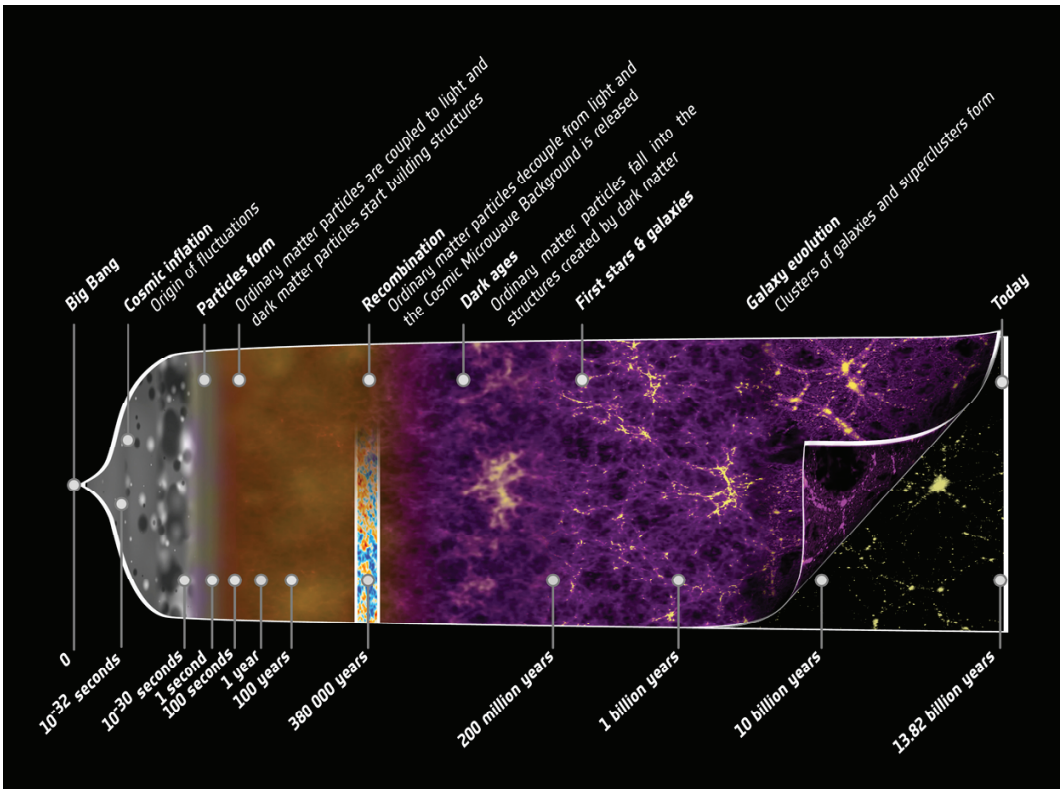

Figure 1.1.2: Cosmic timeline of our Σ dominated Universe. Image credit: ESA and the Planck collaboration.

of gravity and the motion of these particles is integrated in time, starting at some higher redshift. A sufficient particle number is required in N-body simulations, in order to avoid pair–wise interaction between particles and to make sure the systems reside in a dynamical equilibrium, i.e. two–body relaxation time $\tau_R \rightarrow$ crossing time τ_c (Binney and Tremaine, 2008),

$$\tau_R \gg \frac{N}{7\,ln\,N}\tau_c, \tag{1.1}$$

$$\tau_c \gg) G\not{\rho}+^{-1/2}, \tag{1.2}$$

where N represents number of particles. There exist different methods for calculating the gravitational force by solving Poisson's equation, such as particle–based and particle–mesh. In the particle–mesh approach, the potential is determined via a Fourier transformation of density within each grid cell (Hockney and Eastwood,

1988). In the particle–based tree code, the force from distant particles is approximated using their multipole moments with some opening angle of the tree and a force softening length ϵ (Barnes and Hut, 1986). An example of a N–body code which employs both approaches is the GADGET-2 (Springel, 2005). The process of identifying bound subhaloes in the simulations is performed using different algorithms such as "friends–of–friends" (FOF) (Davis et al., 1985), 6–dimensional phase–space based method (Diemand et al., 2006) and SUBFIND (Springel et al., 2001). Millennium I simulation with 10 billion dark matter particles (Springel et al., 2005b) is regarded as one of the largest cosmological simulations ever carried out with the aim of understanding galaxy formation and evolution using GADGET-2. This simulation had a cubic box of side length $500h^{-1}$ Mpc and a $5h^{-1}$ kpc spatial resolution. The follow–up Millennium II simulation (Boylan-Kolchin et al., 2009) with 125 times better mass resolution, due to a smaller box size, provides a more accurate picture of galaxy evolution over a more extensive redshift and mass range.

However, these simulations together with implemented *semi–analytical models* (SAM) fail at reproducing the observed abundance of haloes with $M_h < 10^{11} M_\odot$, also known as the "missing satellites problem". In other words, more DM subhaloes are formed in simulations for this mass range, than observed in the Local Group (Loveday et al., 1992; Kauffmann et al., 1993; Klypin et al., 1999). With the debut of hydrodynamical codes and improved SAMs, some of the discrepancies between observations and cosmological results can be tackled. The hydrodymaical codes allowed for inclusion of baryonic physics on different scales; including feedback processes, black hole growth, star formation and the Interstellar medium (ISM). It has been concluded that supernovae feedback (Governato et al., 2007; Brooks et al., 2013) together with reionization (Okamoto et al., 2008) are capable of reducing the previously measured slope of the luminosity function from $\alpha_{\rm H} \approx$-2 , close to the observed value of $\alpha_{\rm g} \propto$-1.3.

There exists two main approaches in hydrodynamical codes for solving Euler equations joined by non-relativistic ideal gas equation of state: Lagrangian and Eulerian methods. The most famous of the former is Smooth Particle Hydrodynamics (SPH) code (see review by Springel 2010). An example of a classic SPH code is GASOLINE (Wadsley et al., 2004), while Springel (2005) developed an entropy–conserving variant of the method. In the case of the second approach which relies on grid cells for solving hydrodynamic–equations, Adaptive Mesh

refinement (AMR) technique is the most well–known with examples such as RAMSES (Teyssier, 2010) and H-ART (Kravtsov et al., 1997) codes with sub–grid resolution. In addition, the AREPO code developed by Spriangel (2010) takes advantage of both Eulerian–Lagrangian methods and uses a Voronoi tesselation for dividing the space around particles. For a more detailed overview of numerical hydrodynamical codes see e.g. Somerville and Davé (2015).

Cosmological simulations are carried out, starting from a set of initial conditions set by the specified cosmology and generated as a linear matter power spectrum (Eisenstein and Hu, 1999). The power spectrum is randomly sampled for modes and advanced forward in time according to the Zel'dovich approximation in a cubic simulation box (Bertschinger, 1998). In order to study the evolution of galaxies in high resolution, we benefit from the *zoom* simulation technique. This approach involves re–simulating a region of interest at higher resolution while keeping the surrounding regions at lower resolution, which is computationally cheaper. Therefore, the particles corresponding to the region of importance are tracked back to the starting redshift and simulated with higher resolution, including sub-grid hydrodynamical physics. Zoom cosmological simulations such as Aquarius (Springel et al., 2008) and Via Lactea (Diemand et al., 2007) are aimed at representing a Milky Way–size halo and its subhalo distribution.

Formation of disc galaxies has been a long–term challenge for cosmological simulations. Prior analytical works of disc formation (Mo et al., 1998) have shown that the accreted gas from a DM halo with conserved specific angular momentum $\boldsymbol{j}$ can settle into a disc. However, observations of spiral galaxies have proven to be rather complex interplay between angular momenta $\boldsymbol{j}$ of different strength, which contradicts the picture depicted by theoreticians (Bullock et al., 2001). Earlier simulations suffered from excess removal of high $\boldsymbol{j}$ during disc formation process (Steinmetz, 1999), resulting in compact disc galaxies. More accurate star formation feedback recipes (Governato et al., 2007) have played a major role in ejection of low $\boldsymbol{j}$ and maintaining the galaxy's gas reservoir; hence, more realistic late–type spirals are now formed (Christensen et al., 2014; Vogelsberger et al., 2014).

1.2 The Milky Way as a typical spiral galaxy

The Milky Way galaxy (hereafter MW) is part of the Local Group of galaxies which consist of more than 50 members; the majority are dwarf galaxies. The MW and M31 (Andromeda) are the most massive members, located $\approx$ 800 kpc apart. The Local Group has an estimated size of 3 Mpc. Our Milky Way is regarded as a barred Sc/Sbc spiral galaxy which consists of three components: disc, bulge and halo. Fig. 1.2.1 is a schematic diagram of our Galaxy where different features such as the thin and the thick discs, central nucleus, and Globular clusters (GCs) can be seen. The MW is believed to be around 13 billion years old; this is mostly based on determining the age of Globular clusters in the halo which are among the oldest bound structures in the Universe and hosting second generation of stars (Sparke and Gallagher, 2007). Our Galaxy contains few hundred billion stars which are distributed mostly in the disc and the bulge. The MW is considered to have not experienced a major merger with another comparable galaxy in the last 8-10 Gyr. In addition to stars, our Galaxy also contains dust and gas components. The presence of dust in the inner regions composes a great challenge in observing the Galactic centre. Fig. 1.2.2 shows an artist's impression of the MW viewed face–on; position of the Sun is marked and some of the well-known features of the Galactic disc are visible, such as the spiral arms and the bar.

Understanding the Milky Way is important, in order to have a better insight of other galaxies. Our Galaxy is regarded as a typical spiral. This allows us to study different aspects of astronomy, such as feedback processes, star formation, galaxy evolution, turbulence etc., on different physical scales, ranging from few to thousands of parsecs. In the last decade, many observational surveys have been conducted to study our Galaxy: SDSS, APOGEE, SEGUE, RAVE and Gaia–ESO (York et al. 2000; Steinmetz et al. 2006; Yanny et al. 2009; Gilmore et al. 2012; Alam et al. 2015). The latest Gaia mission which was lunched in 2013, is expected to deliver its first set of results in September 2016. In the following subsections, different constituents of the MW are described.

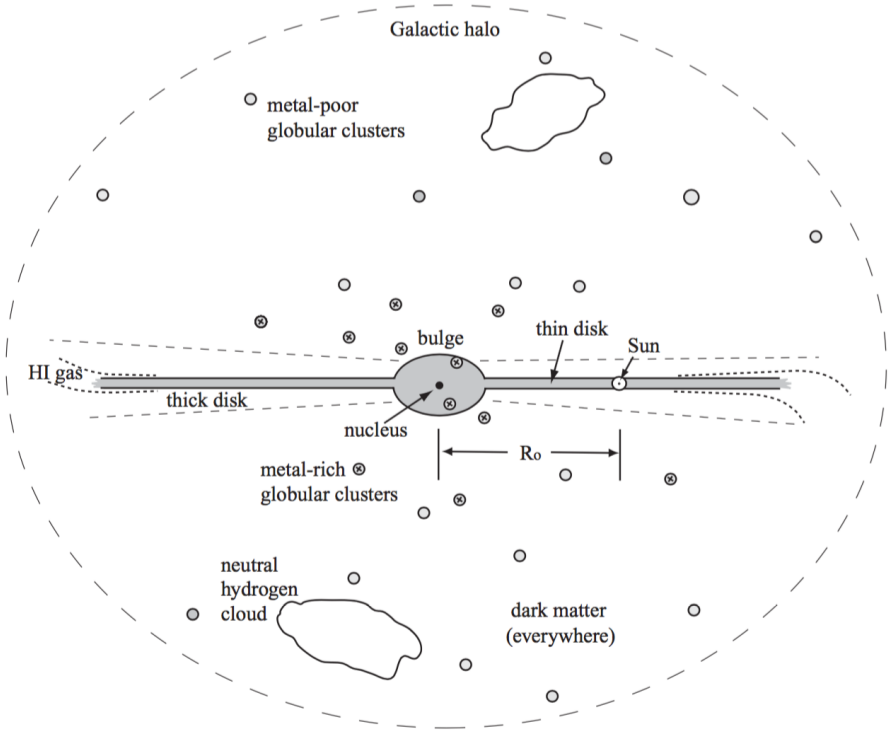

Figure 1.2.1: Schematic diagram of the MW, including different components and members of our Galaxy (Sparke and Gallagher, 2007).

1.2.1 The halo

The halo consists of two major constituents: stellar and dark matter haloes. In order to understand the large–scale gravitational potential of our Galaxy, investigating the halo is essential. A two-component stellar halo resides in the inner ≈ 30 kpc, while the DM component extends to 200–300 kpc. The transition between the inner and outer stellar halo occurs at around $25 \equiv 10$ kpc (Watkins et al., 2009; Deason et al., 2011).

The stellar halo contains $\approx 1\%$ of the MW's stellar budget. The formation of this component can be a result of complex interplay of different scenarios, including accretion of tidally disrupted satellite galaxies (Ibata et al., 1997), *in–situ* formation (Abadi et al., 2006), ejection of disc stars into the halo and star formation from the stripped gas of accreted galaxies (Font et al., 2011; McCarthy et al., 2012; Cooper et al., 2015). The stars are metal–poor with high velocity dispersions. The calculated mean rotation has a value of $\propto 40$ km s^{-1} (Bond et al., 2010). This

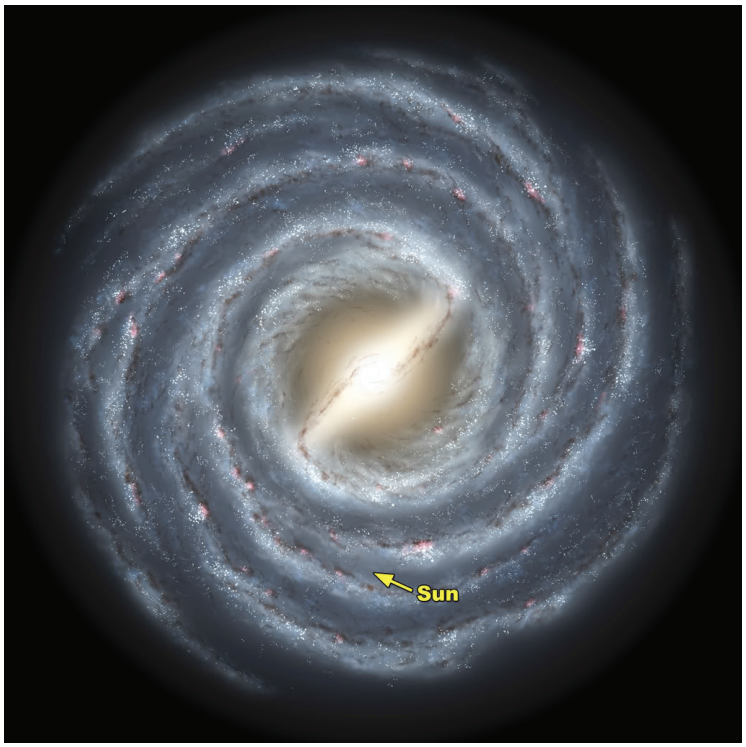

Figure 1.2.2: Artist's concept of our Galaxy viewed face–on with position of Sun marked (≈ 8 kpc). Image credit: NASA JPL

component is measured to be flattened and have an oblate geometry with $q \approx 0.65$ as shown by Jurić et al. (2008). The density profile which explains the distribution of the stellar halo stars has a double power–law shape with a steeper gradient in the outer part (Faccioli et al., 2014). Deason et al. (2011), using the SDSS data, have proposed a stellar mass of $\approx 3 \pm 10^8 M_\odot$. Globular clusters are important features of the MW halo, that allow the observers to determine the characteristics of our Galaxy, such as the formation history. The GCs in the outer stellar halo are metal–poor in comparison to the ones residing in the inner stellar halo (Brown et al., 2004).

The dark matter halo's density profile can be described by the well–known Navarro–Frank–White profile (Navarro et al., 1997) which has a cuspy inner shape. The profile has a scale length of $\gg$25 kpc and a concentration of 10 (van der Marel et al., 2012). The measured mass of the DM halo $M_{200} \approx 1\text{–}2 \pm 10^{12}\ M_\odot$, which corresponds to the mass enclosed within the radius r_{200} with average density 200 times the critical density of the Universe $\rho_{\rm crit}$. The Galactic DM halo is rounder compared to the stellar part with a flattening $q = 0.8 \equiv 0.1$ (Xue et al., 2015). The

estimated total baryonic mass fraction $f_{\rm baryon}$ of the Milky Way is about 6% which is almost a factor of 2.5 smaller than the universal value (Hinshaw et al., 2013). Bland-Hawthorn and Gerhard (2016) provide a more detailed discussion about the Galactic halo.

1.2.2 The bulge

The MW bulge component is located at the centre of our Galaxy and dominates the light/matter budget for the inner $\approx$ 2 kpc. It has an estimated mass of $\gg 3 \pm 21^{10} M_{\odot}$ (Picaud and Robin, 2004; Valenti et al., 2016). Persic and Salucci (1992) have shown that 25 % of the Universe's stellar luminosity originates from bulges of spiral galaxies. Hence, a comprehensive insight of this component is key to understanding galaxy evolution. We are capable of examining the Galactic bulge structure to great details in contrast to extragalactic counterparts; since we have access to the fully resolved stellar populations residing in this component.

Due to the dust extinction in the Galactic centre, the infrared wavelength provides the best window for observing the bugle. The results obtained from COBE satellite's observations in infrared (Weiland et al., 1994; Smith et al., 2004), prove the existence of a bar in the centre. The presence of this bar was proposed initially by de Vaucouleurs (1964), Sinha (1979) and Blitz and Spergel (1991). The bar is a flattened structure with axis ratios 1:0.4:0.3, where the major axis is lying in the Galactic plane with a radial extent of 3–3.5 kpc (Bissantz and Gerhard, 2002). It rotates with a pattern speed $^{-}{}_{\rm p} \approx 61$ kms^{-1}Gyr^{-1} (Gerhard, 2011). The bar is expected to have been formed due to disc instabilities and following a secular evolution path. It resulted in formation of boxy–peanut B/P bulge, also referred to as a *pseudo–bulge* (e.g. Dwek et al. 1995; Debattista et al. 2005; Howard et al. 2008). This is in contrast to the theory of a classical bulge which has been formed via mergers with external satellite galaxies (Elmegreen, 1999). The bulge stars possess high velocity dispersions ($>$ 211 kms^{-1}) compared to rotation, $V_{\rm max}/\sigma$ [1.76 (Minniti and Zoccali, 2008). According to spectroscopic and photometric surveys, the bulge's metallicity supports the argument of a multi–component bulge (Ness et al., 2013; Rojas-Arriagada et al., 2014); with metallicities ([Fe/H]) ranging from -1.0 to 0.4 with a peak at the solar metallicity (Zoccali et al., 2006). Also, the centre of the bulge hosts a supermassive black hole (SMBH) Sagittarius A* with an approximate

mass of $5 \pm 21^{6} M_{\odot}$ (Gillessen et al., 2009). A more detailed overview of the bulge is discussed in the review by Gonzalez and Gadotti (2016).

1.2.3 The disc

The Galactic disc contains the majority of baryonic matter (stars and gas) in our Galaxy. The disc extends out to at least 15 kpc radially and 1 kpc vertically – perpendicular to the disc plane. The Sun lies at a distance of 8 kpc from the Galactic centre (Gillessen et al., 2009; Reid et al., 2014) and slightly above the plane, in the region referred to as the *solar neighbourhood*. The disc is rotating clockwise, if viewed from the Galactic north pole, with a circular speed of 240 kms^{-1} at the solar position (Reid et al., 2014). The Galactic disc shows slight deviation from axisymmetry in the plane, while commonly it is assumed that the vertical component of angular momentum $\boldsymbol{L}_z$ together with the total energy E are conserved quantities. The motion of stars in the disc can be decomposed into three components in cylindrical coordinates ($\boldsymbol{v}_{\mathrm{R}}$, $\boldsymbol{v}_z$, $\boldsymbol{v}_\phi$). The measured velocity dispersions, σ_{R}, σ_z and σ_ϕ in the solar neighbourhood for the three components are $(32.4\,,\ 18.1\,,\ 23) \equiv 1.2\mathrm{kms}^{-1}$, respectively (Fuchs et al., 2009). The calculated surface density of the disc at solar neighbourhood has a value of $\Omega_{\mathrm{d}} \propto 5 \rightleftharpoons M_{\odot}\ \mathrm{pc}^{-2}$ (Flynn et al., 2006; Kuijken and Gilmore, 1989; Just and Jahreiß, 2010), and the estimated mass of MW disc is $M_{\mathrm{d}} \propto 5.6 \pm 21^{10} M_{\odot}$ (Flynn et al., 2006).

Gilmore and Reid (1983) first noticed the presence of two density distributions in the disc, and proposed the idea of MW disc being composed of a thin and a thick disc component (Fig. 1.2.1). These distributions can be described as an exponential profile. The corresponding scale heights z_0 for the thin and thick discs are 300 and 900 pc, respectively (Jurić et al., 2008; Siegel et al., 2002). Radial scale lengths h of 2.6 and 2 kpc are assigned to the two constituents (Jurić et al., 2008; Bovy et al., 2012b). Observations have shown that the thin disc is metal–rich, while having lower abundance of metals lighter than iron (Fe), also known as α–elements (Ivezić et al., 2008). During the stellar evolution phase, massive stars exhaust their fuel first and explode as Supernovae Type II, enriching the surrounding Interstellar Medium (ISM) with α–elements such as O, Ne, Mg and Si. It is only until the SNIa explosions, that the ISM is iron–enriched. Nowadays, different observations and models have shown that we require a combination of Fe yields from both SN

types in order to explain the current chemical budget, with 1/3 Fe contribution from SNII. Therefore, the metal–poor thick disc is older than its thin companion. As we move away from the disc plane, a decline in the metallicity is observed (Bovy et al., 2012b). Furthermore, the thick disc is considered to be dynamically hot, due to stars having higher velocity dispersions than the cold thin disc stars. The thin component contains more than 80 % of the total disc stars. The theory of a sharp distinction between the two disc components (Lee et al., 2011), or rather a smooth transition between different sub–populations (Bovy et al., 2012a), has been subject of intense discussions in the past few years.

Another important aspect of our Galactic disc are spiral arms. These features are regarded as transient density waves, responsible for the transport of material from the outer disc to the inner regions. The majority of the MW's star formation takes place inside these spiral arms, where high gas pressure and turbulence result in gas collapse. Comparing features of our Galaxy with other late–type spirals, we come to the conclusion that the Milky Way is a fair representative of disc galaxies. For example, the increase of vertical thickness with the sub–population's age is also observed in other late–types such as IC 2531 (Wainscoat et al., 1989), NGC 5907 (Just et al., 2006) and many others (de Grijs and Peletier, 2000).

1.3 Heating of the Galactic disc

High-resolution cosmological simulations have demonstrated that DM substructures survive within environments similar to the Milky Way (Moore et al., 1999). Galaxy mergers are believed to be the main drivers for significant kinematical perturbations of galaxies (Toomre and Toomre, 1972), and can be classified into three categories: major, minor and infall of satellites. With regards to theoretical (Hernquist, 1992) and observational evidences, (e.g. Woods, Geller, and Barton 2006; Woods and Geller 2007) "major" mergers (mass ratios $\gtrsim$ 1:3 of total galaxy mass) strongly perturb the system and can even change the morphology. However such events are less common compared to "minor" mergers with masses in the range 1:3 to 1:50 of the total mass (1:1 of disc mass) which are likely to destroy thin discs (Kazantzidis et al., 2008). The third type, which forms the basis of this study, is the interaction of satellite galaxies with intermediate mass ratios which are more commonly represented in units of the disc mass ($\lesssim$

1:10 of disc mass). Our Milky Way galaxy has been experiencing such mergers; observations of stellar tidal stream remnants provide evidence for such encounters (e.g. Ibata, Gilmore, and Irwin 1994; Majewski et al. 2003; Martínez-Delgado et al. 2005). Understanding the evolution of disc galaxies has challenged both observers and theorists for the past decade. There have been numerous attempts at bridging the observed characteristics of spiral galaxies and their violent history (e.g. Navarro et al. 1994; Abadi et al. 2003). Some of the early studies, including that by Moore et al. (1999) have indicated that interaction of substructures with galactic discs could induce heating processes resulting in thickening of the disc. Also, the ΣCDM scenario predicts a continuous infall of subhaloes; this includes massive satellites, which are expected to impact the dynamics of the stellar disc significantly (Stewart et al., 2008). However, early observations of our solar neighbourhood have found the presence of a 10 Gyr old "thin" disc with a scale height less than 500 pc (e.g. Kent et al. 1991; Dehnen and Binney 1998; Just and Jahreiß 2010).

The survival of a thin disc in the (ΣCDM) Universe has been tested through early analytic models (e.g. Tóth and Ostriker 1992; Sellwood et al. 1998) together with N-body/hydrodynamical simulations (e.g Quinn and Goodman 1986; Quinn, Hernquist, and Fullagar 1993; Walker, Mihos, and Hernquist 1996; Velázquez and White 1999; Sommer-Larsen, Götz, and Portinari 2003). One of the major shortcomings of analytical approaches was the choice of nearly circular satellite orbits. This is not in agreement with the ΣCDM results, where eccentric orbits are favoured (Ghigna et al., 1998). Another disadvantage was the use of a rigid potential for the host halo, the disc and/or the bulge instead of live components. Rigid potentials suppress the effect of interactions between the halo and the disc, as well as the dynamical friction – and hence transfer of angular momentum – between different components, as the satellites spiral towards the centre. Velázquez and White (1999) have shown that using a rigid potential instead of a live halo overestimates the heating of the galactic disc by a factor of 1.5-2. Early numerical simulations suffer from an unrealistic high abundance of substructure compared to the ΣCDM cosmology prediction.

Observations of the local stellar kinematics have suggested multiple scenarios for the evolution of the thin disc. The most useful observational quantity in order to investigate the evolution of our Milky Way disc is the so-called "age-velocity dispersion" relation. This relation is aimed at connecting the stellar kinematics

with their dynamical history and providing constraints on the vertical structure of the Galactic disc. Nordström et al. (2004) and follow-up studies (e.g. Holmberg, Nordström, and Andersen 2007, 2009) have favoured a picture in which the disc has experienced continuous heating through its lifetime. Another possible scenario is the saturation of vertical heating of stars older than 4.5 Gyr, as suggested by an analysis of the Geneva-Copenhagen survey (Freeman, 1991; Seabroke and Gilmore, 2007). This survey provided ages, metallicities and kinematics for ≈14,000 G and F dwarfs in the solar neighbourhood, with absolute magnitudes V brighter than ≈ 9.4. The results of Holmberg et al. (2009) benefit from the Hipparcos data (Perryman et al., 1997) which greatly improved the parallaxes and consequently reduced the uncertainties; this resulted in clear continuous heating pattern. Holmberg et al. (2009) fitted power laws to the radial, tangential, vertical and total velocity dispersions of ∼ 2600 F and G dwarfs in the solar neighbourhood and derived power law exponents of $\gamma = 0.39$, 0.40, 0.53 and 0.40 for these respective quantities. Fig. 1.3.1 shows the age–velocity dispersion plot from Holmberg et al. (2009), where σ_U and σ_W correspond to the radial and vertical velocity dispersions in the solar neighbourhood, respectively. Other disc galaxies also show signs of dynamical heating; a good example is the edge–on galaxy NGC 5907. Just et al. (2006) presented an evolutionary model for this galaxy with a slightly declining star formation rate and a continuous dynamical heating for young population which is slower than the observed value in the solar neighbourhood.

More recent simulations (e.g. Font et al. 2001; Ardi et al. 2003; Kazantzidis et al. 2008; Read et al. 2008; Villalobos and Helmi 2008; Kazantzidis et al. 2009) have shown that infall of satellite galaxies could result in either destroying or greatly heating the disc, forming a *thick* component; this contradicts our picture of the Milky Way thin disc component. It is important to note these analyses focussed on the impact of satellites at the massive end of the substructure spectrum, with masses greater than 5 $\pm 21^9 M_\odot$. For instance, Read et al. (2008) concluded that accretion of a satellite with a mass comparable to the Large Magellanic Cloud (LMC) of 10^{10} $M_\odot$ is sufficient to explain the thick disc formation. Also Moster et al. (2010) examined the role of a gas component in the disc instability and found that for a gas mass fraction of 25 percent, the thickening of the disc could decrease by 20 percent – thus suppressing vertical heating. In addition to galaxy mergers, other proposed mechanisms are expected to contribute towards the heating:

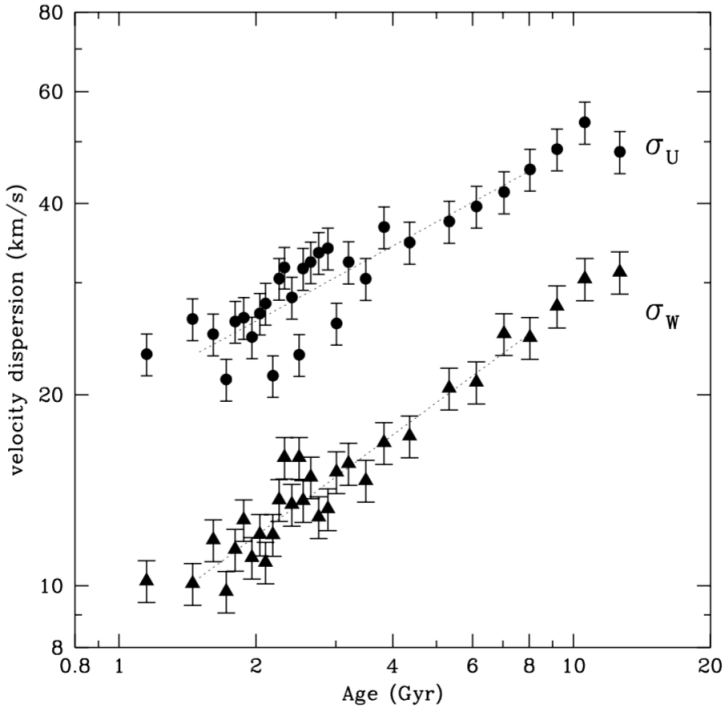

Figure 1.3.1: Velocity dispersion of stars in the solar neighbourhood as function of their estimated age from the Geneva–Copenhagen survey (Holmberg et al., 2009). σ_U and σ_W correspond to the radial and vertical velocity dispersions, respectively.

- Carlberg (1987) and Sellwood (2013) studied the induced changes of the disc's phase-space distribution due to transient spiral waves and concluded that such structures are able to increase the velocity dispersion of stars, although mostly in the disc plane. Since the vertical oscillation frequency ν of stars in the plane is high relative to the frequency at which stars encounter the density waves, such spirals are inefficient at increasing the vertical motion of stars.

- Coherent bending waves are more effective at vertical heating than spiral arms. In principle, such waves could travel across a disc until reaching vertical resonance (Toomre, 1983; Sellwood et al., 1998). At this point, the wave's energy could transfer into increasing vertical velocity dispersion of local stars. However, Araki (1985) has shown that such a mechanism is more likely to take place within discs with velocity ellipsoids more flattened than observed in our solar neighbourhood, $\sigma_R \gtrsim 4\,\sigma_z$.

- Scattering due to massive gas clumps, e.g. Giant Molecular Clouds (GMCs),

is another possible heating scenario. Lacey (1984) demonstrated that such clumps are capable of redirecting the motion of disc stars towards the outer plane; however they fail at increasing the dispersions.

An overview of possible disc heating mechanisms are discussed in the review by Sellwood (2014). In addition to the vertical heating, Quillen et al. (2009) and Bird et al. (2012) showed that the infall of satellites could also induce radial migration in MW-like systems with greater impact at larger radii, while Minchev et al. (2012) and Vera-Ciro et al. (2014) concluded that radial migration has minimal impact on the thickening of the MW disc. The radial migration as a result of mergers reduces the disc flaring (Minchev et al., 2014) which provides an opposite picture to the measured one, especially in the outer parts, in the absence of external perturbations as demonstrated by Minchev et al. (2012). Based on the perturbation theory, Vesperini and Weinberg (2000) have shown that the energy deposit in the perturbation by satellites, scales as the square of the satellite mass, and that in the resonance situation, minor mergers may have a measurable impact on the host galaxy. In a cosmologically based hydrodynamical simulation, Gómez et al. (2016b) have shown that even a distant encounter of a satellite galaxy with M [$5 \pm 21^{10} M_{\odot}$ ($\approx$ 5 per cent of the host galaxy mass) at R [91 kpc can perturb the outer disc at $R > 23$ kpc significantly and form a Monoceros ring-like warp.

Within the framework of this study, we use high-resolution N-body simulations (Bien et al., 2013) to investigate the impact of accreting satellite galaxies on the dynamics of our Milky Way "thin" disc and answer the question: are we able to explain the observed heating of the Galactic disc in the presence of the infall of satellites? For realistic conditions, the initial conditions (ICs) of our satellites follow that of the ΣCDM model (Springel et al., 2008). The interactions of satellites and the stellar disc have the potential to trigger different types of both small and global scale perturbations, such as initiating modes in the Galactic disc. Hence, for a deeper understanding of such distortions in the phase-space distribution of disc stars, we require simulations that are capable of resolving the dynamics down to few tens of *parsecs* scale; a resolution much higher than most current Milky Way interaction analysis simulations. We employ multi-component models for our Milky Way which enable us to use both observational and cosmological constraints for modelling our Galaxy (Yurin and Springel, 2014).

This work improves the current knowledge of the impact of subhalo interactions on the observed vertical structure of our Galactic disc. Such a structure is the result of a complex interplay of different heating mechanisms. Since we do not yet know about the exact contribution from each of such mechanisms, quantifying one method will provide a more accurate picture of other processes. For the first time, we have analysed and compared the impact of subhaloes from Aquarius and Via Lactea II Milky Way-like simulation suites (e.g. Springel et al. 2008; Diemand et al. 2008) to provide a statistically valid study of satellite impact on the vertical structure of the stellar disc of our Galaxy. In addition, having initial conditions for the MW, in a much better equilibrium state compared to previous works, allows us to minimize the bias effects. Such effects could overshadow the expected real heating measurements. The combination of 40 pc vertical resolution together with ICs in a robust equilibrium state differentiates this analysis compared to previous studies. This allows minor vertical heating effects to be measured and distinguished from other processes (Moetazedian and Just, 2016). Also, such an impact could result in excitation of unstable modes in the disc plane. These include the bar mode or asymmetric perturbations which are typically observed due to satellite passages (Gómez et al., 2016b).

"Yesterday I was clever, so I wanted to change the world. Today I am wise, so I am changing myself."

- Jalaluddin Rumi

2

Dark matter subhaloes statistics

For a realistic picture of the interaction between satellite galaxies and the Milky Way's thin disc, we have extracted the distribution of subhaloes from two suites of cosmological simulations: Aquarius and Via Lactea II (e.g. Springel et al. 2008; Diemand et al. 2008). The major difference between the Aquarius and the Via Lactea II (hereafter VLII) lies in their adopted cosmology, which in the case of Aquarius are the WMAP one-year results (Klypin et al., 1999), while for VLII WMAP three-year results were used. Hence the value of σ_8, which represents the amplitude of the (linear) power spectrum on the scale of 8 h^{-1}Mpc, is lower for VLII. This parameter plays a crucial role in the context of influencing structure growth at early epoch. Also n_s corresponds to the spectral index of scalar fluctuations (Table 2.1.1) and is close to being scale-invariant. The value for $^{-}{}_{m}$, σ_8 and n_s are smaller for VLII compared to Aquarius which might impact the substructure distribution at the very low mass end.

2.1 Host dark matter halo properties

The Aquarius suite consists of a set of 6 simulations; each associated with a

Table 2.1.1: The cosmological initial conditions

Cosmological Suite	$^{-}{}_{\mathrm{m}}$	$^{-}{}_{\Lambda}$	σ_8	$\mathrm{n_s}$
Aquarius	0.25	0.75	0.9	1.0
VLII	0.238	0.762	0.74	0.951

different realisation of DM halo likely to host a Milky Way-like galaxy and which has not experienced a recent major merger. The haloes are chosen from a parent halo of homogeneous resolution. These simulations are performed in cubic box with side length of 137 Mpc while VLII is performed in a smaller box of length 40 Mpc. The second highest resolution set of Aquarius simulations "Aq-A2××Aq-F2" are employed for this analysis. In our study we use the $z=0$ snapshots from all the above simulations, which resemble the present day distribution of subhaloes. Each snapshot contains information for the subhaloes – including the position, velocity, maximum circular velocity $\mathrm{V_{max}}$, position of this velocity r_{vmax} and tidal mass M_{tid} for every substructure residing within the simulation box.

The parent haloes from these seven cosmological simulations do not possess exactly similar profile characteristics such as M_{200}, the mass enclosed within the sphere with radius r_{200}, where r_{200} represents the radius at which the mean density of the DM halo is 200 times the critical density of the universe (ρ_{crit}). Thus, we scale the properties of subhaloes from all seven simulations in terms of their position, velocity and mass using similar scaling relations mentioned by Kannan et al. (2012). All the simulations were scaled with respect to the M_{200} of the "Aq-D2" simulation - $1.77 \pm 10^{12}\ M_{\odot}$. The quantity g represents the scaling factor in

$$M\ [\ \ M_{\mathrm{orig}}/g, \tag{2.1}$$

$$v_{x,y,z}\ [\ \ \frac{v_{\mathrm{orig},x,y,z}}{g^{1/3}} \qquad \text{and} \tag{2.2}$$

$$x=\frac{x_{\mathrm{orig}}}{g^{1/3}} \qquad y\ [\ \ \frac{y_{\mathrm{orig}}}{g^{1/3}} \qquad z\ [\ \ \frac{z_{\mathrm{orig}}}{g^{1/3}}. \tag{2.3}$$

The subscript "orig" corresponds to the original non-scaled quantities. Such scaling is important for a statistically meaningful comparison of different simulations. After having done the rescaling, all the host haloes have the same mass and size but different concentrations, hence different r_{vmax} and V_{max}.

According to early N-body simulations of dark matter haloes following the ΣCDM structure formation model, the density profile of the DM haloes could be well described via the known Navarro-Frank-White (NFW) profile (Navarro et al., 1997)

$$\rho_{\rm NFW})r+[\quad \frac{\rho_{\rm s}}{)r/r_{\rm s}+)2\ 0\ \ r/r_{\rm s}+^2}. \tag{2.4}$$

where $\rho_{\rm s}$ and $r_{\rm s}$ are the scale density and scale radius of the subhalo. The $\rho_{\rm s}$ can be computed given the concentration c of the halo which is simply the ratio of $r_{200}/r_{\rm s}$ and the overdensity $\delta_{\rm c}$ with respect to $\rho_{\rm crit}$ using

$$\delta_{\rm c}\ [\quad \frac{\rho_s}{\rho_{\rm crit}}\ [\quad \frac{311}{4}\frac{{\rm c}^3}{ln)2\ 0\ \ {\rm c}+\quad {\rm c}/)2\ 0\ \ {\rm c}+} \tag{2.5}$$

Table 2.1.2 shows the *normalised* properties of the host haloes from VLII and six Aquarius simulations. The particle resolution of the simulation suites $\rm m_{p,orig}$ which is $\approx 10^4\ M_\odot$ motivated us to perform a mass cut and consider subhaloes with $M_{\rm tid} \sim 10^6\ M_\odot$ since substructures with lower mass consist of only a few hundred particles. This introduces some uncertainties in determining the characteristics of these subhaloes at the outer regions. The analysis performed on the subhaloes in this work includes this lower mass cut. In addition to M_{200} and r_{200}, the maximum circular velocity $\rm V_{max}$ and concentration c are listed. For each parent halo we also know r_{50}, the radius at which the mean density is 50 times $\rho_{\rm crit}$; $\rm V_{50}$, the circular velocity at this radius and $f_{\rm sub}\ [\quad f_{\rm sub}^{cum})r_{50}+,$ the percentage fraction of the cumulative mass residing in substructures relative to the host halo enclosed mass at r_{50} and seen as a measure of the host halo clumpiness. It appears that VLII has less mass residing in bound substructures – $f_{\rm sub} \sim 5$ percent – compared to the Aquarius simulations.

Fig. 2.1.1 illustrates $f_{\rm sub}^{cum})r+,$ which is the substructure mass relative to the halo's enclosed mass at r, as function of distance from the parent halo's centre for all seven simulations. Within the inner 20 kpc, Aq-B2 has the highest subhalo mass fraction, while Aq-C2 possesses the lowest value across nearly all radii. Fig. 2.1.2 illustrates an inverse cumulative histogram for the number of subhaloes as function of their normalised $M_{\rm tid}$. All the simulations have a similar slope while the scatter in the high-mass regime is the result of low number statistics. For VLII the slope decreases at a subhalo mass $\lesssim 2 \pm 10^6\ M_\odot$; below this mass-range, the

difference is sensitive to the subhalo finding algorithm and also the mass resolution. Accordingly, the substructure distribution is influenced by lower mass subhaloes that could dominate over higher mass ones by few orders of magnitude in abundance.

Table 2.1.2: Normalised main halo properties; m_p is the original particle mass and g is the scaling factor. M_{200} is the normalised mass enclosed within a sphere of radius r_{200}, where the mean density of the halo is 200 times the critical density of the universe. c is the concentration while V_{max} is the maximum circular velocity of the halo. r_{50} is the radius of the main halo at which the halo encloses the mass with mean density 50 times the *background* density and V_{50} is the circular velocity at this radii. f_{sub} represents the cumulative mass fraction which resides in substructures relative to the total enclosed mass within r_{50}.

Simulation	$m_{p,orig}$ $[M_\odot]$	g	M_{200} $[10^{12}\ M_\odot]$	r_{200} [kpc]	c	V_{max} $[km\,s^{-1}]$	r_{50} [kpc]	V_{50} $[km\,s^{-1}]$	f_{sub} [%]
VLII	4.10 ± 10^3	1.188	1.774	242.8	13.29	212.9	425.7	151.8	4.77
Aq-A2	1.37 ± 10^4	0.963	1.774	242.8	16.19	205.9	428.2	156.3	12.46
Aq-B2	6.45 ± 10^3	2.166	1.774	242.8	9.72	204.0	418.0	152.6	9.61
Aq-C2	1.40 ± 10^4	1.000	1.774	242.8	15.21	222.4	417.1	152.3	6.67
Aq-D2	1.40 ± 10^3	-	1.774	242.8	9.37	203.2	425.7	158.1	13.14
Aq-E2	9.59 ± 10^3	1.497	1.774	242.8	8.26	204.8	421.3	153.8	9.85
Aq-F2	6.78 ± 10^3	1.564	1.774	242.8	9.79	196.3	424.7	155.0	12.80

2.2 Identifying the most effective subhalo candidates

As mentioned above, we are interested in subhaloes which are likely to interact with the galactic disc; hence we need to identify such subhaloes. We apply a simple selection criterion by estimating the pericentre distances of all subhaloes. We select these by determining the orbit of subhaloes in the presence of the background potential of the host DM halo only. Using the initial 6-dimensional phase-space information of the subhaloes we integrate their orbits using the standard Runge-Kutta 4th order orbit integrator, which determines the position and velocity of subhaloes at each integration step (Press et al., 1992), for 2 Gyr. Any subhalo that comes closer than 25 kpc to the parent halo's centre at any point during its orbit is marked as a *crossed* candidate. This calculation does not take into account dynamical friction and the gravitational force of the disc and the bulge.

Fig. 2.2.1 shows $M_{\rm tid}$ vs. $r_{\rm peri}$ for subhaloes at the high mass end, with $M_{\rm tid} > 21^9 M_\odot$, for all simulations (colour coded). The vertical dashed line marks the 25 kpc radius, and all the objects to the left of this line are our crossed objects. Instead of using a simple distance cut (and a mass cut at $M_{\rm tid} > 21^8 M_\odot$), the strength of the tidal forces on the disc and resonances of the orbital motion and the disc could have been used. The four dotted lines correspond to lines of constant tidal force at 10 kpc from the galactic centre. These correspond to objects with $M_{\rm tid}$ of 1, 3, 10 and 100 $\pm$ $10^8 M_\odot$ (from right to left) at $r_{\rm peri}$=25 kpc. All subhaloes to the left of these lines have higher tidal forces. There is one object in Aq-E2 with a mass of $\approx 10^{10} M_\odot$ and a pericentre at 28 kpc, to the left of the red line ($10^9 M_\odot$) which has a tidal force greater than a subhalo with $M_{\rm tid}$=$10^9 M_\odot$ at $r_{\rm peri}$=25 kpc and should have been included. However, there are 2 subhaloes in Aq-E2 with larger tidal force (left of green line). It turned out, that only satellites left of the green line contribute to the disc heating on a measurable level. We conclude that we did not miss a significant fraction of interactions, which would change the derived dynamical heating of the disc.

Previous analytical studies proposed a linear scaling between the heating of the galactic disc due to satellites and the subhalo mass $M_{\rm sat}$. However Hopkins et al.

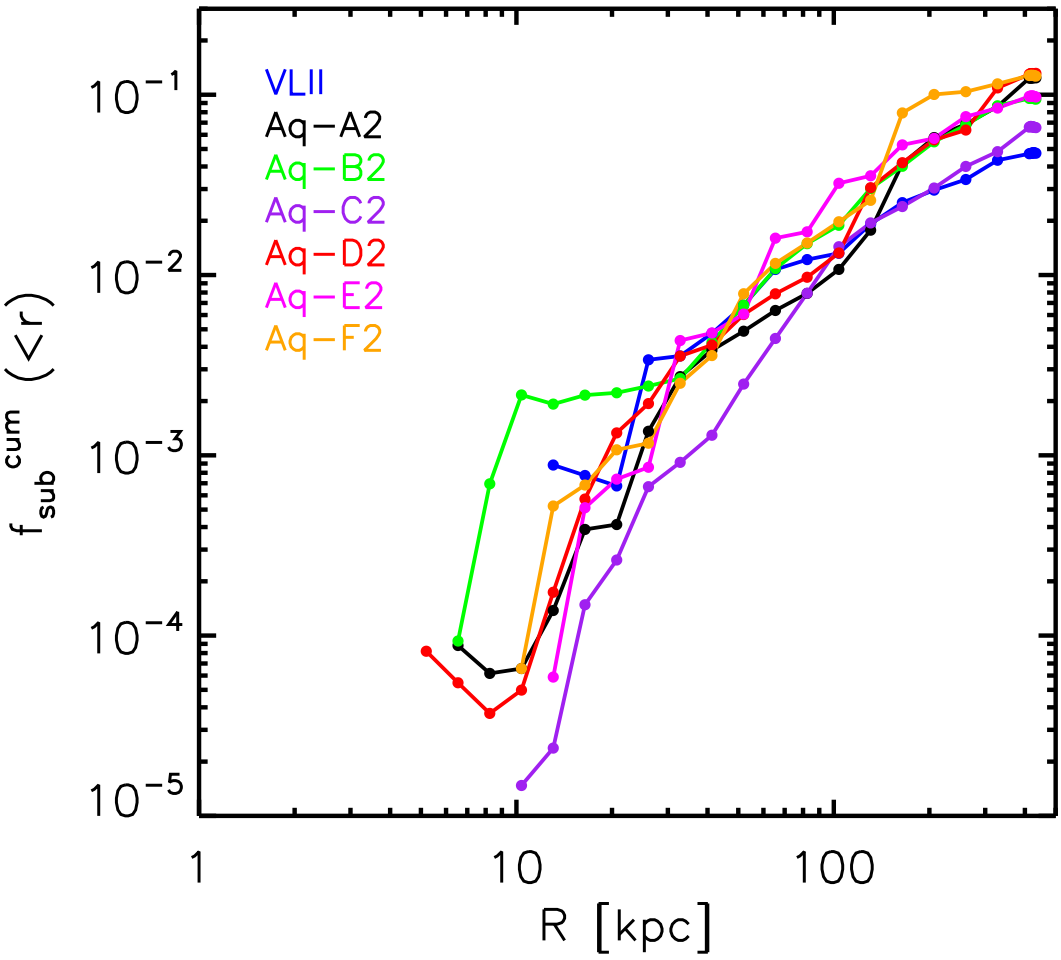

Figure 2.1.1: Cumulative subhalo mass fraction, substructure mass relative to the halo's enclosed mass at r, as function of distance from the host halo centre.

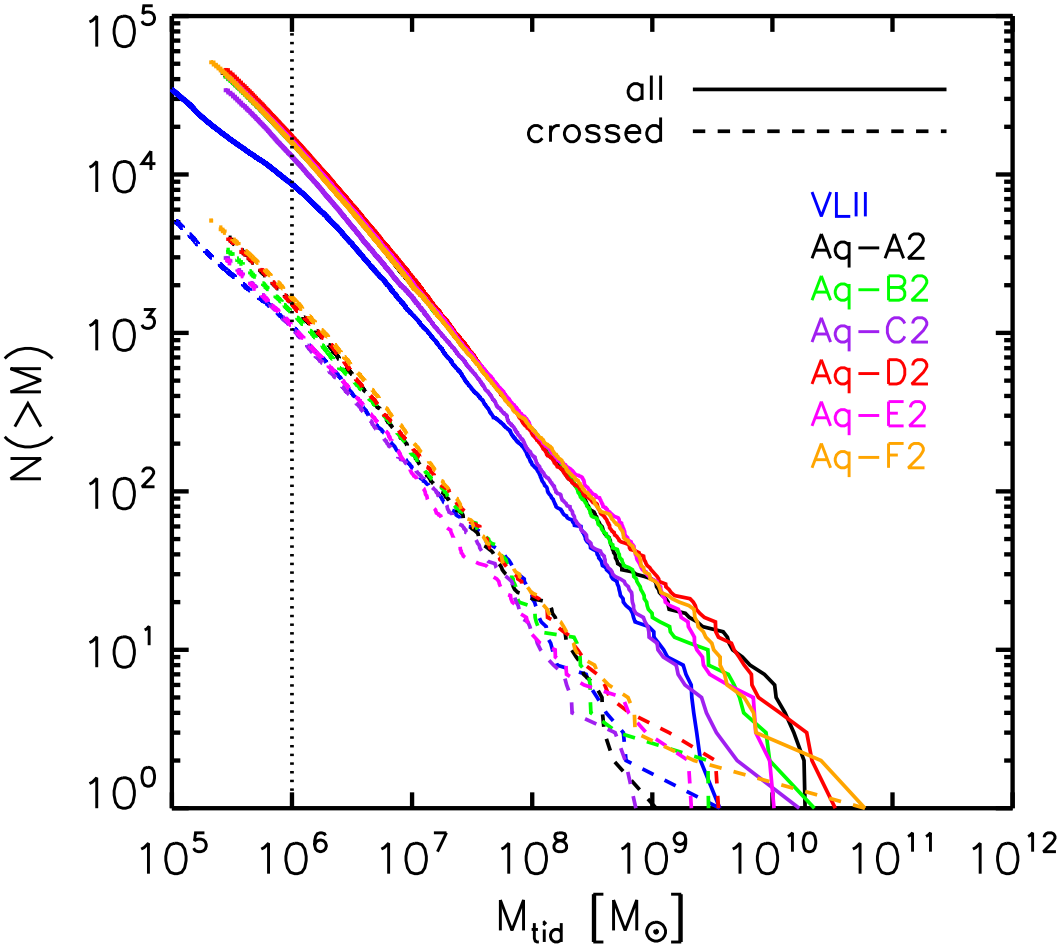

Figure 2.1.2: Inverse cumulative histogram for the number of subhaloes as function of subhalo mass within r_{50} of the host haloes. The crossed population corresponds to the subhaloes which come closer than 25 kpc to the centre of the host halo within 2 Gyr while all represents the total sample. The vertical line marks the mass cut at 10^6 $M_\odot$.

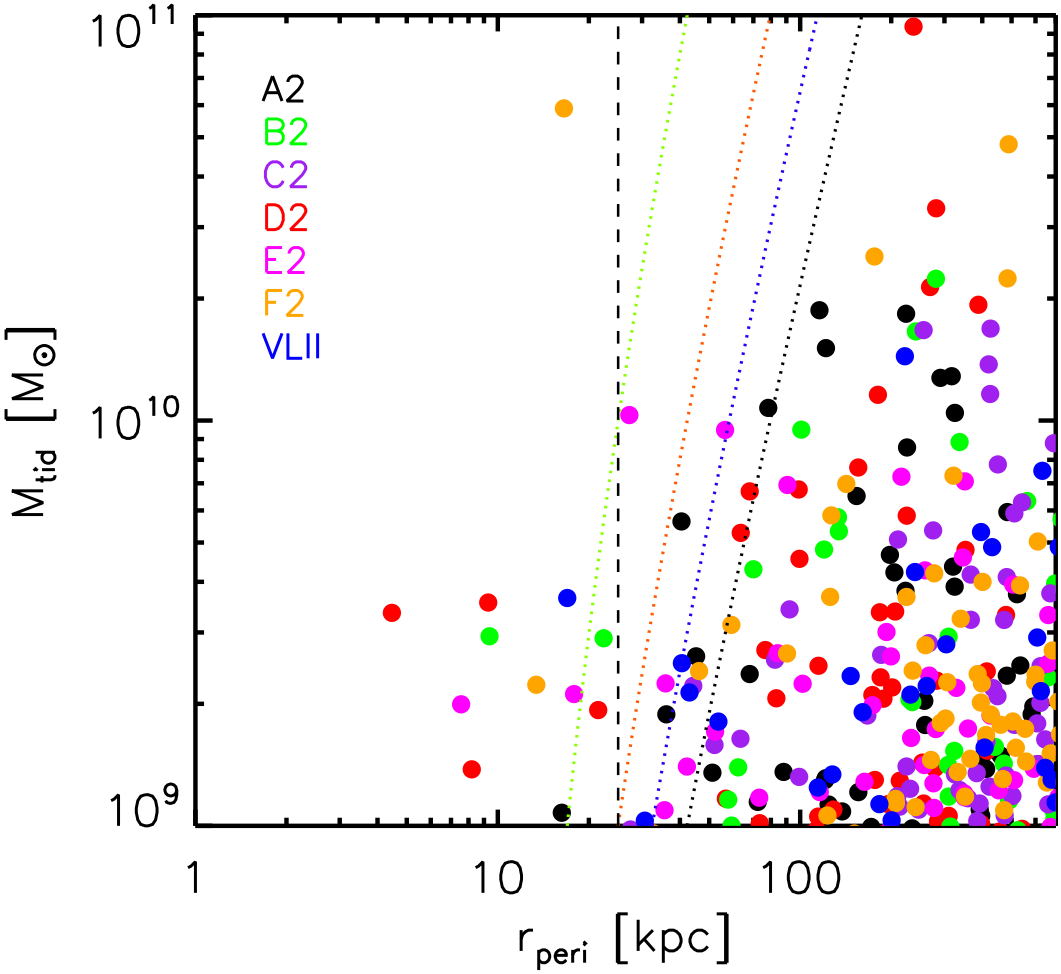

Figure 2.2.1: $M_{\rm tid}$ against pericentre distance $r_{\rm peri}$ for all 7 simulations (colour coded). The vertical dashed line marks the 25 kpc crossing criteria radii; all the subhaloes to the left of this line are regarded as crossed candidates. The 4 dotted lines correspond to lines of same tidal force at 10 kpc from the galactic centre as objects with $M_{\rm tid}$ of 1, 3, 10 and 100 $\pm$ $10^8 M_\odot$ (from right to left) at $r_{\rm peri}$=25 kpc. All subhaloes to the left of these lines have higher tidal forces.

(2008) investigated the importance of such dependence using "live" components for the disc and the subhaloes, together with realistic non-circular orbits of satellites. They concluded that the heating rate per Gyr due to continuous infall, which forms the basis of our study, scales non-linearly as $\propto M_{\rm sat}^2$ taking into account dynamical friction. This result contradicts earlier work which had only focused on the single interaction of subhaloes with discs and scaled linearly as $\propto M_{\rm sat}$ per merging event. In other words, most of the impact is expected from the most massive subhaloes found in the scatter in the high-mass end of the subhalo mass spectrum (Fig. 2.1.2).

In this study, we focus on the interaction of subhaloes with $M_{\rm tid} \geqslant 10^8\ M_\odot$ corresponding to $M_{\rm tid}/M_{\rm disc} \gtrsim 0.003$. Table 2.2.1 includes information regarding the subhalo distribution in all seven simulations together with statistics of the "crossed" sub-sample. $\rm N_{sub}$ is the total number of subhaloes in each simulation suite with $M_{\rm tid} \sim 10^6\ M_\odot$, while $p_{\rm sub}$ shows the fraction of subhaloes within r_{50}. The percentage fraction which cross the introduced 25 kpc sphere is represented by $p_{\rm cross}$. VLII and Aq-F2 have the largest $p_{\rm sub}$ values together with the highest crossed fractions. However, Aq-E2 possesses the least number of subhaloes that cross the disc, although it has the fourth highest substructure fraction inside r_{50}. The last four columns of table 2.2.1 show the number of crossed subhaloes with masses $\geqslant$ 1, 3, 5 and 10 $\pm\ 10^8\ M_\odot$. We found a range of subhaloes from 12 to 24 with $M_{\rm tid} \geqslant 1 \pm 10^8\ M_\odot$ which provides a good sample for analysing the impact of both the number and mass range of satellites. Aq-D2 has the largest number of subhaloes with mass $\geqslant 1 \pm 10^9\ M_\odot$ and Aq-F2 is the only simulation that has one candidate $\geqslant 1 \pm 10^{10}\ M_\odot$.

Table 2.2.1: Number statistics of subhaloes; $p_{\rm sub}$ is the percentage of the subhaloes originally within r_{50} while $p_{\rm cross}$ shows the percentage of subhaloes inside r_{50} which cross the disc in 2 Gyr. $\star$: One of the subhaloes has M $> 10^{10}\ M_{\odot}$

Simulation	$\rm N_{sub}$	$p_{\rm sub}$ [%]	$p_{\rm cross}$ [%]	$\rm N_{cross}$ ($> 10^8\ M_{\odot}$)	$\rm N_{cross}$ ($> 3 \pm 10^8\ M_{\odot}$)	$\rm N_{cross}$ ($> 5 \pm 10^8\ M_{\odot}$)	$\rm N_{cross}$ ($> 10^9\ M_{\odot}$)
VLII	28,618	30.36	12.71	21	5	3	1
Aq-A2	108,396	14.72	9.70	20	6	1	1
Aq-B2	133,793	11.85	8.45	17	6	3	2
Aq-C2	121,334	10.68	8.39	14	3	2	0
Aq-D2	72,380	24.01	8.85	23	8	5	4
Aq-E2	93,322	17.49	6.77	12	5	5	2
Aq-F2	51,985	30.54	10.49	24	9	5	$2^{\star}$

The time evolution of the satellites' orbits from our N-body simulations (see section 3) are shown in Fig. 2.2.2 for all 7 simulations. The colours correspond to the mass range of the satellites; $10^8 \geq M_{\rm tid} < 5 \pm 10^8$ (grey) and $M_{\rm tid} \sim 6 \pm 21^8 M_\odot$ following a colour map. The dashed lines represent the 25 kpc crossing radius. The real pericentric distances from our simulations are very close to the estimated pericentres found in the analysis that used an orbit integrator and the background potential of the host halo (section 2.2). The presence of additional mass from bulge+disc slightly reduces $r_{\rm peri}$, hence the effective limit of selected satellites is less than 25 kpc. The crossing of satellites is rather continuous with time.

2.3 Subhalo statistics

Prior to the numerical analysis of the interaction of satellites and the galactic thin disc, it is useful to discuss the properties of all subhaloes in our seven cosmological simulation suites. Fig. 2.3.1 represents the inverse cumulative histogram of three quantities: N(>M) (dashed), $M_{\rm tid}$ (solid) and $M^2_{\rm tid}$ (dash dotted) for all the *crossed* subhaloes initially within r_{50}. Aquarius simulations have a similar range for $\rm N_{sub}$. Aq-F2 shows a significant jump at the high mass end of $M_{\rm tid}$ due to the presence of one subhalo with $M_{\rm tid}$ [$6.=\pm 21^{10} M_\odot$, which actually resides in the minor merger range. For Aq-F2 80% of the mass resides above $10^9 M_\odot$, while for the rest of the simulations the same percentage is reached at $10^7 M_\odot$. As mentioned above the expected impact strength scales with $M^2_{\rm tid}$; more than 95% of the impact is expected from the really massive subhalo for Aq-F2. Aq-D2 has the second highest expected impact due to massive subhaloes and Aq-C2 has the lowest. In all cases more than 90% of the impact is expected from subhaloes above $10^8 M_\odot$.

The cumulative histogram of $\rm V_{max}$ for all (solid) and crossed (dashed) subhaloes is shown in Fig. 2.3.2. The $\rm V_{max}$ values are normalised using the circular velocity ($\rm V_{50}$) of the host halo at r_{50}. About 90% of the subhaloes have $\rm V_{max}$ less than $1.16 V_{50}$ since the simulations are dominated by lower mass subhaloes. Moving towards subhaloes with $\rm V_{max}$ greater than $1.2 V_{50}$, the scatter between the simulations increases due to low number statistics. For all the subhaloes, VLII lies on average below Aquarius over the whole spectrum. For the crossed subhaloes it appears the deviation between VLII and Aquarius becomes less significant. The two dashed lines

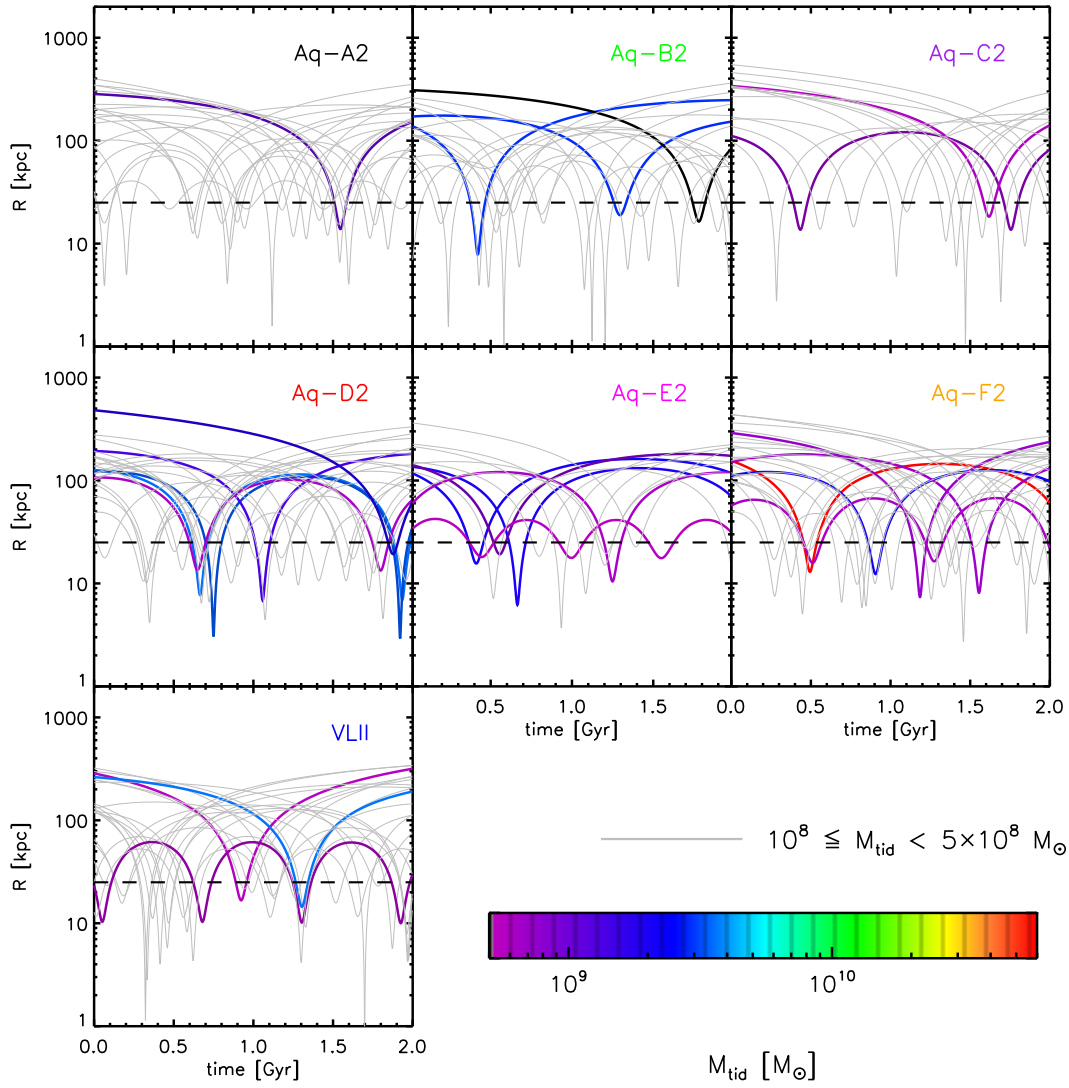

Figure 2.2.2: The time evolution of the orbits of subhaloes from our N-body simulations in spherical coordinates for all seven host haloes. Subhaloes with $10^8 \geq M_{\rm tid} < 5 \pm 10^8 M_\odot$ are shown using grey colour while objects with $M_{\rm tid} \sim 6 \pm 21^8 M_\odot$ are represented following a colour map.

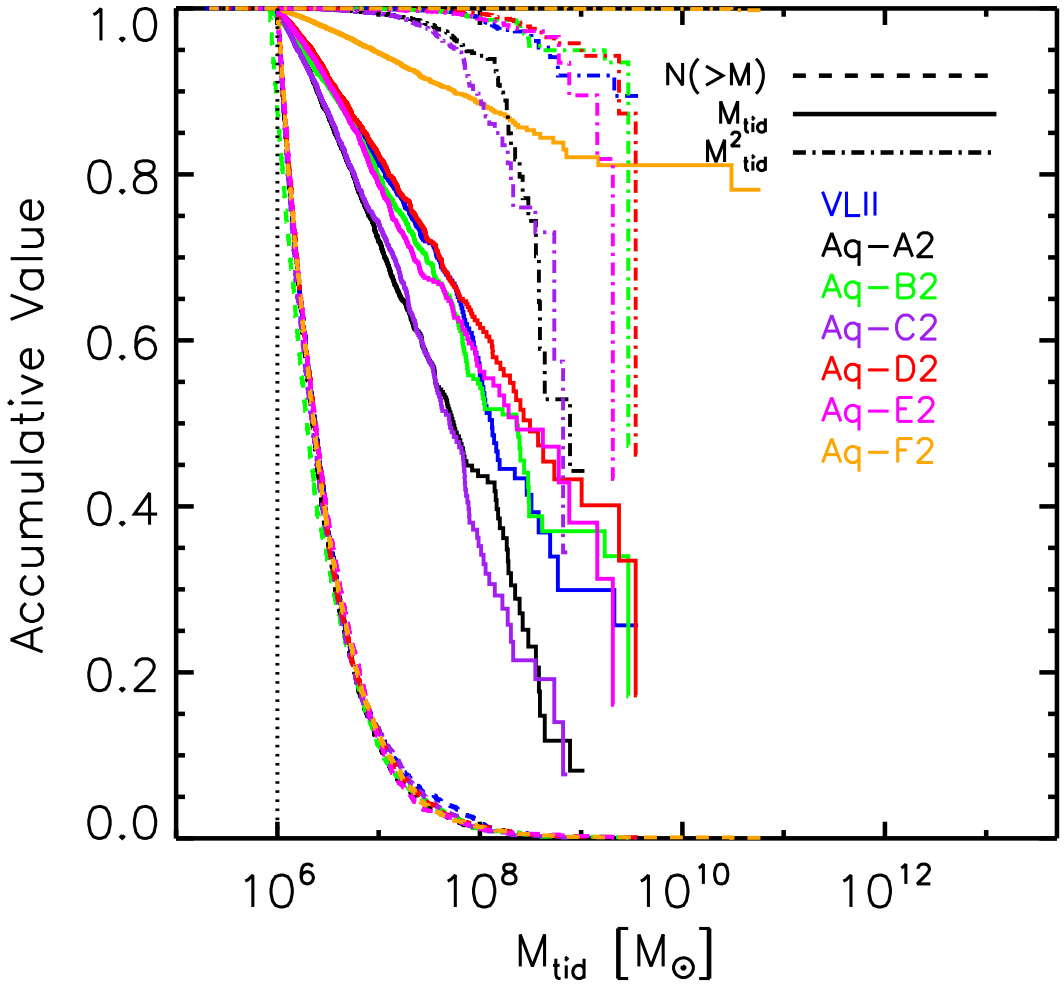

Figure 2.3.1: Inverse cumulative histogram of number N (dashed), $M_{\rm tid}$ (solid) and $M^2_{\rm tid}$ (dotted) of crossed subhaloes for all our seven simulations as function of subhalo mass $M_{\rm tid}$. The vertical line marks the mass cut at 10^6 $M_\odot$.

correspond to the average of the best-fitting power laws over all the seven simulations, except in the case of all the subhaloes were we have excluded VLII. The fitted power laws have the form

$$N)> \mathrm{V}_{\mathrm{max}}+[\ \ \beta\,)\mathrm{V}_{\mathrm{max}}/\mathrm{V}_{50}+^{\alpha} \tag{2.6}$$

$$\begin{array}{llll} \beta & [& 1.287 \pm 21^{5} & \alpha\ [\ \ 3.=7\ \ \text{all} \\ \beta & [& 1.146 \pm 21^{4} & \alpha\ [\ \ 3.98\ \ \text{crossed.} \end{array}$$

The slope of the power laws are similar, indicating that the crossed subhaloes are representative of the total population. Also, the slope agrees well with that mentioned in Springel et al. (2008).

Fig. 2.3.3 presents two quantities $p_{\mathrm{cross},1}$ (top) and $p_{\mathrm{cross},2}$ (bottom) which are defined as $\mathrm{N}_{\mathrm{cross}})r+/\mathrm{N}_{\mathrm{all}})r+$and $\mathrm{N}_{\mathrm{cross}})r+/\mathrm{N}_{\mathrm{cross}}$, respectively. The crossed subhaloes located at $r > 100$ kpc contribute to less than 20% of total population at such distance. However these subhaloes make up $\approx 50\%$ of the total crossed fraction $p_{\mathrm{cross},2}$.

For the purpose of numerical analysis, each crossed subhalo candidate will be generated as a distribution of particles following a NFW profile. To reproduce these subhaloes with a corresponding NFW density profile we determine the radius, r_{tid}, enclosing the provided mass M_{tid}, using the scale radius r_{s} and $\mathrm{V}_{\mathrm{max}}$ of subhaloes. Using

$$r_{\mathrm{vmax}}\ [\ \ 3.274\ r_{\mathrm{s}}, \tag{2.7}$$

$$\left(\frac{\mathrm{V}_{\mathrm{max}}}{r_{\mathrm{vmax}}}\right)^{2}\ [\ \ 5\,\pi\,\mathrm{G}\,\rho_{\mathrm{sat}})r_{\mathrm{vmax}}+ \tag{2.8}$$

and

$$M_{\mathrm{tid}}\ [\ \ 5\,\pi\,\rho_{\mathrm{s}}\,r_{\mathrm{s}}^{3}\left[ln)2\,0\ \ \mathrm{c}_{\mathrm{tid}}+\ \ \frac{\mathrm{c}_{\mathrm{tid}}}{2\,0\ \ \mathrm{c}_{\mathrm{tid}}}\right] \tag{2.9}$$

together with equation (2.4) outline the most important steps in determining the tidal radius r_{tid} of subhaloes via calculating $\mathrm{c}_{\mathrm{tid}}$ which is the ratio of $r_{\mathrm{tid}}/r_{\mathrm{s}}$. The median of the concentration $\mathrm{c}_{\mathrm{tid}}$ as a function of distance from the centre of the host halo is shown in Fig. 2.3.4 for all (top) and crossed (bottom) subhaloes. The

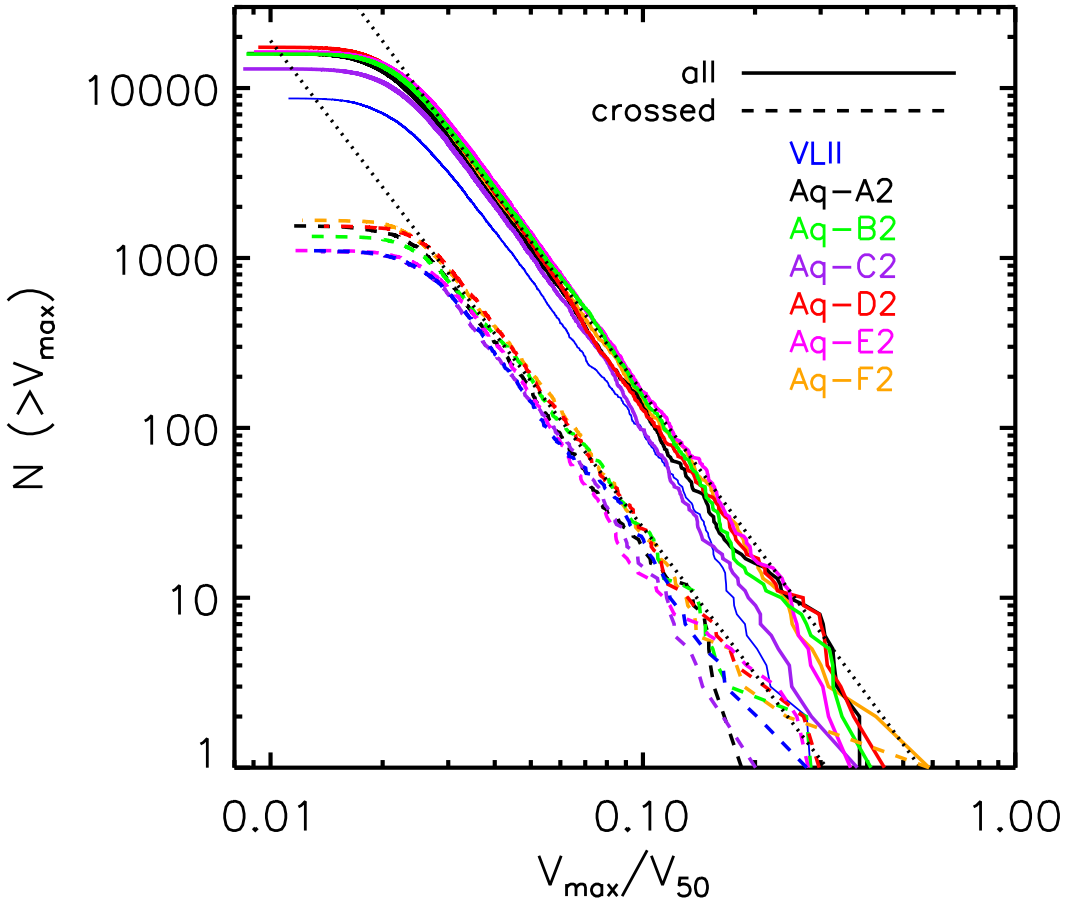

Figure 2.3.2: Cumulative V_{max}/V_{50} histogram for all (solid) and crossed (dashed) subhaloes; here V_{max} is the maximum circular velocity of the subhalo while, V_{50} is the circular velocity of the main halo at r_{50}.

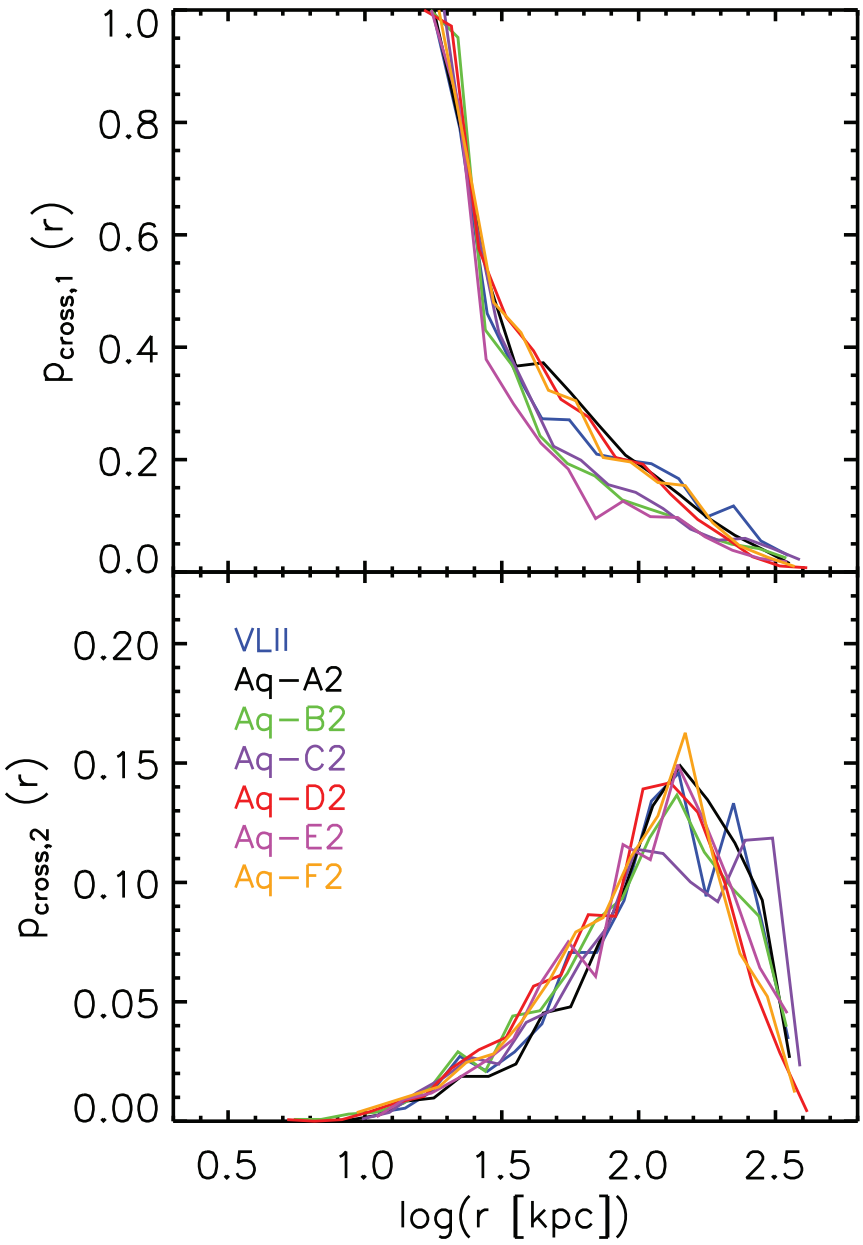

Figure 2.3.3: *Top*: Fraction of crossed to all subhaloes $p_{\mathrm{cross},1}$ for spherical shells from centre of their host halo, defined as $\mathrm{N_{cross}})r+/\mathrm{N_{all}})r+$ *Bottom*: Normalised radial distribution of all crossed subhaloes, $p_{\mathrm{cross},2}$, representing $\mathrm{N_{cross}})r+/\mathrm{N_{cross}}$.

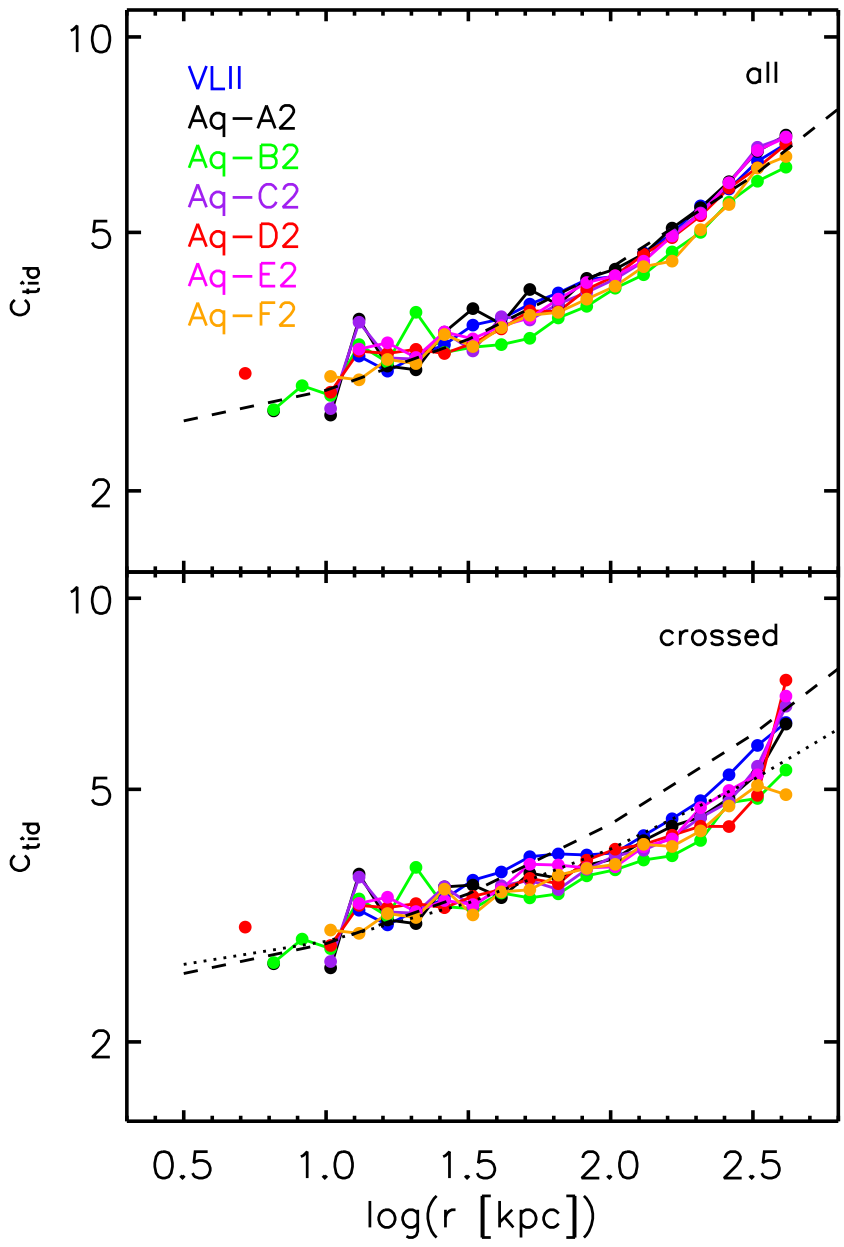

Figure 2.3.4: Mean concentration c_{tid} against the distance from centre of the host halo, r, for all (top) and crossed (bottom) subhaloes. The dashed and dotted lines represent the average best-fitting power laws for the total and crossed candidates, respectively.

outer most bin at $r \approx r_{50}$ extends to infinity. For guiding the eye, best power law fits for all subhaloes (dashed) and for the crossed ones (dotted) are shown. In both populations we observe higher c_{tid} with increasing distance from the host. Hence the subhaloes located further away from the centre tend towards higher concentrations. This trend is due to the tidal mass loss of the subhaloes and is well known (Nagai and Kravtsov, 2005). The scatter between different simulations is insignificant. It is notable that the concentration of subhaloes located at r greater than 30 kpc are, on average, lower for the crossed sample as seen by the deviation of the slope between the fitted power laws. At r=150 kpc where the maximum $p_{cross,2}$ is observed (Fig. 2.3.3), the total population has higher c_{tid} by a factor of 1.12. For $r < 30$ kpc the two populations show very comparable concentrations. This suggests that subhaloes on radial orbits lose more mass, when entering the main halo at r_{50} already.

Fig. 2.3.5 is the normalised histogram of c_{tid} for all (solid) and crossed (dashed) subhaloes. The peak of the distribution for the total population is around $c_{tid} \approx 4.5$ while for the crossed subhaloes we observe a shift of the distribution to lower concentrations with the peak around 3.6. This indicates that lower concentration is favoured by crossed satellites. The reason for this behaviour consists of two points. The mean concentration of crossed subhaloes is smaller for r greater than 100 kpc (Fig. 2.3.4) and the fraction of crossed subhaloes, $p_{cross,1}$, is decreasing with increasing r leading to a biased selection towards lower c_{tid}.

The median of the concentration as function of subhalo mass for all (top) and crossed (bottom) subhaloes is plotted in Fig. 2.3.6. Here and also for Fig. 2.3.9 the final bin includes all the subhaloes with larger mass. The scatter for the crossed subhaloes is smaller than for the total population. The dashed and dotted lines represent best fits for all and crossed samples following a power law

$$c_{tid} \; [\;\; c_8 \left(\frac{M_{tid}}{21^8 M_\odot} \right)^{\eta}, \tag{2.10}$$

where c_8 corresponds to the c_{tid} value at tidal mass of $10^8 M_\odot$. The slope of the power law is identical in both plots (η [1.16). We observe a shift to lower concentrations for crossed subhaloes by a factor of 1.35 which corresponds to the shifted maximum in Fig. 2.3.5. The agreement between VLII and Aquarius is

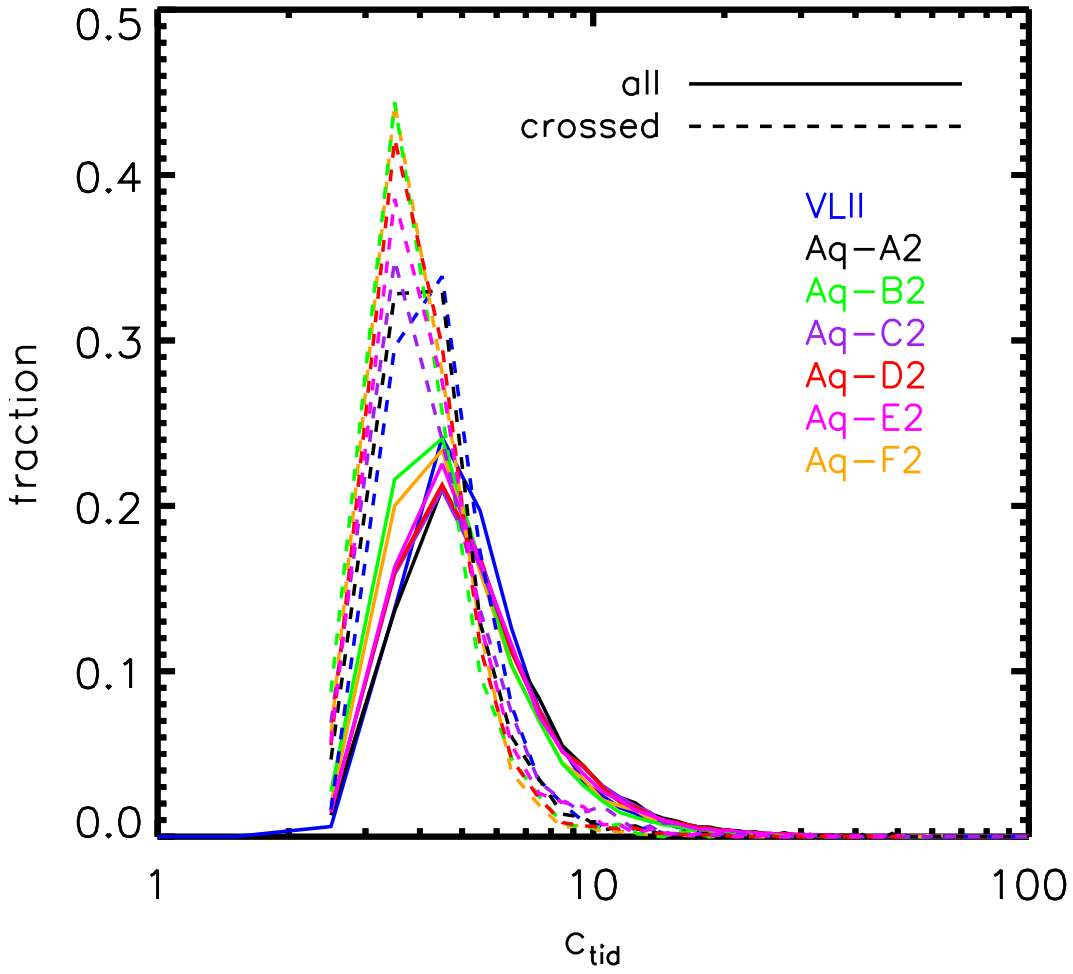

Figure 2.3.5: Normalised distribution of c_{tid} for all (solid) and crossed (dashed) subhaloes.

particularly noticeable for the crossed populations.

Fig. 2.3.7 represents the distribution of pericentres (solid) and initial distances (dashed) of subhaloes for all seven simulations. The vertical lines mark the position of the 25 kpc crossing criterion. VLII has the lowest number of subhaloes both with pericentres less than 25 kpc and also over the whole distance range. This is partially due to the fact that VLII is dominated by low-mass subhaloes, with $M_{\rm tid} \geq 10^6\ M_\odot$, which are ignored in this analysis. There exists some variation in the maximum of the pericentre distribution between the simulations, but most subhalo pericentres lie in the range $10 < r < 100$ kpc.

Another interesting aspect is the angular distribution of subhaloes in the simulations. The cosine of the inclination angle i (solid) and the azimuthal angle ϕ (dashed) of initial positions are represented in Fig. 2.3.8 which are measures of *isotropy*. These quantities are calculated by

$$\text{ert})i+[\quad \frac{z}{r} \qquad \text{and} \tag{2.11}$$

$$\phi\,[\quad \text{wco}^{-1}\left(\frac{y}{x}\right) \qquad 291 < \phi < 291, \tag{2.12}$$

where x,y and z represent the position of the subhaloes in Cartesian coordinates and r is the distance to the host halo's centre in spherical coordinates.

It is important to note in this analysis, the x,y and z directions do not necessarily imply any favoured orientation of the system but rather the chosen disc orientation (section 3.1). In the case of $\cos(i)$, the inclination angle i is measured with respect to the z-component. Therefore $\cos(i)$ of 1 corresponds to the object which is located on the positive z-axis and *vice versa* for $\cos(i)$ of -1. For the Aquarius simulations, this quantity has a rather homogeneous distribution with Aq-E2 showing a slight peak around 0, indicating that more subhaloes are concentrated towards the x-y plane. However, it is interesting that in the case of VLII we clearly see distinct peaks close to 1 and -1, suggesting that most of the subhaloes are close to the z-axis, i.e. on more polar orbits with respect to the disc. The azimuthal angle ϕ tells us how the subhaloes are distributed initially when observed from a top-down view

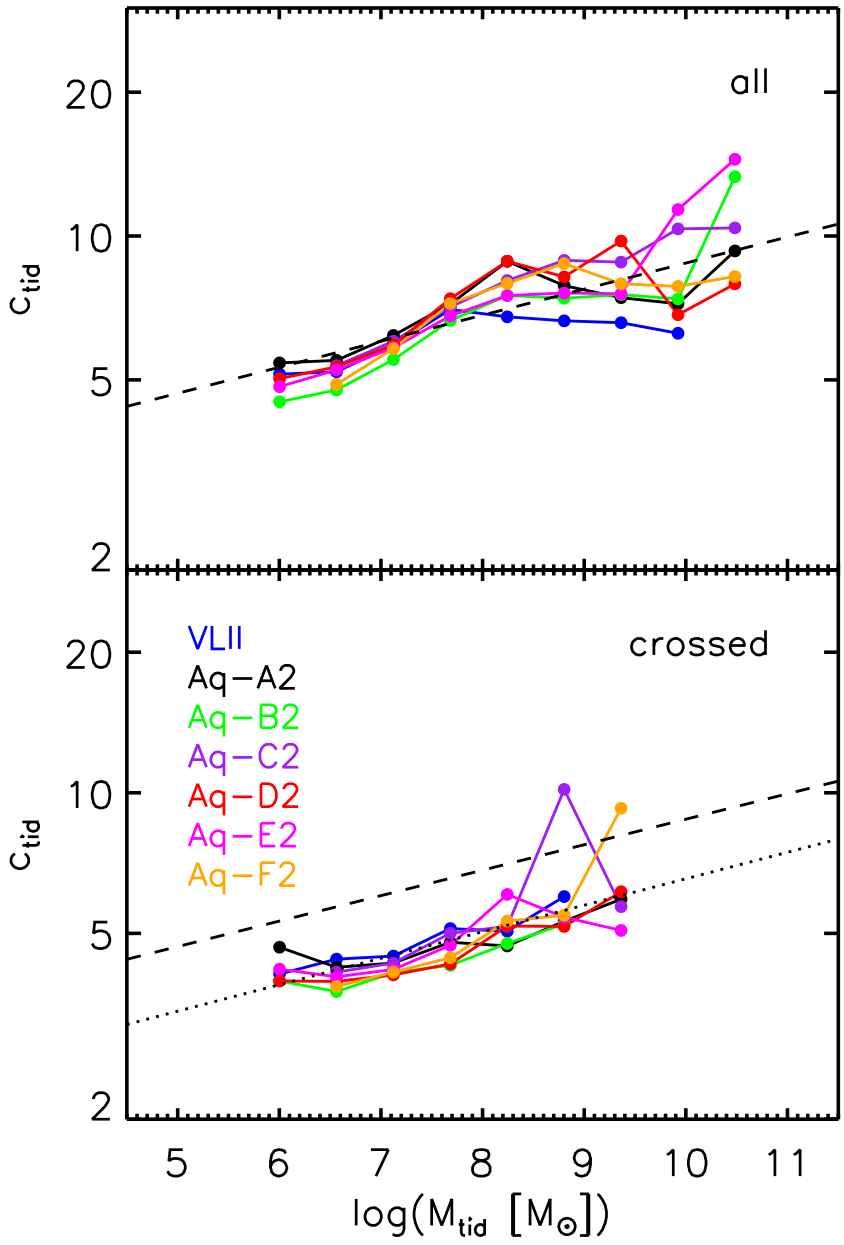

Figure 2.3.6: Concentration $c_{\rm tid}$ against $M_{\rm tid}$ for all (top) and crossed (bottom) subhaloes. The dashed and dotted lines represents the average best-fitting power laws for the total and crossed candidates.

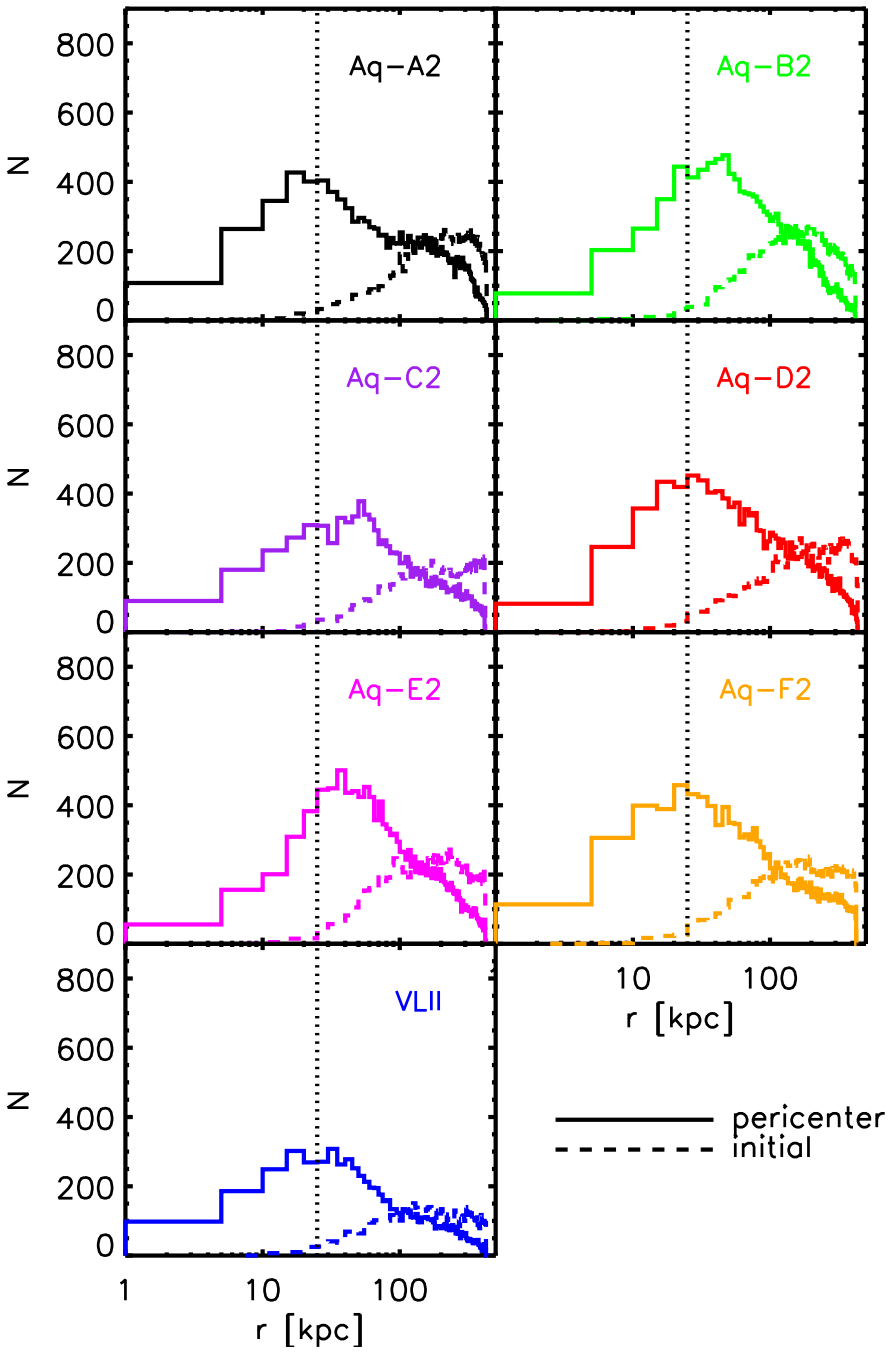

Figure 2.3.7: Pericentre (solid) and initial distance (dashed) histograms for all subhaloes. The vertical dotted lines mark the 25 kpc crossing radii.

(on the x-y plane). We observe the largest deviation from an isotropic distribution for VLII and Aq-A2. The bimodal behaviour indicates that more subhaloes are located around ≡=1° corresponding to the y-axis. Aq-B2 has the most isotropic distribution. We also performed a similar analysis for the crossed subhaloes and concluded that for the Aquarius simulations, the distributions for both quantities become more isotropic – flat in cos)i+and ϕ – while for VLII the bimodality is still found.

One of the important quantities in order to characterize the shape of orbits is the eccentricity e which in calculated using

$$e \left[\sqrt{2 \quad \frac{l^2}{\mu a}} \qquad \text{x l hsh} \qquad \mu \left[\quad G)M_{\text{tid}} \, 0 \quad M_h)r\text{+}\text{+}, \right. \tag{2.13}$$

$$l \left[\quad \vec{r} \pm \vec{v} \, , \right. \tag{2.14}$$

$$a \left[\quad \frac{\mu}{3\epsilon} \quad \text{and} \right. \tag{2.15}$$

$$\epsilon \left[\quad \frac{v^2}{3} \quad \frac{\mu}{r}. \right. \tag{2.16}$$

In the above equation, μ corresponds to the sum of the standard gravitational parameters of the subhalo and the host halo with enclosed mass M_{h} at distance r. The specific angular momentum l is calculated using the velocity and position of the subhalo with respect to the host. The semi-major axis a and the specific orbital energy ϵ are related through equation (2.16). Only in a Kepler potential, the eccentricity and semi-major axis are well-defined and constant along the orbit. A general potential, using the enclosed mass, gives an upper limit for the eccentricities and underestimates the pericentre distances.

Fig. 2.3.9 shows the median eccentricity against M_{tid} for all (top) and crossed (bottom) subhaloes. VLII possesses slightly higher e values than Aquarius over the whole mass range for the total population. Aquarius simulations have a relatively similar behaviour in the $M_{\text{tid}} < 10^9 \, M_\odot$ zone, while the scatter in the higher mass regime is expected. For the crossed subhaloes, the difference between the simulations

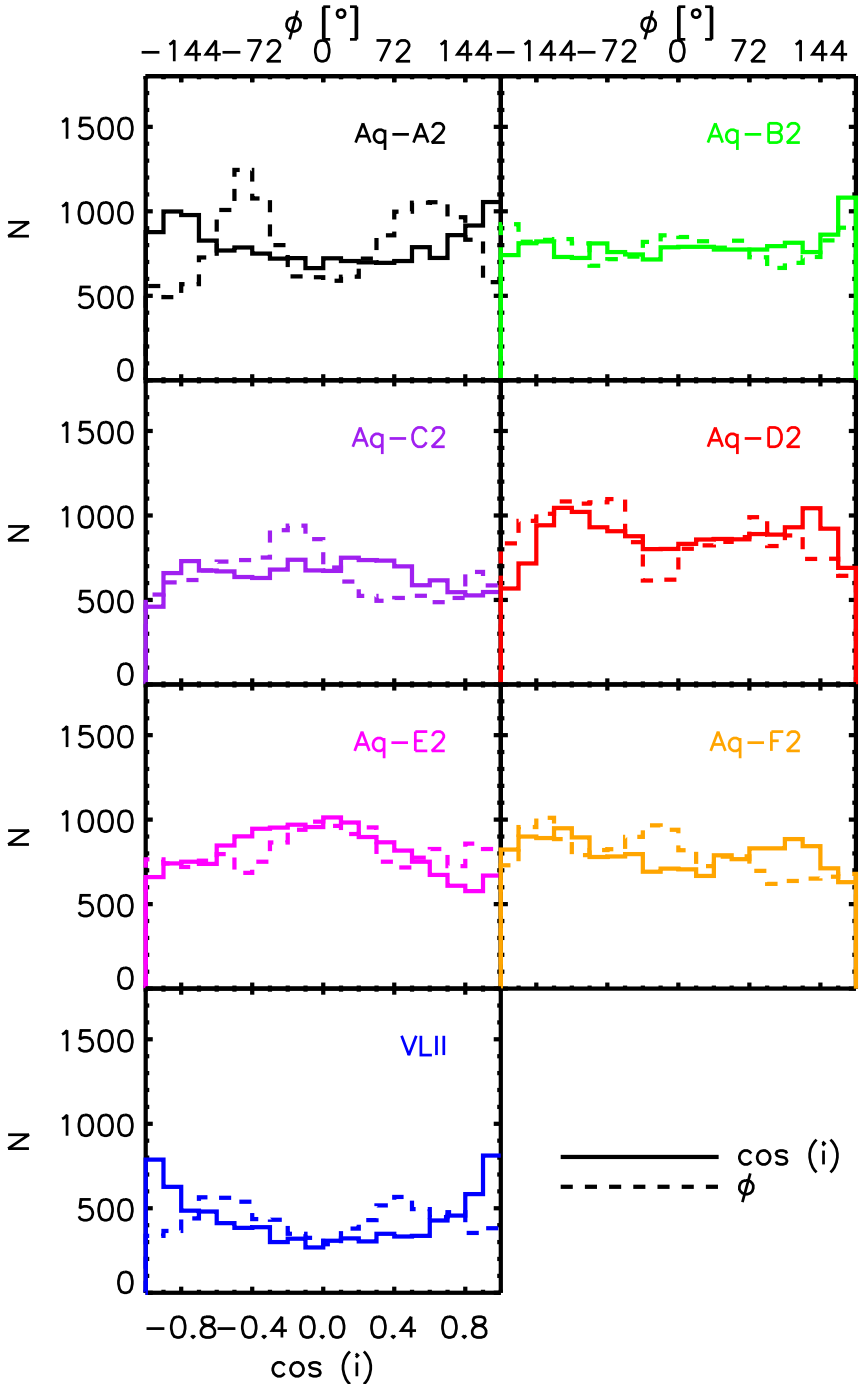

Figure 2.3.8: Distribution in cos(i) (solid) and ϕ (dashed) for all subhaloes; where i is the subhalo inclination angle with respect to the z-component and ϕ is the azimuthal angle.

is minimized and there exists a minor increase of e with $M_{\rm tid}$. In other words the orbits of crossed subhaloes become more parabolic, closer to $e = 1$, for higher masses.

More than 85% of the subhaloes in all seven simulations have $0.5 < e < 1$ – these subhaloes have bound elliptic orbits with respect to the enclosed halo mass at the corresponding radii. Also $\sim$ 10% have hyperbolic trajectories with $e > 1$ and regarded as candidates which would cross once as they pass by the galactic disc. VLII has the highest fraction of subhaloes with unbound orbits.

In order to determine how homogeneous is the infall time distribution of subhaloes, we looked at the pericentric passage time of the subhaloes which correspond to the time of the closest approach to the centre of the host halo. The expected pericentric time of crossed subhaloes for all the seven simulations is shown in Fig 2.3.10. The distribution is fairly homogeneous while we observe a shallow peak around 1 Gyr time; hence the impact of the subhaloes is expected to be continuous with time. There is a lack of encounters for the first 0.5 Gyr which might be due to mass loss of subhaloes already located at close distances. The possible impact of this delay on heating of the galactic disc is discussed in section 3.4. Also the drop seen in all the simulations after 1.5 Gyr could be the result of simulation box's finite volume size. This plot can robustly tell us about the interaction rate per Gyr of subhaloes with the host.

The VLII and Aquarius simulations do not show significant differences in their spatial distribution. The higher mean eccentricities of the VLII satellites is the main difference compared to the Aquarius simulations. However for the crossed subhaloes such a difference disappears.

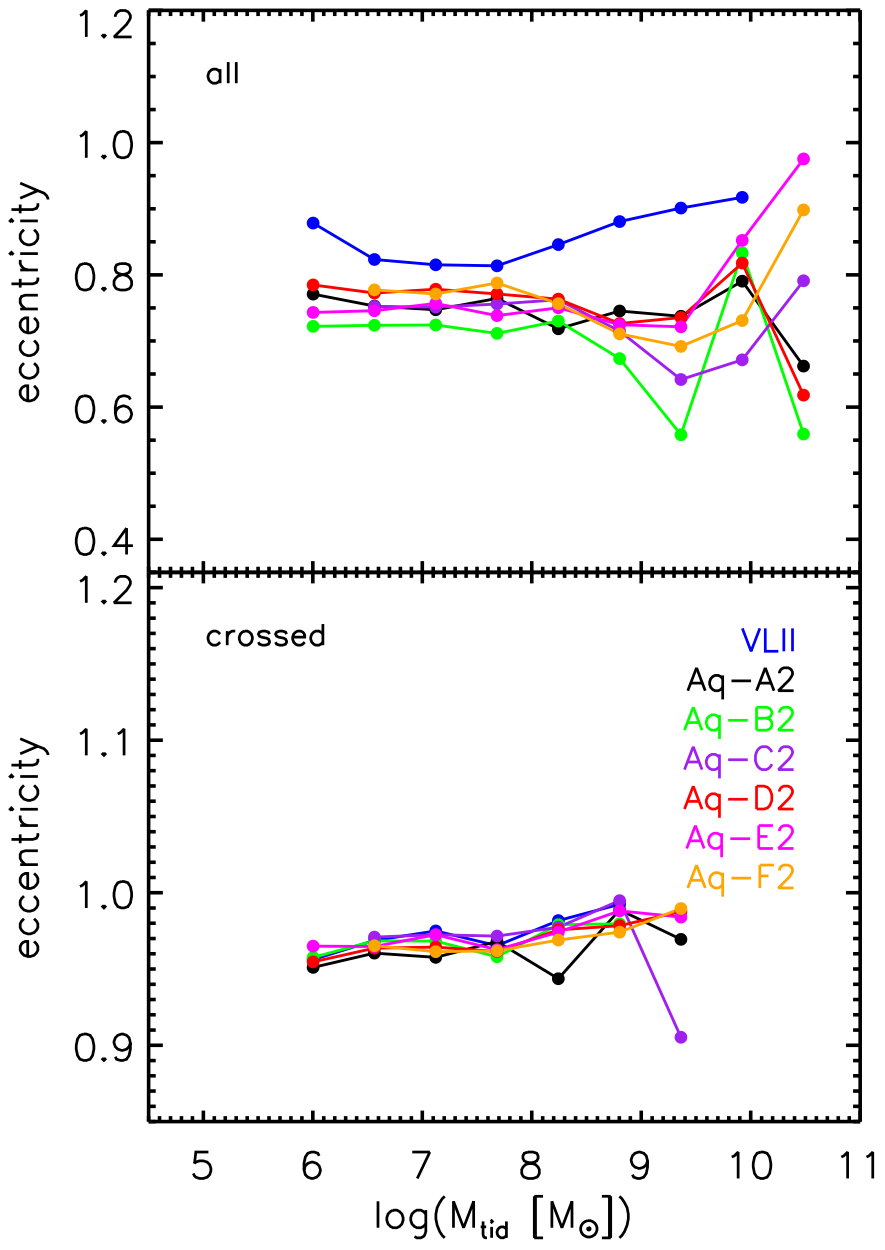

Figure 2.3.9: Eccentricity e against $M_{\rm tid}$ for all (top) and crossed (bottom) subhaloes.

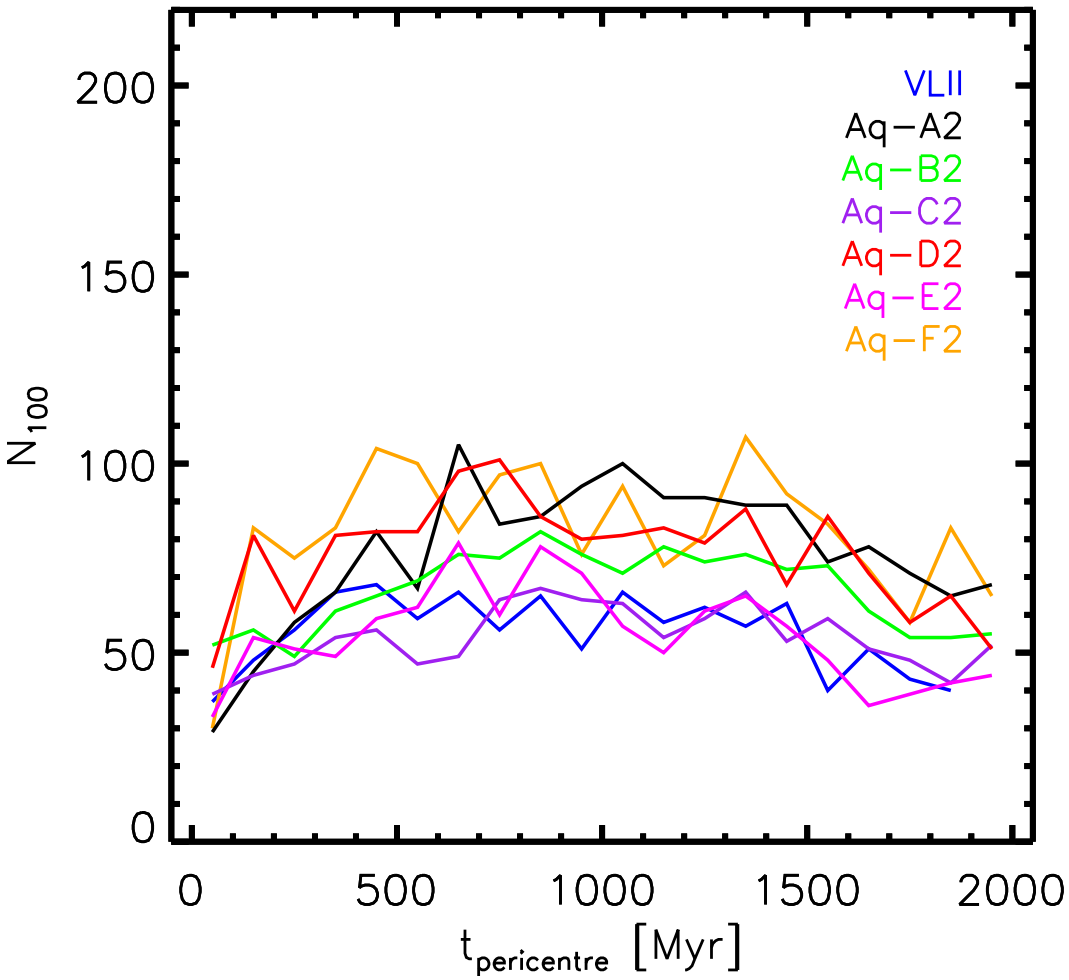

Figure 2.3.10: Distribution of pericentric time $t_{\mathrm{pericentre}}$, time of reaching the closest pericentre, for crossed subhaloes. Multiple pericentre passages are not included.

"Don't be satisfied with stories, how things have gone with others. Unfold your own myth."

- Jalaluddin Rumi

3

Milky Way's disc vertical heatings

3.1 Galaxy N-body model

Prior to the numerical analysis, we need to set up our desired galaxy models as a distribution of particles which include disc, bulge, DM halo and also the satellite component. As mentioned earlier, one of the most important aims of this work is to resolve the dynamical properties of the Galactic disc in the absence of any bias originating from a system which is not originally in equilibrium.

3.1.1 Multi-component Milky Way galaxy

In the past two decades there have been a number of attempts to generate initial conditions (IC) for multi-component spiral galaxies that include a disc, a bulge and a DM halo component, and producing a distribution of particles which follow particular density profiles. We have tested a few such attempts, however the true equilibrium and steady state of the disc component is questionable. For this study we take advantage of a recent code (GalIC) which employs a different approach to the made-to-measure method: constructing ICs for multi-component axisymmetric systems via an iterative scheme (Yurin and Springel, 2014).

The stellar disc component has an exponential radial profile while for the vertical direction an isothermal profile is adopted

$$\rho_{\rm d})R, z+[\quad \frac{\rm M_d}{5\pi z_0 h^2} \exp\left(\quad \frac{R}{h}\right) \operatorname{sech}^2\left(\frac{z}{z_0}\right) \tag{3.1}$$

In the above equation h and z_0 correspond to the radial scale length and the thickness of the disc; the total mass of the disc is represented by $M_{\rm d}$. For the scaling of the disc surface density, we use the value of the thin disc at the solar neighbourhood $\Omega_{\rm sol}$ proposed by Just and Jahreiß (2010) , which is then converted into $M_{\rm d}$ via

$$\rm M_d\ [\ \ 3\pi\Omega_{sol} h^2 \exp\left(\frac{R_0}{h}\right) \tag{3.2}$$

where R_0 [9 kpc is supported by Gillessen et al. (2009) and Reid et al. (2014). The value for the radial scale length h is chosen to be 2.8 kpc. Since the disc mass is not sensitive to the scale length over a large range, when fixing the local surface density, a strong influence from smaller scale lengths as discussed in recent literature is not expected. The GalIC code allows us to constrain the kinematical preferences of axisymmetric components. For the disc, we use the ratio of the radial and vertical velocity dispersions σ_R/σ_z which converges to a unique solution during the IC construction. The bulge follows a spherically symmetric and isotropic Hernquist profile (equation 3.4). The DM halo is set up in two stages. The first step consists of using properties of our DM halo such as λ, c and $\rm V_{200}$ (the spin parameter, concentration and total circular velocity of the system at r_{200}) extracted from the seven simulations. These quantities together with the employed cosmology allows us to infer the total mass (disc+bulge+DM halo) of the system, $M_{\rm tot}$, using

$$\rm M_{tot}\ [\ \ \frac{V_{200}^3}{21\, G H_0}. \tag{3.3}$$

The spin parameter λ, which determines the size of the disc, possesses a range of values for different haloes and is dependent on the concentration. Since we would like to have similar disc profiles among all simulations, this quantity is calculated such that the discs have similar scale lengths. These systems lie in the low spin parameter range. The code takes a reverse procedure and using the inputted λ together with the disc mass fraction $\rm m_d$, it calculates the scale length of the disc (e.g. Mo, Mao, and White 1998; Springel, Di Matteo, and Hernquist 2005a). In

the second step, the code uses the technique where a matching Hernquist profile is created for our desired NFW halo. This profile has a similar density profile to NFW in the inner part while falling off steeper in the outer regions according to

$$\rho_{\rm hern})r+[\quad \frac{M_{\rm hern}}{3\pi}\frac{a}{r)a\,0\;\;r+^3}, \tag{3.4}$$

where $M_{\rm hern}$ is the total mass of the halo and a is the scale radius of the Hernquist profile. Springel, Di Matteo, and Hernquist (2005a) introduced a method for constructing a Hernquist model with a density profile which matches that of a particular NFW profile. This is achieved by associating a Hernquist DM halo with total mass ($M_{\rm hern}$) same as the NFW halo mass within r_{200} where scale lengths are related via the NFW halo concentration

$$a\;[\quad r_{\rm s}\sqrt{3]ln)2\,0\;\;c+\quad c/)2\,0\;\;c+a} \tag{3.5}$$

We used this approach to generate the matching Hernquist potential for the parent haloes and employ them in the orbit integration analysis. We also found negligible deviations between the orbits of subhaloes in the NFW and the corresponding Hernquist haloes of the order of less than few percent. All the DM haloes in this study are generated with a spherical density profile for simplicity, while the original profile from the cosmological simulations are non-spherical, i.e. prolate/oblate/triaxial, (Allgood et al., 2006).

Some of the quantities used for the set up of the initial conditions are listed in table 3.1.1. The λ ranges from 0.021–0.028 depending on the simulation and the DM halo which is constructed. Each system contains 10, 0.5 and 4 million particles for the disc, the bulge and the halo, respectively. According to Khoperskov et al. (2007) an insufficient number of disc particles could damp out the modes by introducing noise; hence 10 million disc particles allow for a physically reliable analysis of the disc.

3.1.2 Satellite model

The satellites with $M_{\rm tid} \sim 10^8\ M_\odot$ are generated using their $M_{\rm tid}$, $c_{\rm tid}$ and $r_{\rm s}$ calculated in section 2.3 together with the distribution function introduced

Table 3.1.1: The characteristics of the components for the Milky Way. N represents the number of particles for the component, while the subscripts d,b and h correspond to the disc, bulge and the halo. The solar neighbourhood surface density $\Omega_{\rm sol}$ together with the thin disc scale height and scale radius, z_0 and h correspond to the model proposed by Just and Jahreiß (2010).

Quantity	Value
$\Omega_{\rm sol}$	39.9 $M_\odot$pc^{-2}
h	2.8 kpc
z_0	277 pc
M_d	3.42 $\pm$ 10^{10} $M_\odot$
σ_R/σ_z	1.5
N$_d$	10 million
a$_b$	0.35 kpc
M_b	1.9 $\pm$ 10^{10} $M_\odot$
N$_b$	0.5 million
M_{200}	1.77 $\pm$ 10^{12} $M_\odot$
λ	0.021-0.028
N$_h$	4 million

by Widrow (2000) and implemented in Lora et al. (2013) for a cuspy NFW profile. We need to employ a cut-off radius for the satellites due to the infinite cumulative mass of NFW profile at $r \simeq$ | ; hence $r_{\rm tid}$ was chosen. All the satellites for this study are represented using 50,000 particles.

3.2 N-body code

The numerical simulations in this paper are performed using the efficient parallelised N-body particle-mesh code SUPERBOX-10 (Bien, Brandt, and Just, 2013). Since the individual gravitational interaction of particles from similar/different components, also known as two-body relaxation, has a time-scale of the order of the Hubble time we can regard them as collisionless (Binney and Tremaine, 2008). SUPERBOX-10 has three nested grids at different resolution for *each* galaxy, where the inner most grid with the highest resolution allows the inner dense structure of every galaxy to be resolved and the outer most grid contains the whole simulation and coincides for all galaxies. Each grid is divided into cubic cells and we decided to use n^3 cells with n=256 instead of 128 in order to reduce the energy conservation error to $< 0.4\%$ after 4 Gyr of evolution. The size of each cell depends on the radius of the grid

$R_{grid,i}$ and calculated as

$$d_{cell} [\frac{3 R_{grid,i}}{n \quad 5}. \tag{3.6}$$

The outermost grid contains all the particles in the simulation and hence has a size of few hundred kpc. The calculation of the potential is performed via transforming the cell densities into potential using parallelised Fast Fourier Transform (FFT) together with Green's function. The computation time scales as Nlog N in the case of FFT while direct calculation scales as N^2. In addition, the orbital integration of the particles are done using a leapfrog method and a constant time step (Fellhauer et al., 2000). It is important to choose an appropriate time step, as it plays an essential role in the force calculations; it needs to be short enough that a typical particle in the inner most grid moves a maximum of one cell during the step, which was chosen to be 0.1 Myr.

In order to enhance the resolving power of the vertical structure of the galactic disc, SUPERBOX-10 takes advantage of a flattening parameter q which flattens the middle grid along the z-axis. This technique improves the calculation of the acceleration in the vertical direction. For all our simulations we use similar grid radii for the Milky Way galaxy; $R_{inn} [4.6$ kpc, $R_{mid} [41$ kpc and $R_{out} [611$ kpc. The cell size of each grid are $d_{inn} [1.139$ kpc, $d_{mid} [1.35$ kpc and $d_{out} [5.1$ kpc. The flattening factor q has the value of 0.3, which increases the resolution of the middle grid in the z direction by a factor of ≈ 3.3. According to the work by Just et al. (2011) the effective resolution in the force calculations using the particle-mesh code is $d_{eff} [d_{cell}/3$. Hence we reach a resolution of 40 parsecs in the vertical direction of the entire disc in the middle grid.

Each satellite has its own 3 grids, where the sizes of the inner and middle grids are chosen as $2r_s$ and $2r_{tid}$; the outer grid has the same size as the MW system, 500 kpc.

3.3 The simulations

3.3.1 Runs

In the current version of SUPERBOX-10 code, only the FFT section which is responsible for the conversion of cell densities into potentials, is parallelised. The parallelisation is achieved via the aid of Message Passing Interface (MPI), allowing

for the communication and transfer of information between different processors. Each run was carried out using in total 64 processors distributed among 8 CPU nodes. In total each isolated simulation took approximately 14 days to complete.

The simulations were performed on the Milky Way supercomputer, funded by the DFG SFB 881 subproject Z2 and hosted and co-funded by the Jülich Supercomputing Center (JSC).

3.3.2 Analysis of the disc

The disc is subject to being shifted, tilted and distorted with respect to the original coordinate system due to evolution and mostly the bombardment by the satellites. Therefore, we defined at each time-step a new coordinate system for the analysis of the disc structure, by moving the origin to the density centre of the host galaxy. The velocities of the disc particles are corrected for the density centre velocity, then the coordinate system is rotated to correct for the tilt. It turned out that the angular momentum vector of the disc is the most robust measure of the disc rotation axis and disc plane. The positive z-axis is rotated to the angular momentum vector of the disc, taking into account all disc particles. For an exponential disc with flat rotation curve 95% of the disc mass and 87% of the angular momentum is enclosed within $6h$ [25 kpc. The tilt angle ranges from less than 1° for most of our simulations to ≈ 5° in the case of Aq-F2 with satellites.

For the analysis of the disc structure we study the temporal evolution of the solar neighbourhood defined by $7.5< R < 9.6$ kpc, and the radial profile at the end of the simulation. We evaluate in radial rings, $z_{\rm mean}$ which provides a measure of the mean value of the disc z-coordinate, in order to check the disc orientation and identify bending modes. We have checked that the inner disc is well-aligned with the new coordinate system in all cases. The root-mean-square of the disc z-coordinate in the solar neighbourhood calculated via

$$z_{\rm rms} [\sqrt{<)z \quad z_{\rm mean}{}^{+2} >}, \quad z \quad z_{\rm mean} \geq 3\,{\rm kpc} \tag{3.7}$$

which is a measure of the disc thickening and the square of the vertical velocity dispersion are measures of disc's vertical heating. We neglect any disc particle with $z \quad z_{\rm mean} \sim 2$ kpc for this analysis in order to avoid any outliers.

3.3.3 Isolated system

The multi-component Milky Way galaxy was evolved in isolation – in the absence of satellites – for 2+2 Gyr in the case of all 7 simulations. The initial 2 Gyr is for the purpose of reaching an equilibrium state while the latter 2 Gyr is to have a control group for comparison to the systems with satellites. The isolated evolution allows the components to adapt to their environment and also reach the equilibrium and steady state. Fig. 3.3.1 shows the time evolution of 10-90% Lagrange radii of the Aq-B2 system (disc+bulge+halo) in isolation. This quantity represents the spherical radii at which 10-90% of the total mass are enclosed. The inner 50% of the system that extends beyond the disc does not show signs of expansion/contraction during 4 Gyr. The outer regions of the halo have only less than 6% of expansion, which is expected due to the cut-off as the outer parts are loosely bound and few particles could, in principle, escape.

The number density plot of the disc from the Aq-B2 simulation is represented in Fig. 3.3.2 where starting at top-left we observe the system at -2, 0, 1 and 2 Gyr. After 4 Gyr of evolution the disc appears in steady state and we do not observe any strong instabilities within the disc. Also the red crosses correspond to centre of mass of the bulge which coincides with the disc centre of mass.

Fig. 3.3.3 shows a few quantities describing the dynamics of the isolated system Aq-B2 – a fair representative of our simulation sample. In the top two rows different line colours correspond to the system at -2, -1, 0, 1 and 2 Gyr of evolution as function of radial distance across the disc. Starting from the top left, the surface density Ω of the disc is represented and stays unchanged throughout 4 Gyr of evolution in isolation. We observe some fluctuations at the outer disc, $R > 21$ kpc, in the initial 1 Gyr which dampens afterwards. The next plot shows the Toomre parameter Q, a measure of the disc stability and is calculated as

$$Q \; [\quad \frac{\sigma_R \kappa}{4.47 G \Omega}, \tag{3.8}$$

where σ_R and κ represent the radial velocity dispersion and the epicyclic frequency

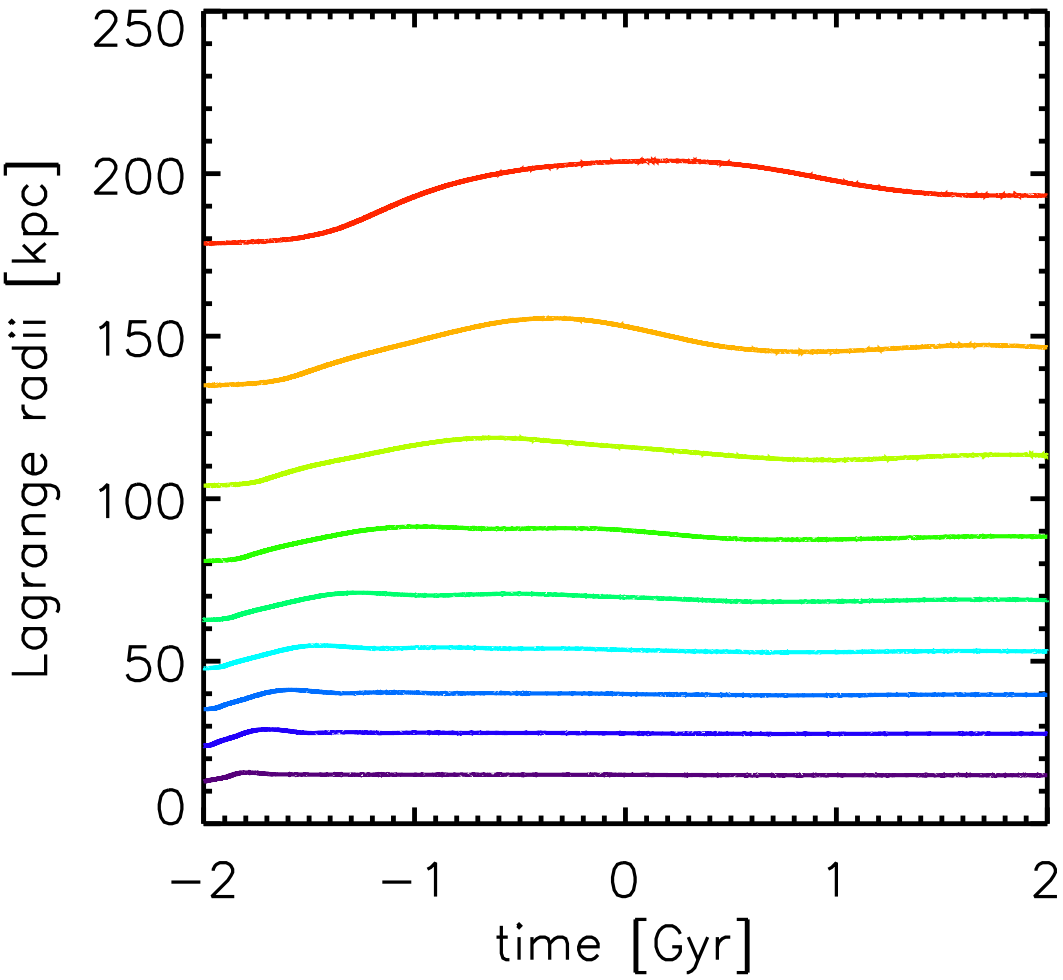

Figure 3.3.1: 10-90% Lagrange radii of the isolated MW for Aq-B2 simulation. The 10% radii corresponds to the lowest value (dark purple) while 90% has the highest value (red) and the remaining colours in between show the 20-80% Lagrange radii from bottom to top.

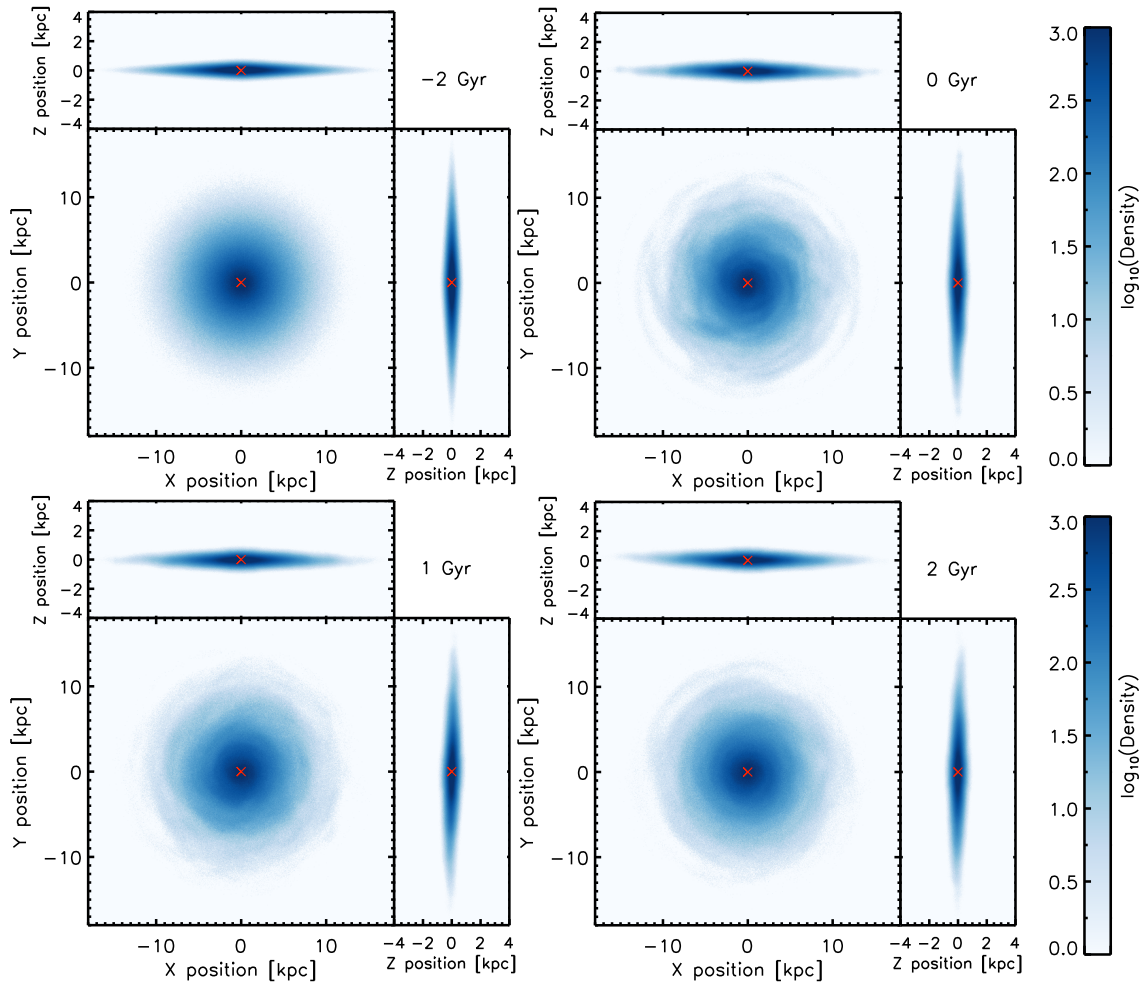

Figure 3.3.2: The number density plot for the isolated system in x-y, x-z and y-z view. *From top left:* Aq-B2 simulation at initial time (-2 Gyr), 0, 1 and 2 Gyr of evolution. The red cross represents the centre of the mass of the bulge component.

of the disc particles. Initially the disc has a Q value of 1.5 at the solar neighbourhood increasing to $\approx$ 2.5 after few hundred Myr. The initial increase of σ_R is still one of the caveats of the GalIC code. The vertical velocity dispersion σ_z shows an increase of 45% at R [26 kpc after 4 Gyr while for the solar neighbourhood we observe an increase of less than 12% only. $z_{\rm mean}$ stays close to 0 for the inner 10 kpc as expected from a system in equilibrium. The next plot shows the time evolution of $z_{\rm rms}$ in the solar neighbourhood. The increase of the disc thickness after 3 Gyr is $\approx$ 15 % which reaches 320 pc while in the case of the σ_z^2 in the solar neighbourhood a vertical heating of 40 km^{2}s^{-2} (16%) is seen in the last 3 Gyr.

3.3.4 Full simulations

After obtaining an isolated system which satisfies the equilibrium criteria, we add the subhalo candidates using their extracted initial positions and velocities at t=0 Gyr. Since there is no massive satellite with $M_{\rm tid} > 6 \pm 21^8 M_\odot$ closer than 20 kpc (see Fig. 2.2.2), we don't expect an unphysical reaction of the disc by the sudden implementation of the satellites. Each of the seven systems were simulated for 2 Gyr.

3.4 Results

In this section we discuss the results obtained from the analysis of satellites' impact on the disc. We focus on the vertical heating of the Galactic disc due to the infalling satellites, expressed in terms of thickening the disc and increasing the vertical velocity dispersion of disc particles. In the first part, we discuss the heating in the solar neighbourhood, 7.5 kpc $< R <$ 8.5 kpc, for the duration of 2 Gyr; in the second part we analyse the impact of satellites across the whole disc's radial range. In the last part, we argue about the relevance of the orientation of satellites' distribution to the vertical heating measurements for two cases of Aq-D2 rotated along the x and y axes by 90 degrees.

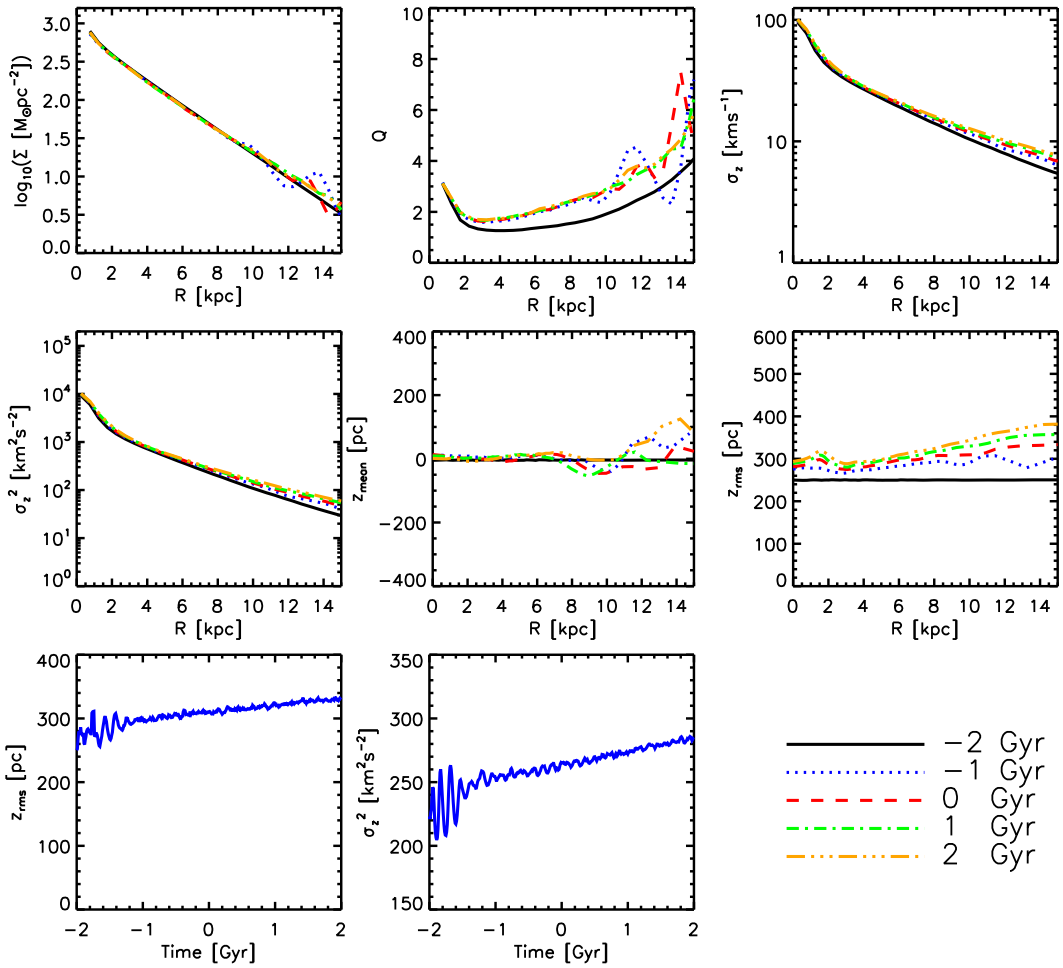

Figure 3.3.3: The properties of the disc in the isolated Aq-B2 simulation. From the top left as function of radial distance from the centre of disc: Surface density of the disc Ω, Toomre parameter Q, vertical velocity dispersion σ_z, vertical σ_z^2, mean disc height $z_{\rm mean}$, root-mean-square thickness $z_{\rm rms}$. The lines represent the results at -2, -1, 0, 1 and 2 Gyr. The two bottom figures show the $z_{\rm rms}$ and σ_z^2 in the solar neighbourhood, $7.5 < \mathrm{R} < 8.5$, as function of time.

3.4.1 Solar neighbourhood

In this study, taking advantage of our high resolution analysis of the Milky Way disc, we are able to resolve the structure of the disc at 40 pc scale together with the large number of disc particles. The next results focus on the time evolution of the $z_{\rm rms}$ and vertical velocity dispersion in the solar neighbourhood for all the particles lying in the radial range 7.5 - 8.5 kpc from the disc centre. The top panel of Fig. 3.4.1 shows the time evolution of the root-mean-square of the disc height subtracted by the initial values, $z_{\rm rms,t}$ $z_{\rm rms,0}$ for systems with satellites (solid) and isolated (dashed) at the solar neighbourhood for VLII (blue), Aq-B2 (green), Aq-D2 (red) and Aq-F2 (orange). During the initial 0.4 Gyr the thickening is minimal since no massive subhalo with $M_{\rm tid} \sim 10^9$ $M_\odot$ crosses the disc within this period (Fig. 2.2.2). The reason for this lack of interaction in the first 0.4 Gyr may be the result of initial conditions at z=0, since we did not take into account the tidal mass loss which already happened for satellites in the inner region of the host halo (Nagai and Kravtsov, 2005). In order to take this into account, we will compare the dynamical evolution in the simulations in addition to a delayed heating by 0.5 Gyr. Aq-F2 reaches a maximum thickness difference of 75 pc ($\approx$ twice as much as in the isolated case at 2 Gyr), while in the remaining simulations the thickness increases by 30 pc at most.

As mentioned in section 1, the primary aim of this study is to understand the contribution of realistic cosmological satellites to the heating of the Galactic disc. This process can be best quantified using the squared vertical dispersion σ_z^2 of the disc particles. The most reliable measurement of the vertical heating of the Milky Way disc has been obtained for the solar neighbourhood (e.g. Holmberg et al. 2007, 2009) with the value of $d)\sigma_z^2 \# dt$ [83 km^{2}s^{-2}Gyr^{-1} following a power law with exponent 3γ [2.17 for σ_z^2 which means a constant heating rate. The time evolution of the quantity $\sigma_{z,t}^2$ - $\sigma_{z,0}^2$ (the difference between the system at time t and the initial time when the satellites are added) for systems with satellites and isolated in the solar neighbourhood is presented in the bottom panel of Fig. 3.4.1 with $\sigma_{z,0}^2$ [371 km^{2}s^{-2}. As with the evolution of $z_{\rm rms}$ we observe a more significant heating in the case of Aq-F2 – 25% at 2 Gyr compared to initial – while only very small fluctuations are seen for the remaining simulations. The self-heating of the disc is very small, on a scale of $\approx$ 21 km^{2}s^{-2}Gyr^{-1}. The dotted and dash-dotted lines, respectively, represent the observed vertical heating rate in the solar neigh-

bourhood and the observed value allowing for 0.5 Gyr delay, which accounts for possible initial underestimation of heating due to mass loss of subhaloes already located in the inner halo. The jumps observed in the velocity dispersion due to massive mergers are seen in other simulations, where such mergers cause visible signatures in the velocity dispersion profiles (Martig, Minchev, and Flynn, 2014).

Aq-D2 has twice as many subhaloes with $M_{\rm tid} \sim 10^9\ M_\odot$ compared to Aq-B2 which, in theory, translates into a larger impact. We also observe twice as much heating compared to the isolated cases between the two simulations in the solar neighbourhood.

The mean values of $z_{\rm rms,t}$ $z_{\rm rms,0}$ for all 7 simulations with satellites (solid), with satellites except Aq-F2 (dotted) and isolated system (dashed) are shown in the top panel of Fig. 3.4.2 with their subsequent 1σ statistical dispersion around the mean. The blue, pink and green colours correspond to all the simulations with satellites, with satellites except Aq-F2, and for the isolated system, respectively. We observe a very shallow increase of the thickness with time in all systems after the initial 0.4 Gyr. The mean value of all the systems with satellites experiences an increase of 35 pc compared to the initial state and only less than 10 pc – $\approx$ 40% – compared to the isolated system. If we exclude the impact from Aq-F2, the thickening in the solar neighbourhood from satellites is almost indistinguishable from the isolated case.

According to the bottom panel of Fig. 3.4.2 there exists a slow increasing trend of the mean value of $\sigma^2_{z,t} - \sigma^2_{z,0}$ for all systems. The heating rates for the initial 1 Gyr are 20, 15 and 10 $\rm km^2 s^{-2} Gyr^{-1}$ for systems with satellites, with satellites except Aq-F2, and the isolated system, respectively. These reduce to 15 $\rm km^2 s^{-2} Gyr^{-1}$ for all the systems later. This means the rate at which the vertical dispersion increases with time in the solar neighbourhood decreases slightly after 1 Gyr. Not taking into account Aq-F2, the difference between the mean heating due to satellites and the isolated systems is very small and only 5 $\rm km^2 s^{-2}$ at 2 Gyr. The 1σ dispersion region from all the simulations (blue) reaches 50 $\rm km^2 s^{-2}$ at the final snapshot which is 35% of the observed value of 144 $\rm km^2 s^{-2}$. The additional heating for subhaloes below $10^{10} M_\odot$ is of the order of $\approx$ 10-15%. The dotted and dash-dotted lines represent the observed vertical heating rate in the solar neighbourhood and the observed value

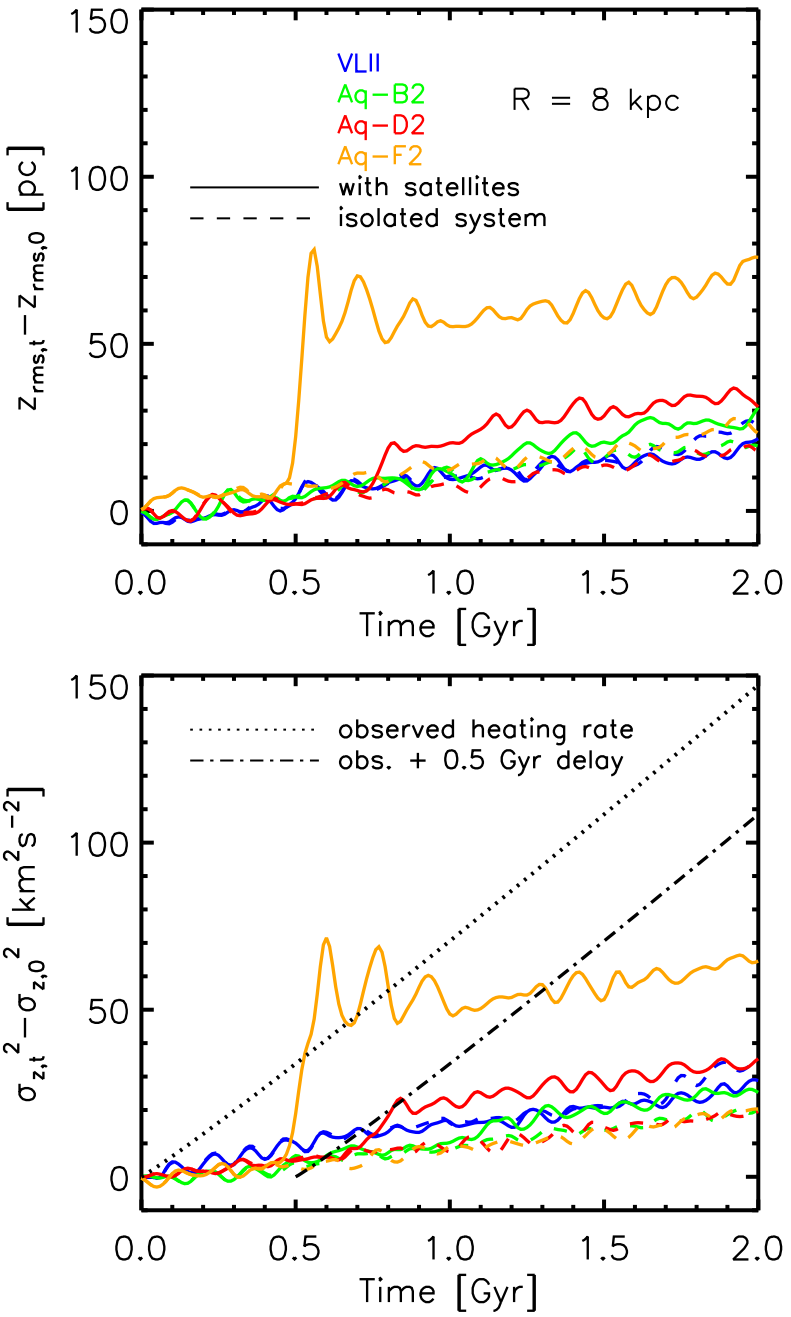

Figure 3.4.1: *Top:* Time evolution of the root-mean-square of the disc thickness subtracted by the initial value for systems with satellites (solid) and isolated (dashed) for VLII (blue), Aq-B2 (green), Aq-D2 (red) and Aq-F2 (orange) simulations in the solar neighbourhood. *Bottom:* The time evolution of the difference of the disc vertical heating for VLII (blue), Aq-B2 (green), Aq-D2 (red) and Aq-F2 (orange) simulations. The dotted and dash-dotted lines represent the observed vertical heating rate in the solar neighbourhood and the observed value with 0.5 Gyr delay, respectively.

with 0.5 Gyr delay, respectively. The Aq-F2 simulation suggests, in order to reach the observed heating rate, that a few encounters per Gyr of LMC type satellites with pericentres below 20 kpc are required. Our result fails by more than 3σ to reproduce the observed heating rate. These results are consistent with the recent observational work by Ruchti et al. (2015). Using the *Gaia*-ESO spectroscopic survey, they found no evidence for a significant dark matter disc in the MW and that the Galactic disc has had a rather quiescent merger history for the past ≈ 9 Gyr.

3.4.2 The impact across the disc

In addition to the solar neighbourhood, the global vertical heating across the whole disc was also investigated and is presented in this section.

The root-mean-square of the disc height at 2 Gyr subtracted by the initial values, $z_{\rm rms,t}$ $z_{\rm rms,0}$, as function of radial distance from the disc centre for systems with satellites (solid) and isolated (dashed) for VLII (blue), Aq-B2 (green), Aq-D2 (red) and Aq-F2 (orange) simulations are shown in the top panel of Fig. 3.4.3; this quantity is calculated in radial bins of equal particle numbers. The solid and dashed lines illustrate the systems with satellites and the isolated control systems; the results correspond to the time of 2 Gyr which is the final snapshot of our simulations. The deviation between the control system and the system with satellites is mainly visible in the outer disc. In Aq-F2 the flare starts at the solar neighbourhood and reaches a thickening of 550 pc at R [26 kpc. For the VLII simulation we observe that the thickening of the isolated case is slightly larger than the case with satellites at some radii, however we still observe a positive increase of thickness compared to 0 Gyr time. As seen in previous studies (Ardi et al., 2003) we observe a small flaring in the outer parts of the disc which is amplified with the presence of the satellites; the particles which reside in the outer regions are less strongly bound to the disc and require less energy to be displaced. Aq-A2, Aq-C2 and Aq-E2 show the least thickening due to infalling satellites.

The bottom panel of Fig. 3.4.3 illustrates the vertical heating of the disc,$\sigma^2_{z,t}$ $\sigma^2_{z,0}$. Aq-F2 dominates the heating – reaching $\approx$ 200 km^{2}s^{-2} in the outer parts. The peak at $R < 5$ kpc corresponds to a very small increase in the velocity dispersion (from 100 kms^{-1} to 102 kms^{-1} at the centre). The

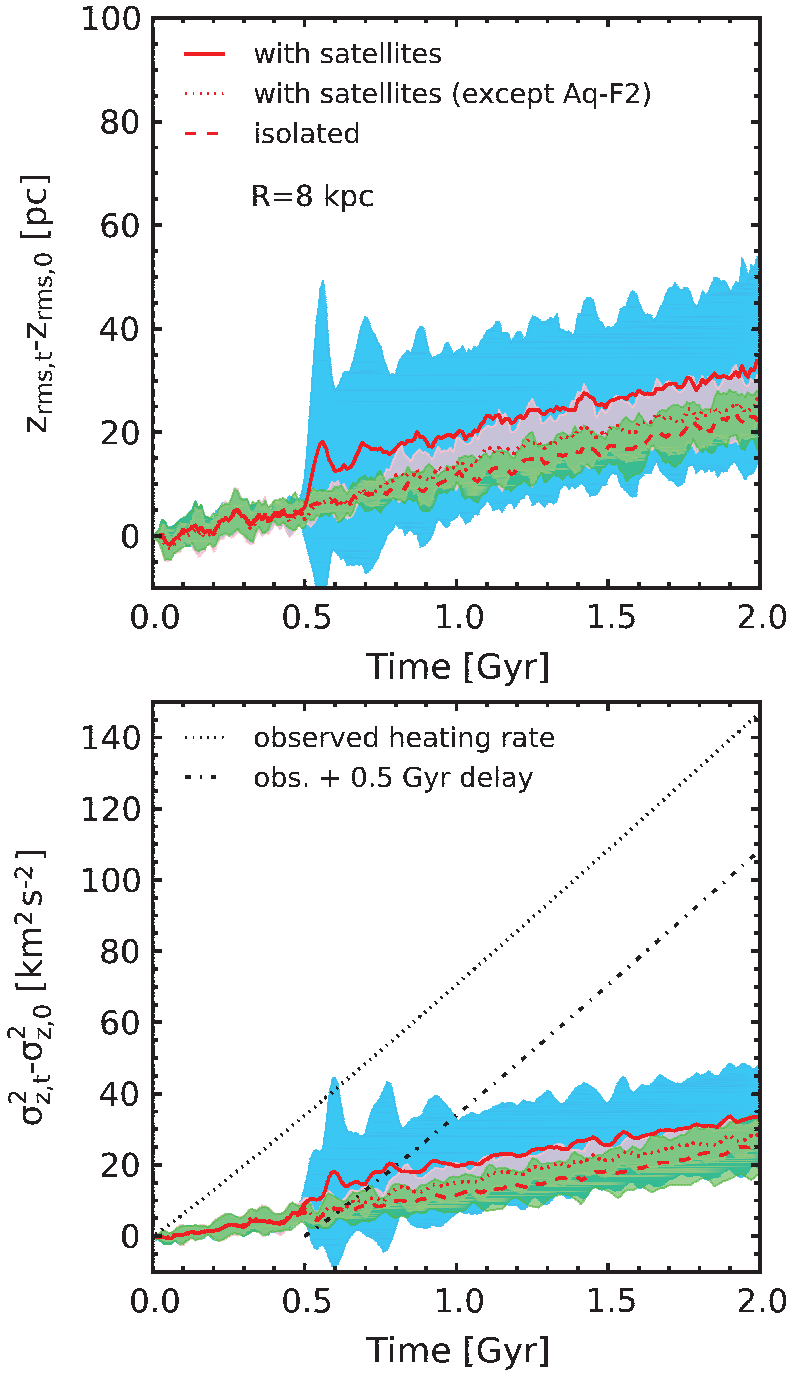

Figure 3.4.2: The mean difference of vertical heating between t [3 and t [1 Gyr together with their 1σ statistical dispersion region of all 7 systems with satellites (solid, blue), with satellites except Aq-F2 (dotted, pink) and isolated (dashed, green). The dotted and dash-dotted lines represent the observed vertical heating rate in the solar neighbourhood and the observed value with 0.5 Gyr delay.

observed vertical heating in the solar neighbourhood after 2 Gyr (Holmberg et al., 2009) is represented as a filled diamond while, if we allow for 0.5 Gyr of delay, we obtain the heating represented by the empty diamond in Fig. 3.4.3 with values of 144 and 108 km^2s^{-2}, where 144 corresponds to twice the vertical heating rate of 72 $km^2s^{-2}Gyr^{-1}$. The $\sigma^2_{z,0}$ at R [26 kpc has a value of 40 km^2s^{-2} and therefore the maximum heating in the outer parts reaches $\approx$ 500% compared to the initial value; excluding Aq-F2, we only have less than 130%.

Similar to the behaviour seen in the solar neighbourhood, Aq-B2 and Aq-D2 possess comparable heating rates with 20 km^2s^{-2} extra heating for Aq-D2. Aq-D2 has half of its pericentric passages during the initial 1.1 Gyr while the remaining passages occur during the final 0.1 Gyr. Hence it appears that the heating due to subhaloes with $10^9\ M_\odot < M_{\rm tid} < 10^{10}\ M_\odot$ contributes only to $\approx$ 40 km^2s^{-2} of heating for R $>$ 4 kpc.

The top panel of Fig. 3.4.4 demonstrates the mean $\sigma^2_{z,t}$ - $\sigma^2_{z,0}$ value of all seven simulations with satellites (solid), with satellites except Aq-F2 (dotted) and the isolated system (dashed), across the radial range at t [3 Gyr. The shaded regions present the 1σ statistical dispersion in each bin. The impact of Aq-F2 is seen as the difference of the dotted and solid lines which increases as we move towards the outer regions. The mean disc height of all simulations with satellites increases by 150 pc after 2 Gyr at 15 kpc and including the dispersion this value reaches 340 pc; while the isolated systems only have an increase of 50 pc at this radius, corresponding to self thickening of about 14%. Aq-F2 increases the mean value by an additional 70 pc in the outer 15 kpc regime.

The mean value of the vertical heating between 0 and 2 Gyr for all systems across the disc is shown in the bottom panel of Fig. 3.4.4. The shaded areas correspond to the 2σ dispersion around the mean for the subsequent systems – blue, pink and green. For all the systems with satellites, the mean value lies around 40 km^2s^{-2} across the disc at $R > 5$ kpc, while the simulations excluding Aq-F2 possess less than 20 km^2s^{-2} in the outer parts. The solar neighbourhood heating at R [9 kpc of 144 km^2s^{-2} and the value 108 km^2s^{-2} taking into account 0.5 Gyr delay are represented as filled and open diamonds. The 1σ dispersion in the solar neighbourhood reaches only 50 km^2s^{-2}. We observe a specific heating almost independent of galactocentric

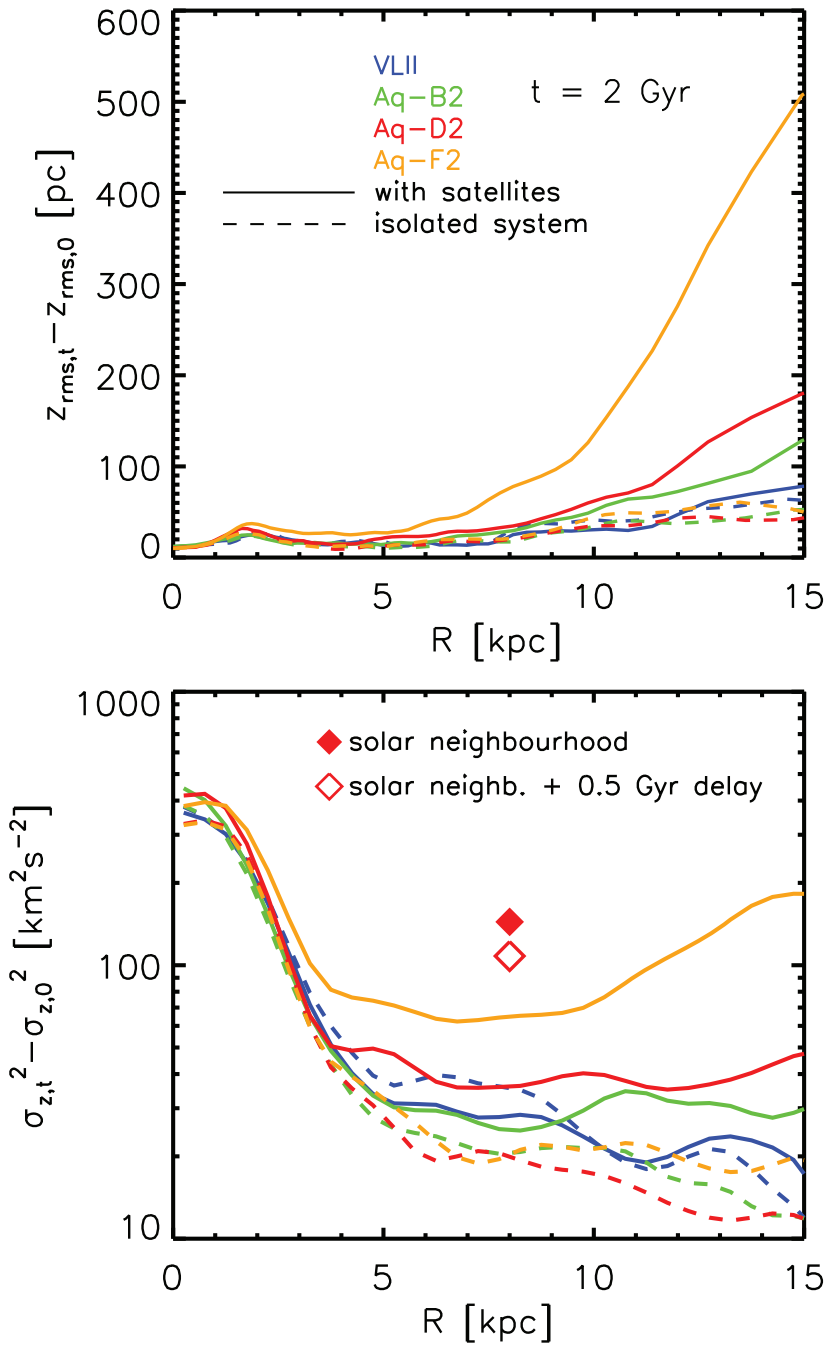

Figure 3.4.3: *Top:* The difference of root-mean-square of the disc height $z_{\rm rms}$ at 2 and 0 Gyr for systems with satellites (solid) and isolated (dashed) for VLII (blue), Aq-B2 (green), Aq-D2 (red) and Aq-F2 (orange). *Bottom:* The difference of the disc vertical heating between t [3 and 0 Gyr for VLII (blue), Aq-B2 (green), Aq-D2 (red) and Aq-F2 (orange). Filled and open *diamonds* represent the observed value of vertical heating in the solar neighbourhood and the observed value with 0.5 Gyr delay.

distances for R $\sim$ 4 kpc. More energy is deposited to the inner parts; although, this region is not strongly perturbed due to both higher surface density and velocity dispersion. However, the outer parts with lower surface density experiences stronger relative heating together with flaring.

3.4.3 Effect of satellites infall orientation

In this section we present our results from the analysis of the impact of the orientation of satellites distribution relative to the disc on the measured vertical disc heating. For this purpose we only use the Aq-D2 simulation, which has the second most number of satellites candidates (23) above 10^8 $M_\odot$ and the most candidates with $M_{\rm tid} \sim 10^9$ $M_\odot$. This simulation is believed to be representative of our simulation suites and shows a typical level of anisotropy (Fig. 2.3.8). We decided to consider two additional cases of different orientation that consist of rotating the satellites' frame by 90 degrees along the x axis, hereafter case B, and also performing the similar rotation along the y axis, case C. The original orientation is regarded as case A. These rotations correspond to changing the disc's original axis of rotation, z, to rotation about the y (case B) and x axis (case C).

The top panel of Fig. 3.4.5 shows the difference of the disc vertical heating, $\sigma^2_{z,t}$ – $\sigma^2_{z,0}$, for the original Aq-D2 case A (red), case B (blue), case C (green) and isolated (black) systems across the disc at the end of the simulation, t [3 Gyr. The heating across the disc is very similar. Only in case C the outer disc shows a reduced heating. The time evolution of the same quantity in the solar neighbourhood is shown in the bottom panel of Fig. 3.4.5. The difference is minimal during the initial 0.4 Gyr when no massive subhalo crosses the disc. The time evolution differs by 10 km^{2}s^{-2} around 1 Gyr. However, the final heating rate is the same in all cases. Hence, the impact of orientation plays a minor role in the vertical heating of the Galactic disc.

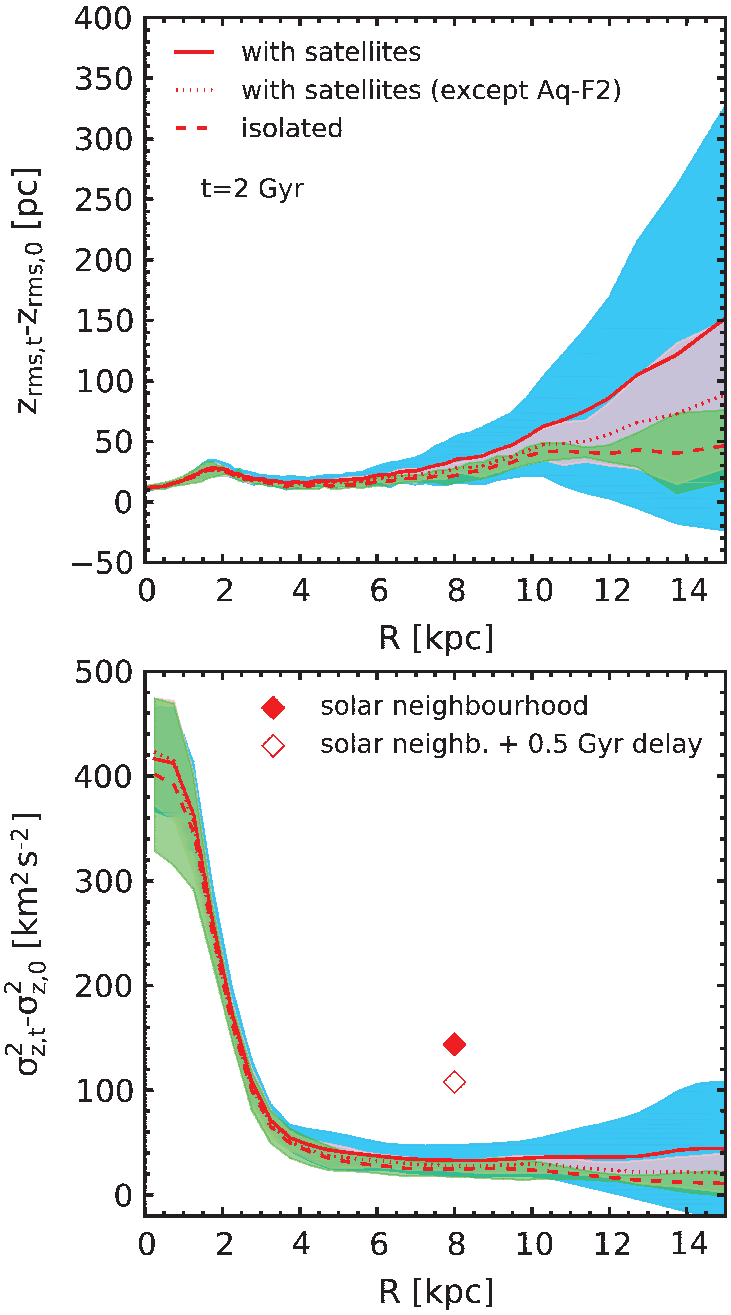

Figure 3.4.4: *Top:* The mean root-mean-square of the disc height for all 7 systems with satellites (solid), with satellites except Aq-F2 (dotted) and all 7 isolated system (dashed) at 2 Gyr. *Bottom:* The mean difference of the disc vertical heating between t [3 and 0 Gyr for similar systems as in the top panel. The shaded regions correspond to the 1σ dispersion around the mean value for all 7 systems with satellites (blue), with satellites except Aq-F2 (pink) and isolated systems (green). Filled and open *diamonds* represent the observed value of vertical heating in the solar neighbourhood and the observed value with 0.5 Gyr delay.

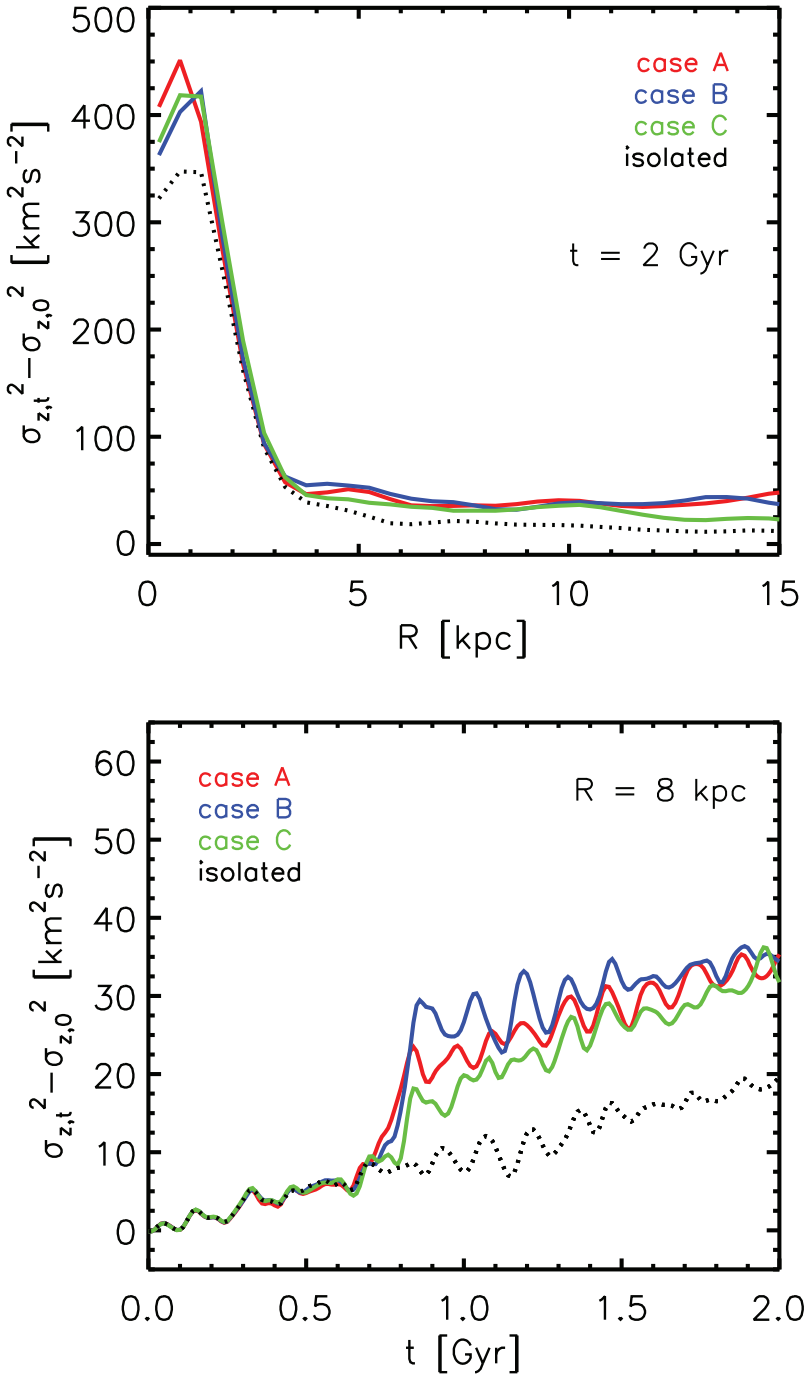

Figure 3.4.5: *Top:* The difference of the disc vertical heating for original Aq-D2 case A (red), case B (blue), case C (green) and isolated (dotted) systems across the disc at the final snapshot, t [3 Gyr. *Bottom:* the time evolution of the difference of the disc vertical heating for similar systems as in the top panel in the solar neighbourhood.

"Sell your cleverness and buy bewilderment."

- Jalaluddin Rumi

4 Mode analysis

4.1 Introduction

Structure formation in the Universe governed by the Σ cold dark matter (ΣCDM) paradigm, pursues a hierarchical model. Smaller DM (sub)haloes merge in order to build up larger objects (e.g. White and Rees 1978; Moore et al. 1999). Such mergers occur on different scales, ranging from minor (1:3 - 1:50 of total mass) to major (mass ratios $\gtrsim$ 1:3 of total galaxy mass) mergers. These events are believed to impact the dynamics of galaxies, and even change their morphology (e.g. Baugh, Cole, and Frenk 1996; Borne, Bushouse, Colina, et al. 1999; Hernández-Toledo, Avila-Reese, Conselice, and Puerari 2005; Lotz, Jonsson, Cox, and Primack 2010; Kannan, Macciò, Pasquali, Moster, and Walter 2012). Current hydrodynamical cosmological simulations, which account for different small and large scale physical processes such as radiative cooling, stellar and AGN feedback, star formation, magnetic fields etc., are able to reproduce spectrum of galaxies with different morphologies, including ellipticals, barred and unbarred spirals (Vogelsberger et al., 2014).

Observations of galaxies in local and high redshift Universe, have shown a

high fraction of barred spirals (e.g. van den Bergh et al. 1996; Abraham et al. 1999). The properties of the host disc galaxy are affected by the presence of a bar, which possesses strong gravitational potential. For instance, redistribution of stars/gas within the bar's corotation radius, together with evolution of the bulge are strongly correlated with the bar (e.g. Hohl 1971; Kormendy 1982; Athanassoula 2005). Early N-body simulations were successful in generating spiral galaxies, hosting bars (e.g. Miller, Prendergast, and Quirk 1970; Ostriker and Peebles 1973; Athanassoula and Sellwood 1986). Initially, the bar mode instability was assumed to be responsible for the bar-formation. However, later works (e.g. Mark 1971, 1974; Sellwood 2000) have proposed other possible mechanisms.

Noguchi (1987) concluded that tidal interactions with external fly-bys, are able to induce bar structures. According to observations, larger number of barred spirals are found in denser environments, such as galaxy clusters, than in isolation. This supports the importance of tidal interactions for bar-formation (Elmegreen, 1999). Toomre's swing amplification (Toomre, 1981) can be regarded as the main mechanism for the growth of such perturbations, if the satellite has a mass ratio greater than 1:1 of the host disc mass. However, in the case of lower mass fly-bys, such encounters, have the capability to induce perturbations in the disc plane, which can be amplified after few disc rotations (Goldreich and Lynden-Bell, 1965; Julian and Toomre, 1966).

This chapter is aimed at investigating the importance of satellite galaxy encounters on the bar-formation in the Milky Way via N-Body simulations. In order to have realistic initial conditions (ICs), we use a distribution of subhaloes extracted from cosmological simulations, which are likely to host Milky Way-like galaxies (Diemand et al., 2008; Springel et al., 2008). We explore different subhalo mass ranges in order to quantify the relevance of such quantity. The spectral analysis employed for this chapter follows that described by Polyachenko (2005).

4.2 Cosmological initial conditions

In order to account for a realistic image of satellite galaxies' infall to the Milky Way's disc, the distribution of subhaloes was withdrawn from the Aquarius cosmological suite (e.g. Springel et al. 2008; Diemand et al. 2008). For the purpose

of this section, we only focus on the Aq-D2 run, regarded as a fair representative of a Milky Way-like halo. The characteristics of Aq-D2, such as $M_2 11$ and $r_2 11$, are listed in Tab. 2.1.2.

As mentioned earlier we are interested in subhaloes with a chance of passing through the Galactic disc. The detailed procedure of identifying these candidates, is mentioned in chapter 2. Statistics of Aq-D2 subhaloes distribution are shown in Tab. 2.2.1. This run has 23 candidates with $M_{\rm tid} \geqslant 21^8 M_\odot$ out of which 4 have masses $\geqslant 21^9 M_\odot$. A complete comparison of different properties of crossed and total populations, is provided in chapter 2.

The host halo, in which these candidates would be inserted, has a slightly different enclosed mass (M_{200}) than Aq-D2's host. Therefore, we needed to rescale the phase-space properties of the subhaloes, together with their mass, following the recipe mentioned in section 2.1, in order to have a physically sensible analysis. The scaling factor has a value of $f{=}M_{200,\text{Aq-D2}}/M_{200,\text{W7-009}} \gg 1.37$. As discussed earlier in section 2.1, all the DM subhaloes, including the host halo, would follow a NFW density profile.

4.3 N-body Models

This section includes the description of the models recruited for setting up our desired Milky Way model which consists of a disc, a bulge and a DM halo component together with the satellite galaxies.

4.3.1 Galaxy

Our 3-component model is adopted from Widrow et al. (2008); Kuijken and Dubinski (1995), and consists of the stellar disc, bulge, and dark matter halo. The disc is exponential, with radial scale length $R_{\rm d}$ [3.=kpc and truncation radius 15 kpc. The radial velocity dispersion σ_R is approximately exponential with a central value σ_{R0} [251 km/s and a radial scale length R_σ [$3R_{\rm d}$. We accept a value for the solar neighbourhood radius of 8 kpc (e.g. Gillessen et al. 2009; Reid et al. 2014). The complete list of characteristics for disc, bulge and halo

Table 4.3.1: The characteristics of disk+bulge+halo for our Milky Way model. N represents the particle number for the component and M for the enclosed mass, while the subscripts d,b and h correspond to the disc, the bulge and the halo. The solar neighbourhood surface density $\Omega_{\rm sol}$ together with the thin disc scale height and scale radius, z_d and $R_{\rm d}$ correspond to the model proposed by Just and Jahreiß (2010). The dispersion values σ_R and σ_{R0} correspond to the solar and central radial velocity dispersion of the disc. In case of the bulge, $R_{\rm b}$ and σ_b are the effective radius and central velocity dispersion.

Quantity	Value
$\Omega_{\rm sol}$	50 $M_\odot$pc^{-2}
$R_{\rm d}$	2.8 kpc
$z_{\rm d}$	300 pc
M_d	4.2 ± 10^{10} $M_\odot$
σ_R	35 kms^{-1}
σ_{R0}	140 kms^{-1}
N$_{\rm d}$	7×21^6
R$_{\rm e}$	0.64 kpc
$\sigma_{\rm b}$	272 kms^{-1}
$M_{\rm b}$	1.02 ± 10^{10} $M_\odot$
N$_b$	2.6×21^6
M_{200}	1.29 ± 10^{12} $M_\odot$
$r_{\rm s}$	17.25 kpc
r_{200}	229.3 kpc
N$_h$	$=36 \times 21^6$

components are listed in Tab. 4.3.1.

The bulge component takes a density profile of the form (Sérsic, 1968)

$$\rho_{\rm b})r+[\quad \rho_{\rm b}\left(\frac{r}{R_e}\right)^{-p} {\rm e}^{-b(r/R_e)^{1/n}} \ , \tag{4.1}$$

where r is a spherical radius. The scale density $\rho_{\rm b}$, can be replaced by the bulge velocity scale

$$\sigma_{\rm b} \leq \left\{5\pi G n b^{n(p-2)} \quad]n)3 \quad p\text{-}\text{a}R_e^2\rho_{\rm b}\right\}^{1/2} \ . \tag{4.2}$$

Here, $\sigma_{\rm b}^2$ corresponds to the depth of the gravitational potential associated with the bulge. In addition, we require n [2.22899 and $p \propto 1.6$, in order to define the bulge density profile. We have employed a truncated NFW profile for the halo, with the truncation radius $r_{\rm h}$ [33=4 kpc. The bulge component dominates the rotation curve at $R < 1.12$ kpc, despite the halo having a more cuspy profile.

The total circular velocity profile (solid curve) and the contribution from each component (dashed/dotted) are shown in the top panel (a) of Fig. 4.3.1. The bulge dominates at radii $R \lesssim 2.6$ kpc, while the halo takes over at $R > 21$ kpc. At $R \gg 7\,\mathrm{kpc}$, where contribution of the disc component reaches the maximum, the force from the halo is about 2/3 of that from the disc in the Galactic plane.

Panel (b) of Fig. 4.3.1 presents the angular velocity profile $^{-})R+$. In addition, the positions of the inner and outer Lindblad resonances ILR and OLR are shown as $^{-} \equiv \kappa/3$. For a given pattern speed $^{-}{}_{p}$, ILR is calculated using

$$^{-}{}_{p}\,[\;\; ^{-}{}_{\mathrm{pr}})R+\leq {}^{-})R+\;\; \frac{2}{3}\kappa)R+. \tag{4.3}$$

The quantity, $^{-}{}_{\mathrm{pr}})R+$is responsible for determining a precession rate of nearly circular orbits. Hence, it can be referred to, as 'precession' curve. For the basic model, the curve diverges weakly at $R \simeq 1$ as $R^{-\alpha/2}$ with $\alpha \gg 1.6$.

The lower panel (c) of Fig. 4.3.1 demonstrates the Toomre Q profile

$$Q\,[\;\; \frac{\kappa\sigma_R}{4.47G\Omega_{\mathrm{d}}}\;, \tag{4.4}$$

where Ω_{d} represents the disc surface density. The minimum $Q_{\mathrm{min}}\,[\;\; 2.9$ resides at $R\,[\;\; 6.=\mathrm{kpc}$.

4.3.2 Satellites

In order to insert the selected satellite candidates into our N-body simulations, each subhalo needs be generated as a distribution of particles following their corresponding NFW profile. We use eqs. 2.7, 2.8, 2.9 and 2.4 from section 2.3, in order to calculate the required quantities such as tidal radius r_{tid}. Such a profile has an infinite cumulative mass at $r \simeq |\;\;$; therefore, we use the satellites' r_{tid}, as the cut-off radius. The satellites are represented using 50,000 particles.

4.3.3 Codes

Initial conditions of stars for single mass simulations have been generated by the 'GalactICS' code provided by Widrow et al. (2008). Numerical calculations have

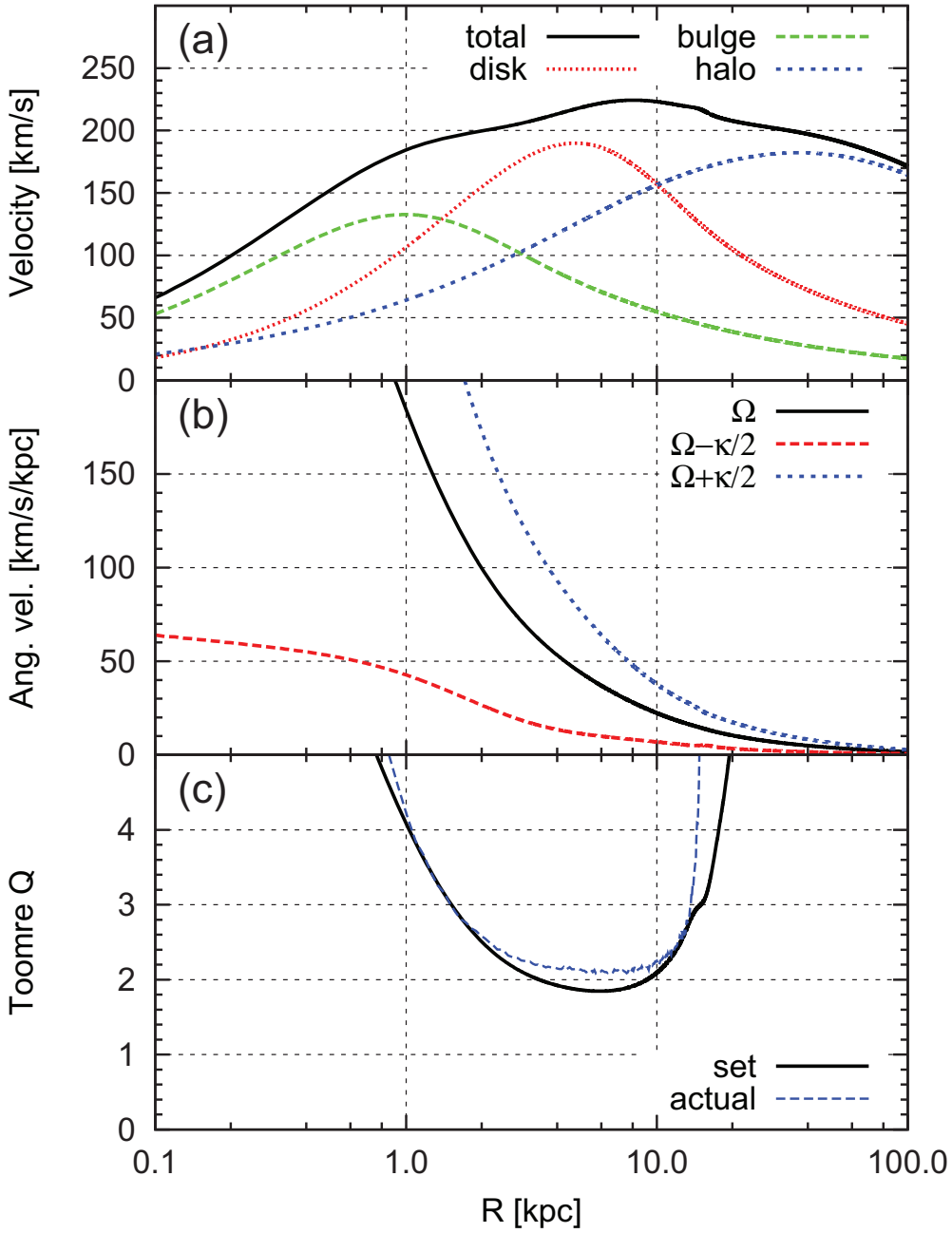

Figure 4.3.1: Initial profiles for the basic model: (a) the total circular velocity and its components due to disc, bulge, and halo; (b) angular velocity $^{-})R+$and curves $^{-})R+\equiv \kappa)R+/3$; (c) Toomre Q initially set to GalactICS and one actually obtained in the simulations.

been performed with two different codes: SUPERBOX-10 and `bonsai2`. For a description of the efficient parallelised collisionless N-body particle–mesh code SUPERBOX–10, a thorough introduction is provided by Bien, Brandt, and Just (2013). For the description of employed factors such as grid size, time-step etc., please refer to section 3.2.

In addition, we take advantage of a modified version of the recently developed N-body Tree–GPU code implementation `bonsai2` (Bédorf et al., 2012a,b). The opening angle used had a value of $\theta = 0.5$, accompanied by an individual gravitational softening of 10 pc. `bonsai2` employs the leap-frog integration scheme with a fixed time–step Λ t = 0.2 Myr. To analyse the snapshot data we use the self coded Tree-GPU based gravity calculation routine `ber-gal0`[1] (Zinchenko et al., 2015) with similar opening angle.

The current set of simulations was carried out with the GPU version of the code using local GPU clusters available at the authors' institutions (ARI: `kepler`, MAO: `golowood`, NAOC: `laohu`) and also the specially dedicated for SFB 881 ("The Milky Way System") GPU cluster `MilkyWay`, located at the Jülich Supercomputing Centre in Germany.

4.3.4 Runs

Tab. 4.3.2 contains parameters of runs for the basic model. It is worthwhile to mention, that the MW halo components simulated using `bonsai2` have multimass halo particles in order to achieve a better resolution in the bar region. For this, we modified the GalactICS code utilizing the strategy described in Dubinski et al. (2009). Such resolution is achieved by assigning low-mass particles to the inner dense region and high-mass particles to the outer part. In the region between 0.1 and 1 kpc, the number density ratio of our multimass and single mass runs varies from 10 to 100, thus the effective numerical resolution there is enhanced by this factor.

The subscript 'm' corresponds to the simulations, which are only mass–rescaled using eq. 2.1; while, the remaining simulations are fully–rescaled (eqs. 2.1, 2.2

[1] `ftp://ftp.mao.kiev.ua/pub/users/berczik/ber-gal0/`

Model	$n_{\rm sat}$	Delay [Myr]
B-0m	–	–
B-1	1	–
B-1m	1	–
B-4	4	–
B-4m	4	–
B-1-110Myr	1	+110
B-1-500Myr	1	−500

Table 4.3.2: Parameters of runs: $n_{\rm sat}$ is a number of satellites; 'm' denotes only mass-rescaled subhaloes while the remaining simulations are fully – mass, positions and velocities – rescaled. Total number of the galaxy particles $N_{\rm tot}$ [27.86 M, and number of particles in components are $N_{\rm d}$ [7 M, $N_{\rm b}$ [2.6 M $N_{\rm h}$ [=36 M, number of stars in each satellite galaxy $N_{\rm sat}$ [61 K.

and 2.3). In the case of simulations marked using 'B-1', we use the most massive candidate from Aq-D2 simulation with non-scaled mass $M_{\rm tid}$ [$4.67 \pm 21^9 M_\odot$. For runs marked as 'B-4', the 4 most massive Aq-D2 crossed satellites with $M_{\rm tid} > 21^9 M_\odot$ were employed.

We also have two additional runs, B-1-110Myr and B-1-500Myr. The former has the same re-scaling as B-1, however, with 110 Myr delay, roughly corresponding to the time difference between the two initial pericentre passages of B-1 and B-1m runs. This was introduced in order to evaluate the importance of full and mass–rescaling for runs with similar initial impact parameters. For the latter, we used the 500 Myr snapshot of B-1 run and started the simulation at this point with the aim of understanding the relevance of noise level on the bar-formation time.

4.4 Simulations

Prior to a detailed analysis of the simulation results, it is beneficial to present the features of our runs. The simulations were carried out for 4 Gyr, capturing two pericentric passages. Fig. 4.4.1 shows the orbits of Aq-D2 most massive candidate from our four runs with this satellite. The orbits from the two simulations with 110 and 500 Myr are also shown. There exists a 110 Myr difference between the first pericentre passages of B-1 and B-1m runs. The pericentre distances have the values r [3.7 and 4.6 kpc, occurring at 0.85 and 0.96 Gyr, respectively. This means, the

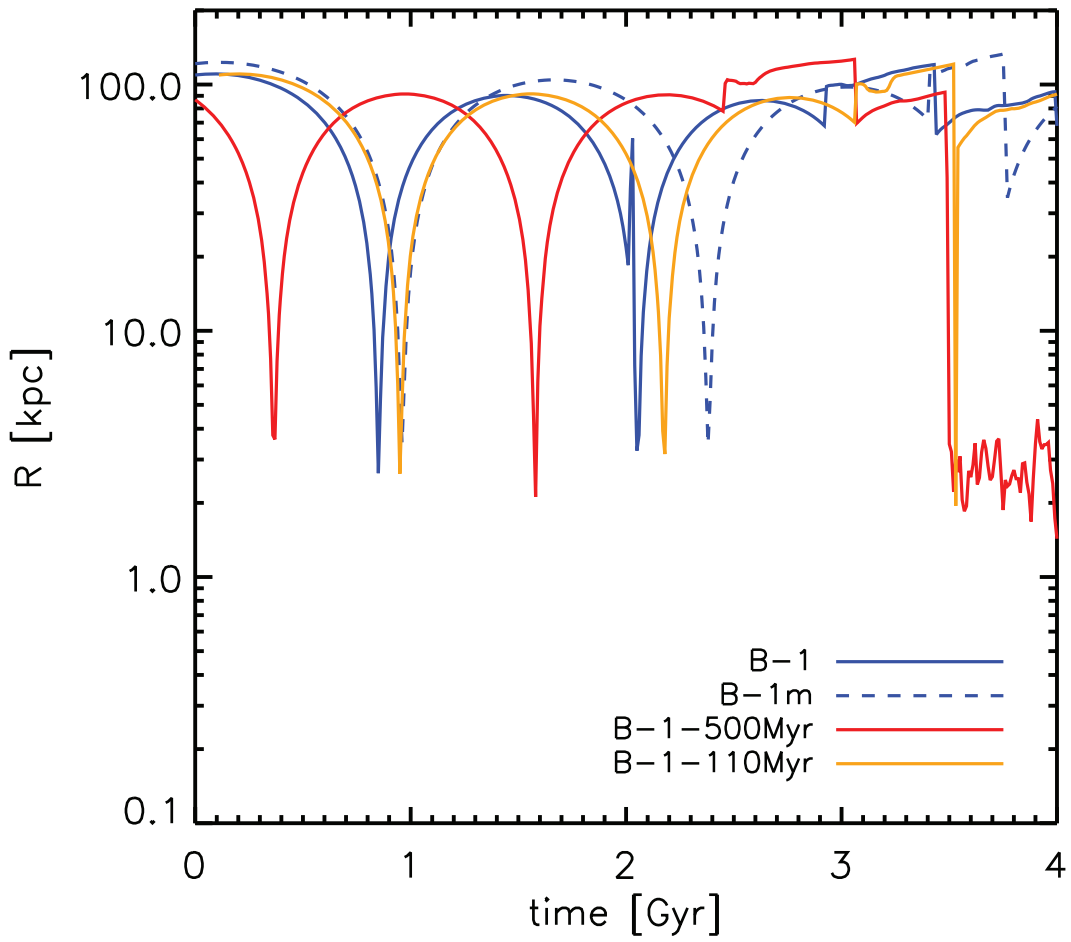

Figure 4.4.1: The orbit of satellite from our 4 runs with the most massive candidate as function of time.

inner parts of the disc are prone to any impact by the infalling satellites.

Fig. 4.4.2 represents the contour plots of the projected disc surface density along 3 planes for t [1 (left) and 4 Gyr (right) from B-1 run. The disc initially starts from an unperturbed component and by the end of the simulation, we have a distinct bar which extends radially to 5 kpc. If viewed along the x–z plane, an X-shaped bulge, reaching 2 kpc vertically above and below the disc plane, is evident at t [5 Gyr.

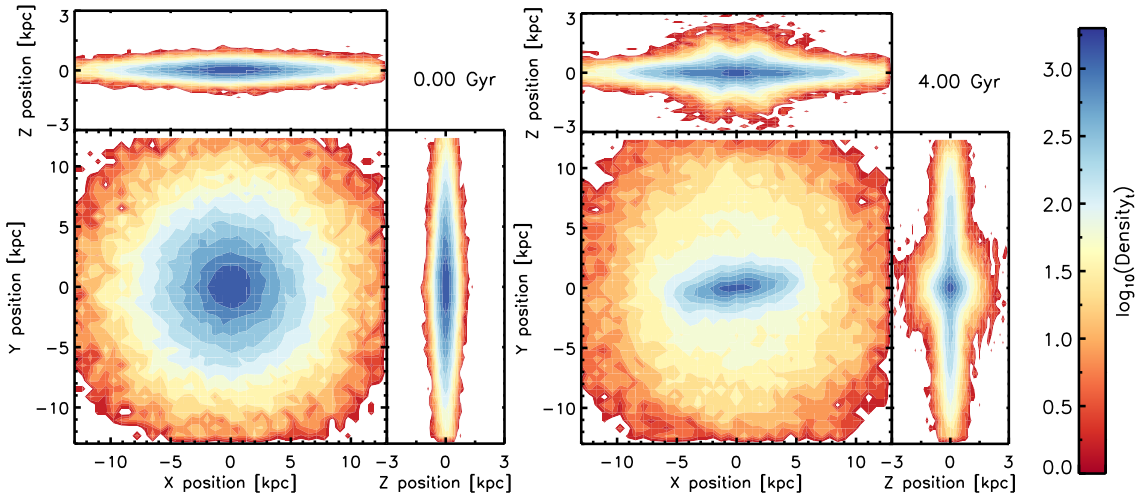

Figure 4.4.2: The contour plots of the projected disc number density for the B-1 run in x-y, x-z and y-z view at 0 (left) and 4 Gyr (right). The colour coding has a logarithmic scale.

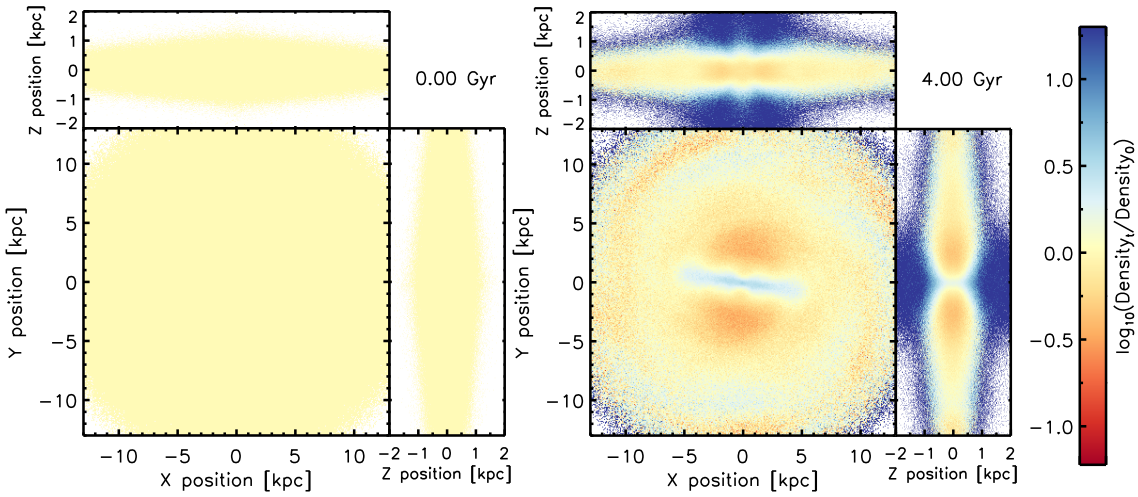

Figure 4.4.3: The relative projected disc surface density for the B-1 run in x-y, x-z and y-z view at 0 (left) and 4 Gyr (right). The colour coding has a logarithmic scale.

The relative projected number surface density of the disc, with respect to the initial value, is shown in Fig. 4.4.3 for the run B-1. This normalisation is aimed at highlighting perturbations across the whole disc. The orange-to-red colour displays density deficit compared to the initial state, while the excess of density is depicted in blue. Other features, such as spiral arms, are also visible in the outer regions of the disc plane.

4.4.1 Bar mode

In order to measure the strength of the bar, we take advantage of the triaxiality parameters I_{yy}/I_{xx} and I_{zz}/I_{xx}, with I being the components of the inertia ellipsoid along the x, y and z axes

$$I_{xx} [\sum_j m_j x_j^2 , \quad I_{yy} [\sum_j m_j y_j^2 \quad \text{and} \quad I_{zz} [\sum_j m_j z_j^2 . \tag{4.5}$$

Where m_j are masses of disc stars; index j spans only the particles residing within a 3 kpc radius. Using this quantities, the bar strength is defined as

$$B)t+[\quad 2 \quad I_{yy}/I_{xx}. \tag{4.6}$$

We apply eq. 4.6 to our simulations and show in Fig. 4.4.4 the time evolution of the bar strength for the isolated B-0m run, together with all the fully-rescaled (top) and mass-rescaled (bottom) simulations. The pattern can be broken down into three phases: the lag at low amplitudes, linear growth and the plateau. First point to notice is that all simulations show a similar trend and consist of the mentioned three parts. The initial low amplitude phase can be regarded as the stage, when different perturbations are getting enhanced/destroyed constantly and lasts for $\approx$ 0.5–0.8 Gyr. The major differences between the runs occur during the linear growth rate regime. The bar-formation is independent of the presence of satellites; since, B-0m run shows the linear growth, which initiates around 1.1 Gyr. This is an indication that the disc from our runs is actually unstable against the bar mode, although possessing a minimum Toomre value $Q_{\min} [\ 2.9$. In the case of B-1 and B-4 runs, the bar growth starts at $\approx$ 0.9 Gyr, while having a very similar amplitude.

This expresses that the most massive candidate exerts the majority of the perturbation and the presence of other three infalling satellites does not contribute

significantly in this case. The passage of satellites enhances the bar instability mode earlier than the isolated run. However, if we compare these two runs with their mass–rescaled counterparts, a so–called *delayed* bar growth is observed. This delay, compared to the fully–rescaled runs, is ≈ 0.5 and 0.9 Gyr for B-1m and B-4m, respectively. The B-1-110Myr simulation with 0.11 Gyr delay, actually causes a bar delay although possessing similar scaling to the B-1 run. In the case of B-1-500Myr run, which starts from the B-1's 0.5 Gyr snapshot, a very similar behaviour as B-0m is measured. The black dash–dotted line corresponds to a growth rate ω [4 Gyr^{-1}.

A Fourier analysis of quantities, such as surface density and velocity of disc particles, allows a deeper insight into the contribution of different modes towards the observed features. For this purpose, we compute the disc's surface density together with the radial, vertical and tangential velocity wave amplitudes, in the case of m [3 mode, according to recipe by Polyachenko et al. (2016), using

$$\Omega)R,t+[\quad \frac{2}{\delta M_\mathrm{d})R+}\sum_j m_j \mathrm{e}^{-im\theta_j} \ , \tag{4.7}$$

$$V_R)R,t+[\quad \frac{2}{\delta M_\mathrm{d})R+}\sum_j m_j v_{R,j} \mathrm{e}^{-im\theta_j} \ , \tag{4.8}$$

$$V_z)R,t+[\quad \frac{2}{\delta M_\mathrm{d})R+}\sum_j m_j v_{z,j} \mathrm{e}^{-im\theta_j} \quad \text{and} \tag{4.9}$$

$$V_\phi)R,t+[\quad \frac{2}{\delta M_\mathrm{d})R+}\sum_j m_j v_{\phi,j} \mathrm{e}^{-im\theta_j} \ . \tag{4.10}$$

The summation is taken over disc particles within a ring near radius R. The disc particle's mass is denoted as m_j, while $M_\mathrm{d})R+[\ \sum_j m_j$ is the total mass within a ring with width δR near R. The input from different global modes could possess R–dependence across the whole disc. However, for the inner regions of the disc, the bulk of the contribution belongs to a single dominant mode. Therefore, the dependence on R can be eliminated via

$$A_{\tilde{\Sigma}})t+[\quad \frac{2}{M_\mathrm{d})R_\mathrm{d}+}\sum \delta M_\mathrm{d})R+\Omega)R,t+, \tag{4.11}$$

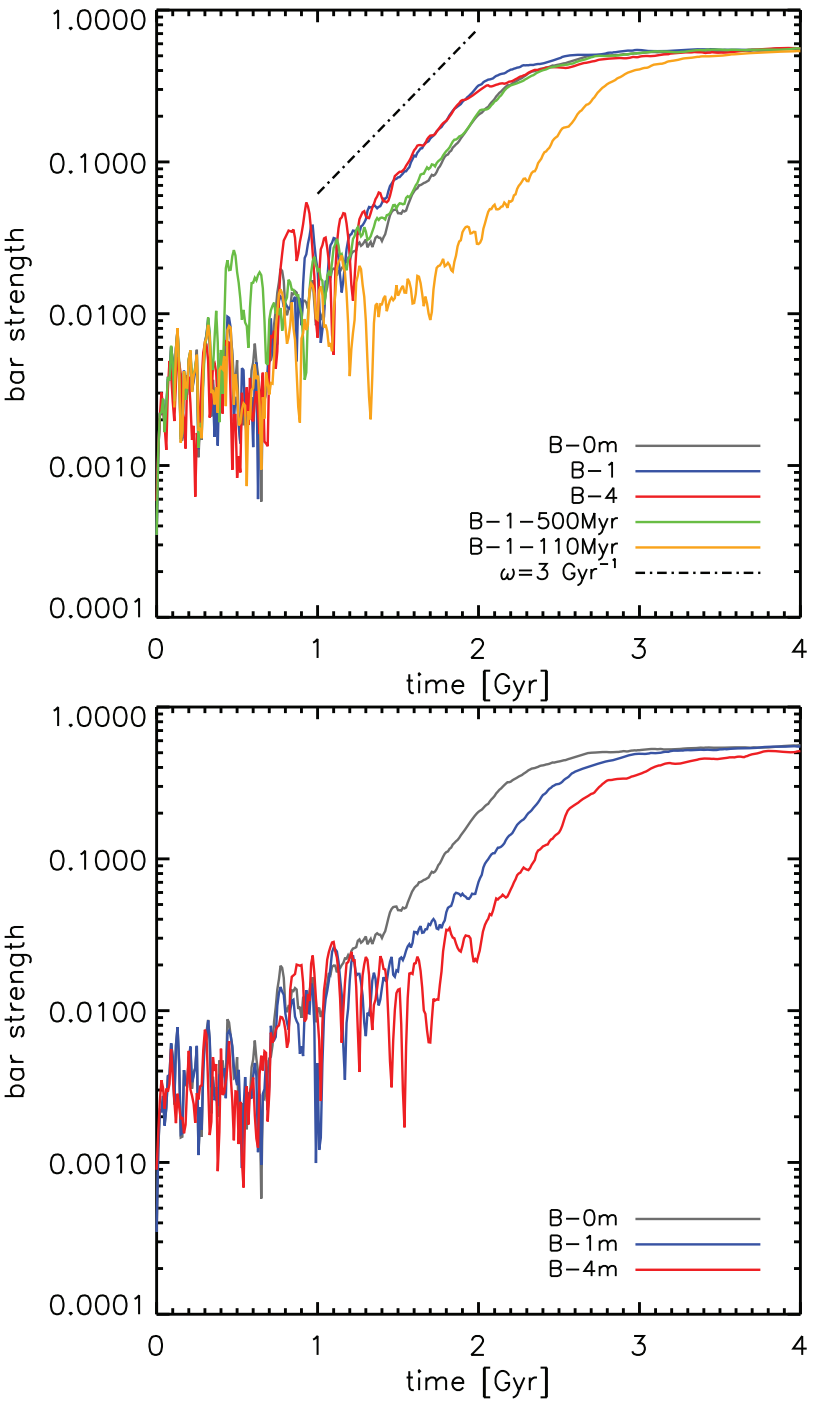

Figure 4.4.4: Bar strength $B)t+$in fully–scaled (top) and mass–rescaled (bottom) together with the isolated B-0m runs. Dash-dotted line shows growth of the bar strength with rate 4 Gyr^{-1}.

$$A_{\tilde{V}_R})t+[\quad \frac{2}{M_{\rm d})R_{\rm d}+}\sum \delta M_{\rm d})R+V_R)R,t+, \tag{4.12}$$

$$A_{\tilde{V}_z})t+[\quad \frac{2}{M_{\rm d})R_{\rm d}+}\sum \delta M_{\rm d})R+V_z)R,t+ \quad \text{and} \tag{4.13}$$

$$A_{\tilde{V}_\phi})t+[\quad \frac{2}{M_{\rm d})R_{\rm d}+}\sum \delta M_{\rm d})R+V_\phi)R,t+. \tag{4.14}$$

We have restricted these calculations to the particles within the disc scale length $R_{\rm d}$. Also, $M_{\rm d})R_{\rm d}+$corresponds to the total disc mass within $R_{\rm d}$, $2.24 \pm 21^{10} M_\odot$.

Fig. 4.4.5 shows the time evolution of amplitudes from eq. 4.11 and 4.12 for all the B-1 simulations, together with the isolated run. Comparing to Fig. 4.4.4, the velocity and surface density amplitudes show a much smoother profile in the lag region, also referred to as the shot noise phase. Yet, the bar delay/advancement are seen clearly for the case of mass–rescaled and fully–rescaled runs. We observe a slight time difference of ≈ 0.1 Gyr between $A_{\tilde{\Sigma}}$ and $A_{\tilde{V}_R}$, which is expected as the reaction time of the velocity space to perturbations/modes is different. The sudden jumps in the amplitude plots correspond to the pericentric passages of the satellites.

From Fig. 4.4.5, we identify three important moments during the bar-formation process, T_1, T_2 and T_3. T_1 marks the epoch when the bar amplitude – $A_{\tilde{\Sigma}}$ – experiences a sudden jump to ≈ 1.12 (1%). This moment has a value of ≈ 1.86 Gyr, and is regardless of satellite's presence (B-0m) and is the result of a strong random wave travelling towards the centre. The time at which the exponential growth of the bar initiates, corresponds to T_2. This value depends on the run with, $\approx 1.=$Gyr and ≈ 2.5 Gyr, for B-1 and B-1m. In the absence of satellites, $T_2 \quad T_1$ is expected to be small. Unless, the bar growth occurs relatively slow (Polyachenko, 2016). The end of exponential growth is identified as T_3. Any incoming perturbation due to the satellite's impact would not leave any trace, if the arrival time is before than T_1. The importance of such perturbation is relevant in case the passage occurs after the amplitude has reached 1% (T_1) and before T_2.

Tab. 4.4.1 shows the characteristics of our 7 simulations. This includes the pattern speed $^{-}{}_{p}$ measured at 3.6 Gyr, which is after the bar amplitude has reached its saturation level. The pattern speed ranges from 28–33 km/s/kpc. The bar mode

Model	$^{-}{}_{p}$ [km/s/kpc]	ω_B]Gyr^{-1}a	$\omega_{\tilde{\Sigma}}$]Gyr^{-1}a	$\omega_{\tilde{V}_R}$]Gyr^{-1}a
B-0m	30.0	3.29	3.29	3.39
B-1	28.9	3.59	3.32	3.35
B-1m	31.6	3.35	3.12	3.22
B-4	28.6	3.63	–	–
B-4m	31.2	3.92	–	–
B-1-110Myr	33.0	3.59	3.06	3.11
B-1-500Myr	29.8	2.99	2.92	2.93

Table 4.4.1: Characteristics of our 7 runs: $^{-}{}_{p}$ represents the pattern speed of the bar at 3.6 Gyr. ω_B, $\omega_{\tilde{\Sigma}}$ and $\omega_{\tilde{V}_R}$ show the bar growth rate calculated using bar strength, surface density and radial velocity amplitudes, respectively.

starts with $^{-}{}_{p} \approx 5$=km/s/kpc initially; during the bar growth the pattern speed decreases, and after reaching the plateau it experiences additional precession. The bar growth rate in Gyr^{-1} calculated using the bar strength, the surface density and the radial velocity amplitudes are represented as ω_B, $\omega_{\tilde{\Sigma}}$ and $\omega_{\tilde{V}_R}$, respectively. There exists a slight difference between the growth rates from different methods.

In order to grasp the details of the bar-formation and interactions with infalling satellites, it is useful to have a better visual and physical picture of the process. Fig. 4.4.6 demonstrates surface plots of the real part of eq. 4.8 for B-0m (bottom) and B-1 (top) runs, as a function of radial distance from the disc and time. The colour–coding corresponds to the amplitude, with a narrower range being chosen in order to observe the features easier. The periodic red/blue stripes, which are seen in both runs, show the bar growth. During the initial 0.6–0.7 Gyr the bar mode is absent, since we are still in the shot noise regime. Afterwards, the exponential growth of the bar occurs. The pericentric passage of the satellite results in a perturbation which travels outwards and initially possesses a rather constant amplitude across the disc. Such a mode becomes dominant in the outer regions of the disc as a two–armed spiral. As the disc evolves, the spiral becomes more tightly wound and after ≈ 3 Gyr, the bar becomes the dominant mode.

The same quantity is represented in Fig. 4.4.7 for B-1-500Myr (bottom) and B-1 (top) runs. The satellite from B-1-500Myr simulation, comes in 0.5 Gyr earlier than B-1. The pericentre crossing occurs during the shot noise phase. The bar growth

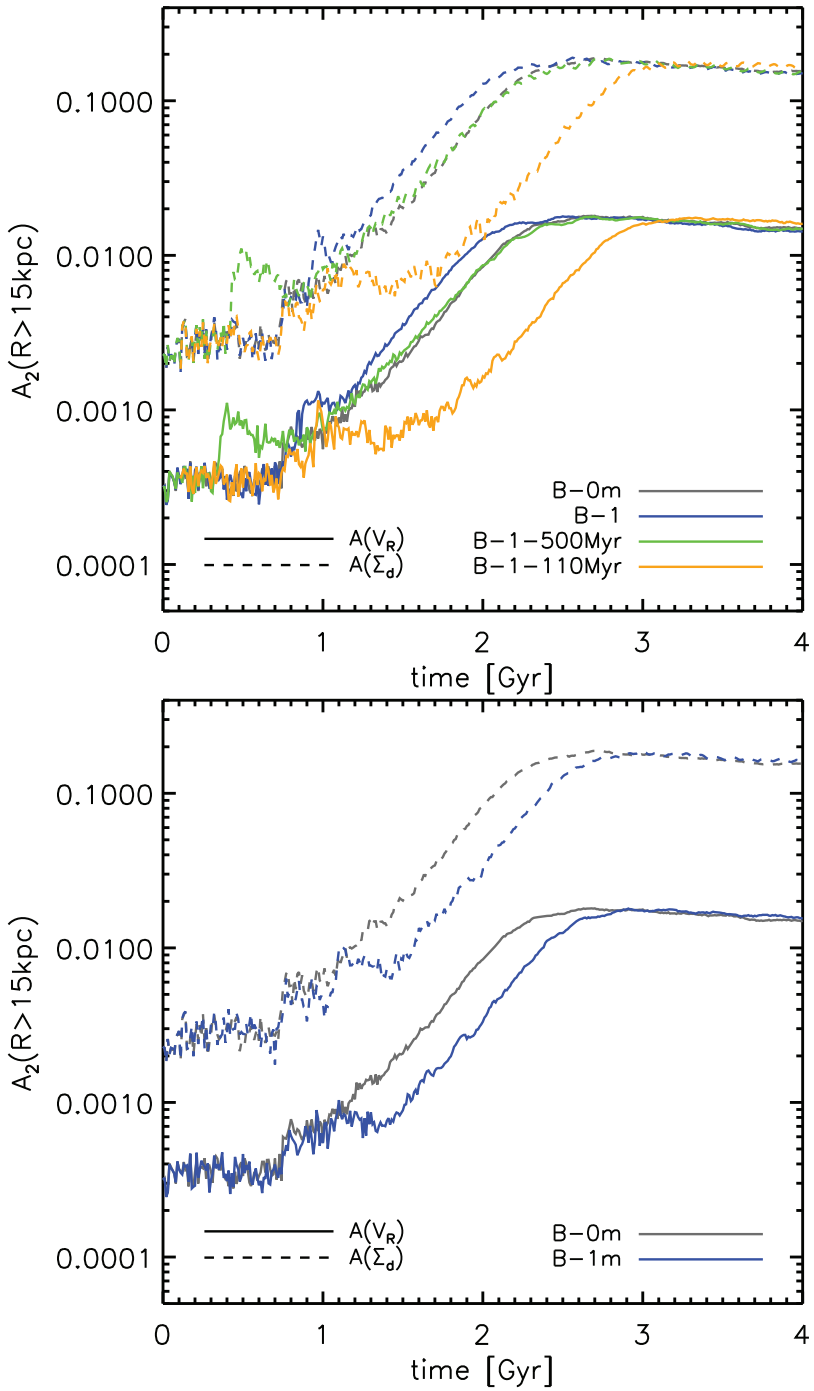

Figure 4.4.5: The evolution of m [3 mode's amplitude, calculated using the surface density (dashed) and radial velocity (solid), of the disc particles. Top panel corresponds to the fully–rescaled runs, while the mass–rescaled B-1m run is shown in the bottom panel.

starts around 0.7–0.8 Gyr which is after the crossing in B-1-500Myr. As the satellite approaches the inner 3–4 kpc, it generates a density wave which could in principle interact with any instability mode residing in the region. In the case of B-1, the satellite induced perturbation amplifies the bar mode which advances quicker than what is observed for the isolated system (B-0m). However, the perturbation in B-1-500Myr run does not interact with the bar mode, since at 0.5 Gyr the bar instability is still sub–dominant and this perturbation passes by without any interaction. The period $T_1 < t < T_2$ is the most critical, as bar–like perturbations with amplitudes greater than 0.01 are prone to incoming satellites. Once the bar mode is induced, it grows at similar time as B-0m (Fig. 4.4.5). The 2–armed mode in the outer disc winds up faster in B-1-500Myr.

4.5 Separate harmonics in N-body simulation

A Fourier analysis of surface densities provides a deeper understanding of the disc evolution. We define two types of amplitudes, describing m–armed structures in radial space

$$A_R)R, t+[\quad \frac{2}{M_{\rm d}} \sum_j m_j {\rm e}^{-im\theta_j} \ , \tag{4.15}$$

where the summation is performed over disc particles within a ring near radius R. In 'spirality' space

$$A_p)p, t+[\quad \frac{2}{M_{\rm d}} \sum_j m_j {\rm e}^{-i(m\theta_j + p \ln r_j)} \ , \tag{4.16}$$

where the summation is over all disc particles. The 'spirality' is represented as p, and is related to the so–called pitch angle ι via er w [p/m. Hence, large positive values of p resemble tightly wound trailing spirals, while small p correspond to open spirals and bars. Maximum values of A_p at given time t render shapes of dominating logarithmic spirals in the forming structure. The profiles of the function $G)t+$defined by

$$G)t+[\quad {\rm n} \underset{p}{\rm c}\tilde{} \ {\rm m} \ A_p)p, t+ \tag{4.17}$$

for all runs listed in Tab. 4.3.2 are very similar to the $B)t+$profiles presented in Fig. 4.4.4. In particular, they also consist of oscillatory, growth, and a plateau

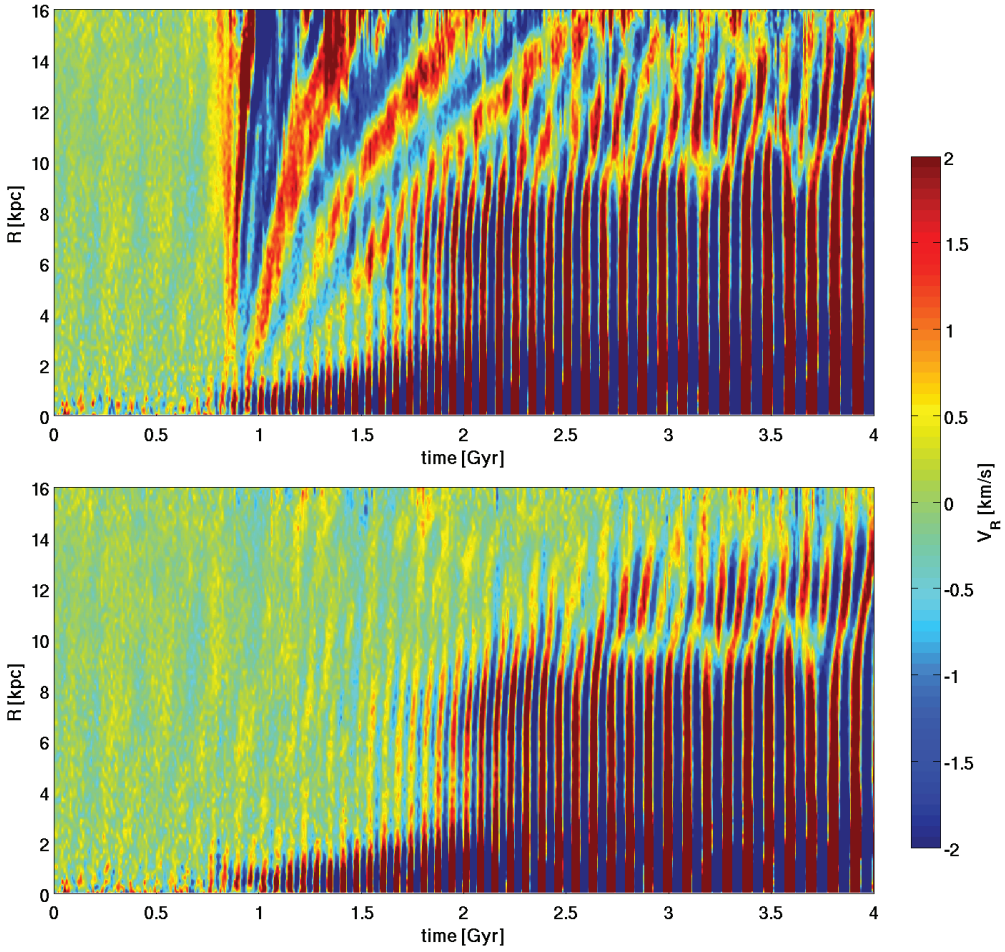

Figure 4.4.6: Surface plot of $V_R)R, t+$real component for m [3 harmonics, in the case of B-1 (top) and B-0m (bottom) runs across the disc's radial range.

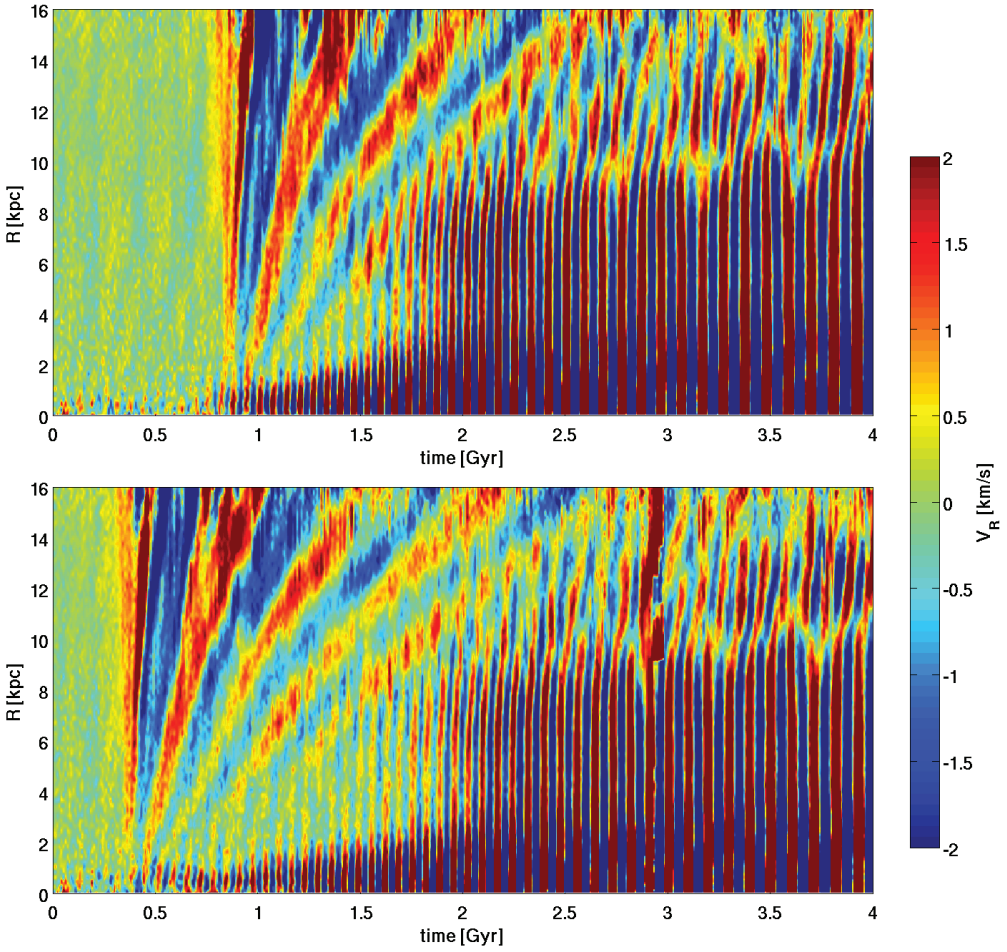

Figure 4.4.7: Surface plot of $V_R)R, t+$real component for m [3 harmonics, in the case of B-1 (top) and B-1-500Myr (bottom) runs across the disc's radial range.

phase of saturated instability.

Further, we introduce the time Fourier transformation (TFT) of the amplitudes A_p and A_R

$$S_R)R, \bar{}_p, T+[\int_{T-\Delta T}^{T+\Delta T} A_R)R, t+H)t \quad T+e^{im\Omega_p t} , \tag{4.18}$$

and

$$S_p)p, \bar{}_p, T+[\int_{T-\Delta T}^{T+\Delta T} A_p)p, t+H)t \quad T+e^{im\Omega_p t} . \tag{4.19}$$

In both expressions H denotes a window function, e.g. Gaussian or Hann filter adopted here. The window function is responsible for selecting a subset of our sample to perform the Fourier transform. TFT produces spectral maps

$$M_p)p, \bar{}_p, T+[\ln \frac{S_p{}^2}{3\pi} , \quad M_R)R, \bar{}_p, T+[\ln \frac{S_R{}^2}{3\pi} \tag{4.20}$$

indicating locations of coherent structures in $)p, \bar{}_p)$- and $)R, \bar{}_p)$-planes.

Figs. 4.5.1 and 4.5.2 show the spectral maps of M_R (right) and M_p (left) of $m [3$ mode for B-1 and B-1-500Myr runs, respectively. The top panel corresponds to $t [1.=$Gyr, while the bottom panel captures $t [2.56$ Gyr. The time window employed in these calculations is $\Lambda t [1.5$ Gyr. The y-axis corresponds to the normalised pattern speed $\bar{}_p$ of instabilities, with unit of 100 kms^{-1}. The contour levels, ranging from 1 to 100%, are evenly spaced in logarithmic space. Also, the solid pink curves show the profile of circular velocity $\bar{})R+$, together with the inner and outer Lindblad resonances, $\bar{})R+\equiv \kappa/3$. The dotted lines represent $\bar{})R+\equiv \kappa/5$. The red crosses mark the instabilities with maximum values. Less than 0.1 Gyr after the impact, in addition to the forming bar mode with $p/m [3$ in the inner part, we observe a significant 2–armed perturbation that dominates at $R > 6$ kpc for B-1. It takes about 0.55 Gyr for this mode to become tightly wound ($p/m [7$) and disappear, whilst the bar mode becomes dominant. For B-1-500Myr, the 2–armed mode has winded up into a trailing arm by 0.9 Gyr. This perturbation is confined between the ILR and the corotation resonance(CR). During the exponential growth period, the bar becomes longer and stretches to $R [9$ kpc. However, the slow–down phase causes the pattern speed to decrease.

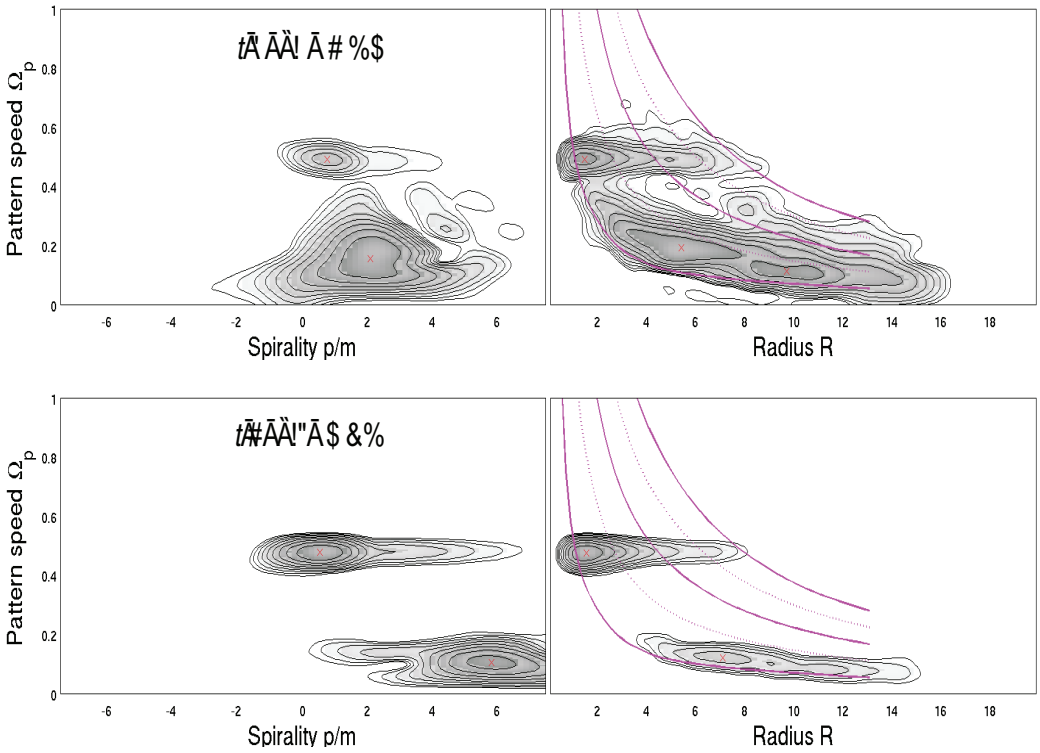

Figure 4.5.1: Spectral maps of M_R (right) and M_p (left) of m [3 mode for B-1 run, corresponding to t [1.=Gyr (top) and t [2.56 Gyr (bottom) with the time window Λt [1.5 Gyr. The y-axis corresponds to the normalised pattern speed of instabilities. The contour levels range from 1 to 100%, evenly spaced in logarithmic scale. Also, the solid pink curves show the profile of circular velocity $^{-})R+_{\mp}$ together with the inner and outer Lindblad resonances, $^{-})R+\equiv \kappa/3$. The dotted lines represent $^{-})R+\equiv \kappa/5$. The red crosses mark the instabilities with maximum values.

By the end of the simulation, the bar extends to only $R \approx 6$ kpc.

4.5.1 Lopsided mode m=1

The existence of lopsided asymmetries is observed in external spiral galaxies (e.g. Zaritsky and Rix 1997; Bournaud et al. 2005). It has been shown theoretically that interaction with accompanying galaxies could result in this phenomena (Kazantzidis et al., 2009). The m [2 mode allows us to measure any off-centred deviations, since this mode is usually the most prone to asymmetrical perturbations.

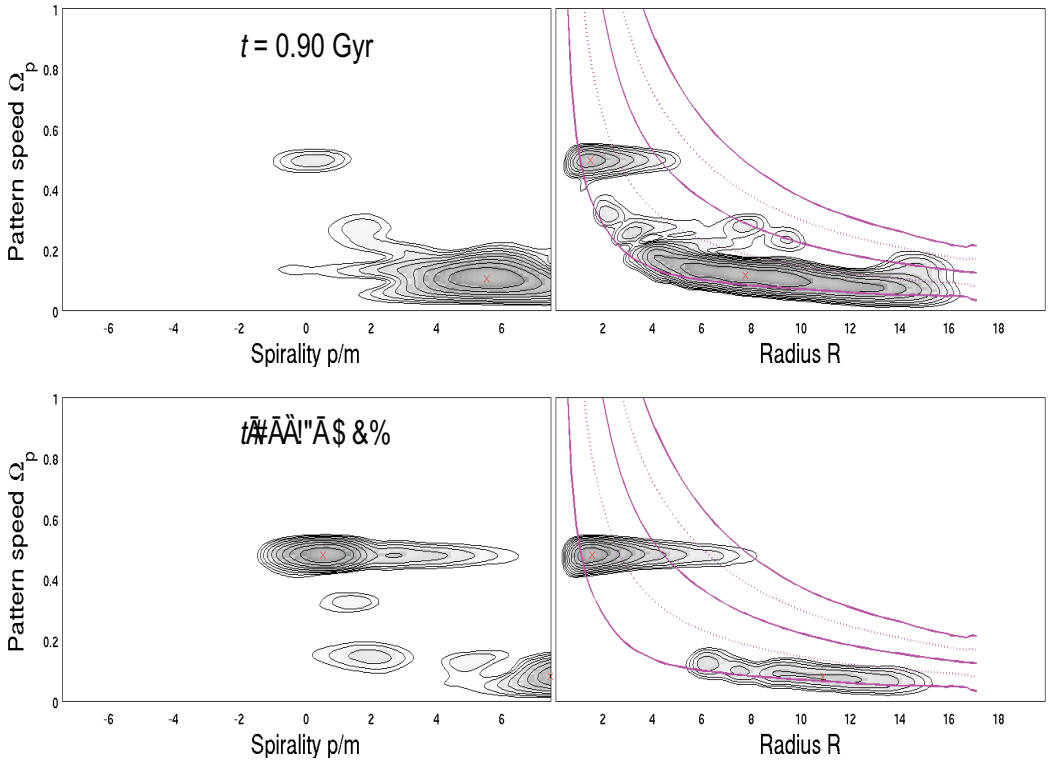

Figure 4.5.2: Spectral maps of M_R (right) and M_p (left) of m [3 mode for B-1-500Myr-delay run, corresponding to t [1.=Gyr (top) and t [2.56 Gyr (bottom) with the time window Λt [1.5 Gyr. The y-axis corresponds to the normalised pattern speed of instabilities. The contour levels range from 1 to 100%, evenly spaced in logarithmic scale. Also, the solid pink curves show the profile of circular velocity $^{-})R+_{\mp}$ together with the inner and outer Lindblad resonances, $^{-})R+\equiv \kappa/3$. The dotted lines represent $^{-})R+\equiv \kappa/5$. The red crosses mark the instabilities with maximum values.

The time evolution of m [2 mode amplitude is shown in Fig. 4.5.3 for all the fully-rescaled B-1 runs (top) and mass–rescaled B-1m (bottom). The amplitudes are calculated according to Eq. 4.11, taking into account disc particles across the whole disc. The impact of the satellites is clearly visible, taking the form of sudden jumps in the amplitude for all runs with satellite. The isolated B-0m system possesses a slow growth of the amplitude, reaching $\approx 150\%$ of the initial value after 4 Gyr. In the case of simulations with satellites, the increased amplitude stays relatively constant for $\approx$1 Gyr after the impact. We then observe the decline of $A_{\tilde{\Sigma}}$ with time, finishing with a similar amplitude as B-0m. The encounters correspond to a peak relative increase of $A_{\tilde{\Sigma}})t+/A_{\tilde{\Sigma}})1+\approx 7$.

Fig. 4.5.4 represents surface plot of $\Omega)R,t+$ (Eq. 4.8) for m [2 mode, in the case of B-1 (top) and B-0m (bottom) runs. The passage of infalling satellite results in excitation of the m [2 mode, which is more prominent in the outer disc. The excited perturbation lives for $\approx$1 Gyr at $R > 23$ kpc, since it is easier to displace the disc particles in the outer parts due to the less stronger gravitational potential of the disc. We see evidence of additional m [2 modes during this period at $5 < R < 21$ kpc, which is also present in the isolated disc, however, with ≈ 4 times weaker amplitude. As concluded from Fig. 4.5.3, this excited mode winds up quickly and disappears.

For a satellite to influence the bar-formation, the time of crossing is crucial. If the incoming perturbation due to the satellite enters during the shot noise regime, the bar mode is not affected. In case the perturbation is induced amid $T_1 < t < T_2$, a delay or advancement of the bar mode is observed. The asymmetric m [2 mode shows a clear indication of the impact with an increase of the amplitude by a factor of 5. However this mode decays towards the end of the simulation; once, the m [3 becomes dominant.

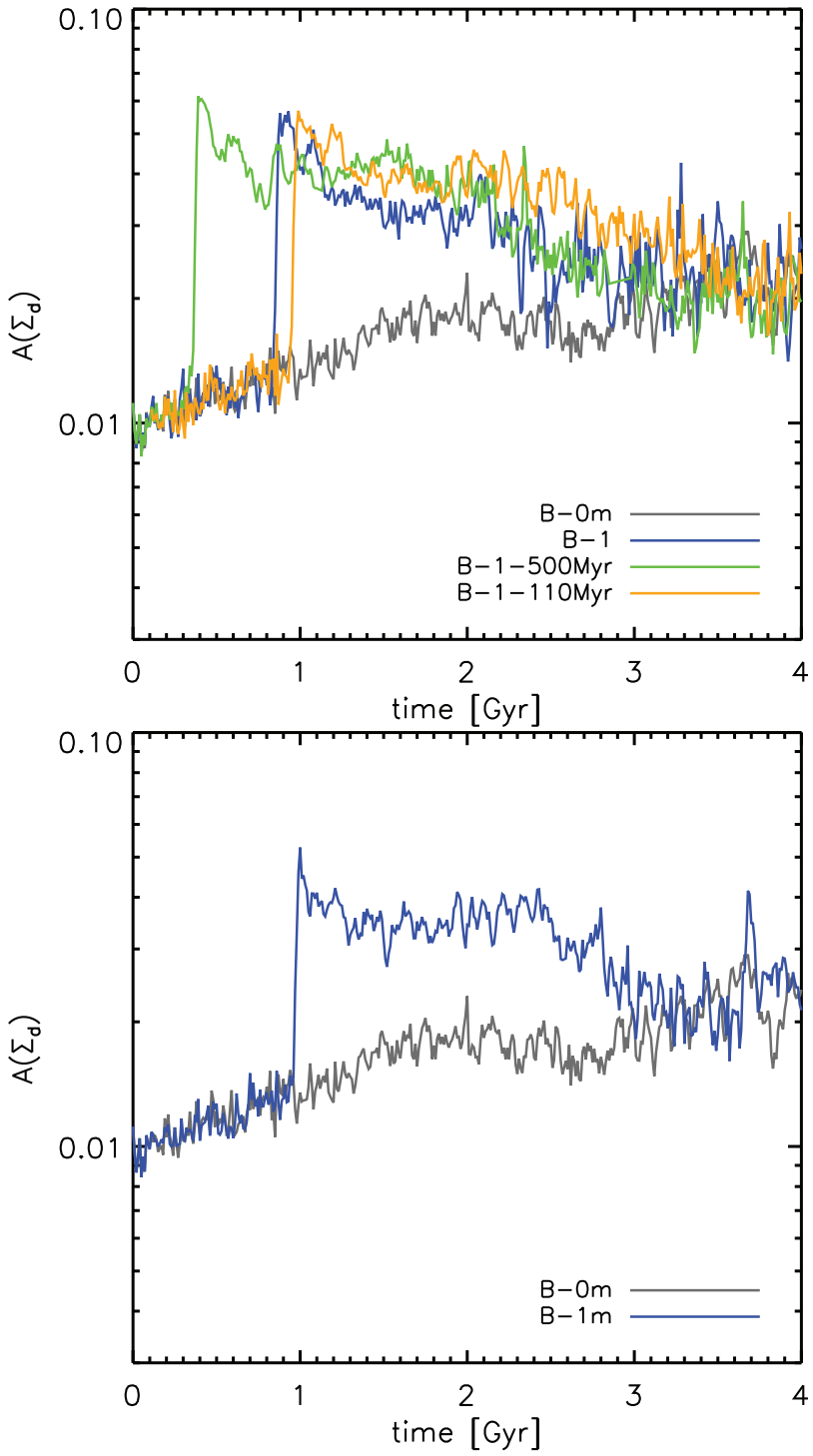

Figure 4.5.3: Time evolution of m [2 mode amplitude calculated using the Fourier transform of the disc surface density for fully–rescaled (top) and mass–rescaled (bottom) runs.

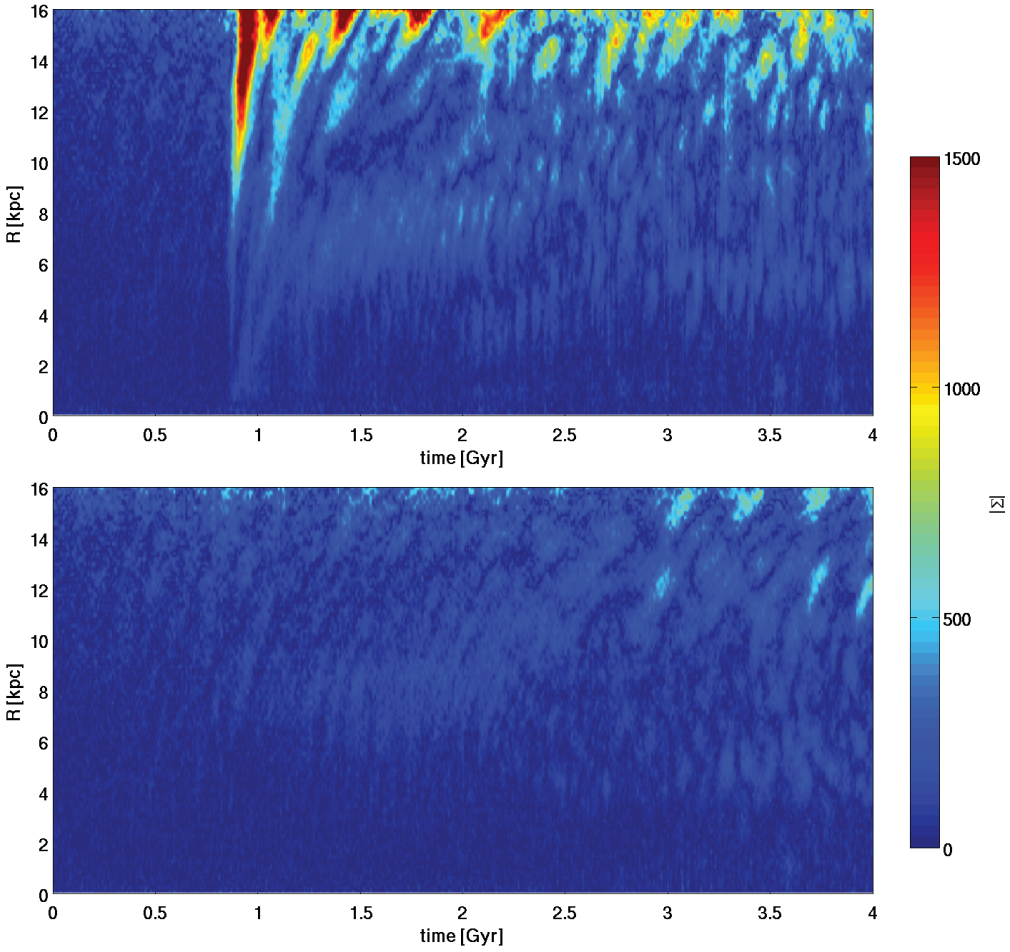

Figure 4.5.4: Surface plot of $\Omega)R, t+$ amplitude for m $[$ 2 harmonics, in the case of B-1 (top) and B-0m (bottom) runs across the disc's radial range.

"I know you're tired but come, this is the way."

- Jalaluddin Rumi

5 Localisation of the heating

As concluded in section 3.4, the contribution of infalling satellites towards the observed vertical heating of the Galactic disc is small, especially in the solar neighbourhood region, where it only reaches 3-10% of the observed heating rate with a significance of more than 3σ. The Aq-F2 simulation possesses the largest impact on the disc heating, having the most massive perturber among all 7 simulations. The measured heatings from the previous chapter are calculated radially along the disc plane. Within the scheme of this chapter, we explore the *localised* heating of the disc.

5.1 The simulation

According to the results of chapter 3, the mass of the infalling satellites are the major factor, determining the extent of the heating. The most massive satellite between the 131 candidates (Tab. 2.2.1) belongs to the Aq-F2 run with $M_{\rm tid}$ [$6.=\pm 21^{10} M_{\odot}$. The Aq-F2 simulation was initially carried out in isolation, for a period of 2 Gyr. At this point, we add the subhalo and let both simulations run for an additional 4 Gyr. This corresponds to a total of 6 Gyr, in contrast to

the runs in the previous chapter which lasted 4 Gyr in total. This allows for three pericentric passages. The initial conditions are the same as in the previous chapter.

Since the presence of such a massive perturber could significantly disturb the disc, we are required to correct for any tilting or movement of the disc with respect to the reference coordinate frame. The correction is performed at every time–step, following the procedure mentioned in section 3.3.2. Hereafter, the simulation with satellite is referred to as Aq-F2-1e10. Fig. 5.1.1 displays the time evolution of the satellite's spherical distance r from the disc's centre of density (solid blue). In addition, the dotted red line corresponds to the fraction of satellite's bound mass, $M)t+/M)1+$ The bound mass refers to the fraction of the total mass with higher potential energy than kinetic energy, relative to the satellite's centre of density. The first pericentric passage occurs at $\approx$ 0.5 Gyr, coming as close as r [13 kpc. At this point, we also observe a significant mass loss of $\approx$ 50% by the satellite. This originates from the tidal forces which act on the satellite as they moves through the DM host halo. As the object loses mass, its pericentre distance $r_{\rm p}$ gets smaller. The last $r_{\rm p}$ has a value of $\approx$ 7.6 kpc, close to the solar neighbourhood. By the end of the simulation, only less than 10% of bound mass is remained. The slight increase of bound mass, observed as peaks in $M)t+/M)1+$ arise due to the decrease of kinetic energy at the apocentre – furthest orbital distance.

Fig. 5.1.2 shows the projected number density profile of the disc particles of Aq-F2-1e10 along x-y, x-z and y-z planes, at 1 (left) and 4 Gyr (right); the colour coding has a logarithmic scaling. The signature of the impact is clearly visible in the disc. The outer parts of the disc are perturbed, while the inner regions show a temporary spiral structure, disappearing after few rotations. The disc experiences major tilting, which is visible in x-z and y-z planes at 4 Gyr. As it will be discussed in the following section, a significant thickening of the disc is seen. The face–down projected number density maps of the disc particles are presented in Fig. 5.1.3. The panels are outputted at every 0.5 Gyr. The outer disc is most vulnerable to the infalling satellite's impact. After the first pericentric encounter at 0.5 Gyr, the disturbance travels inwards through the disc.

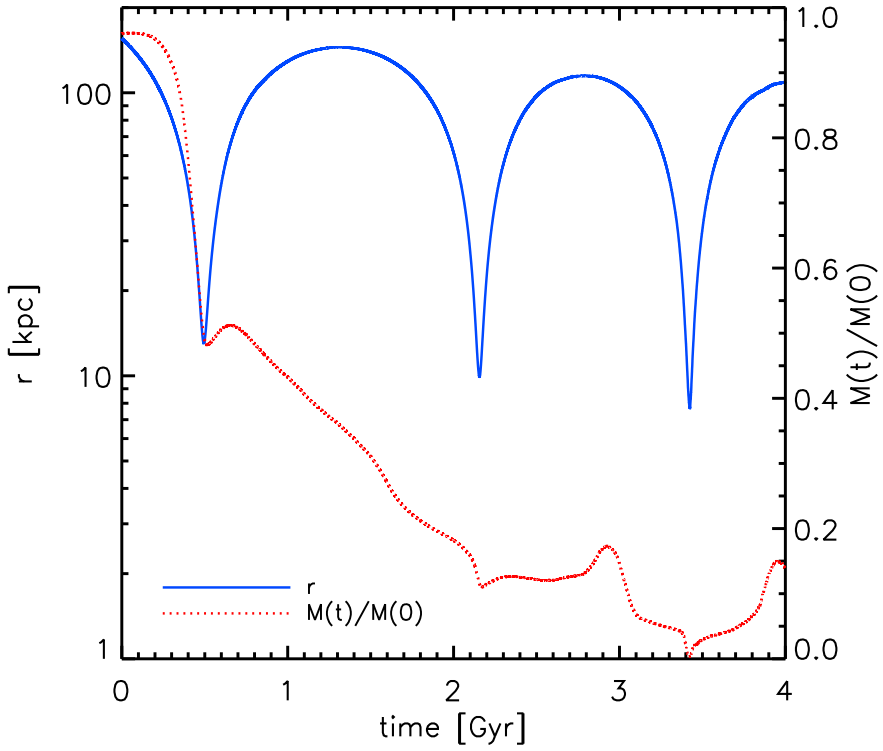

Figure 5.1.1: The spherical distance r of the satellite from the disc, as a function of simulation time (blue). Also, the fraction of satellite's bound mass is shown using dotted red line.

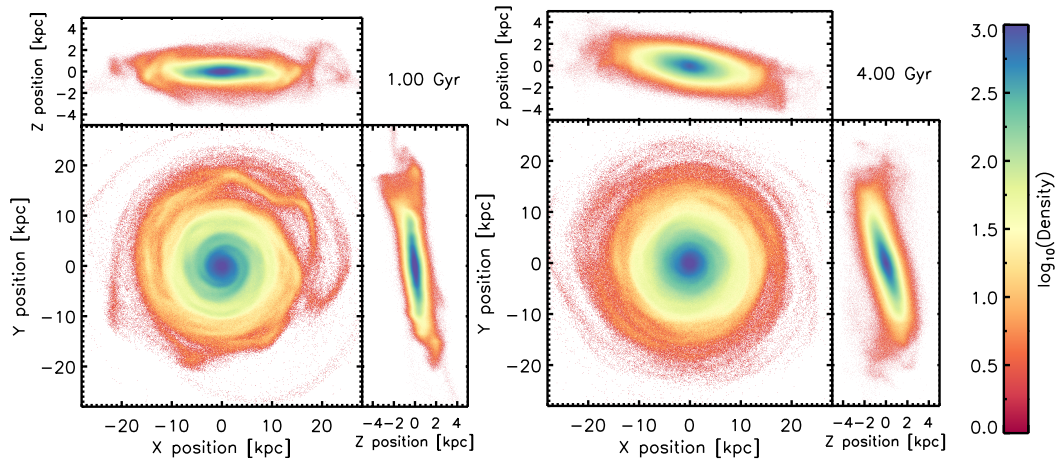

Figure 5.1.2: The number density plots for the Aq-F2-1e10 in x-y, x-z and y-z planes at time 1 (left) and 4 Gyr (right). Logarithmic colour scaling is employed.

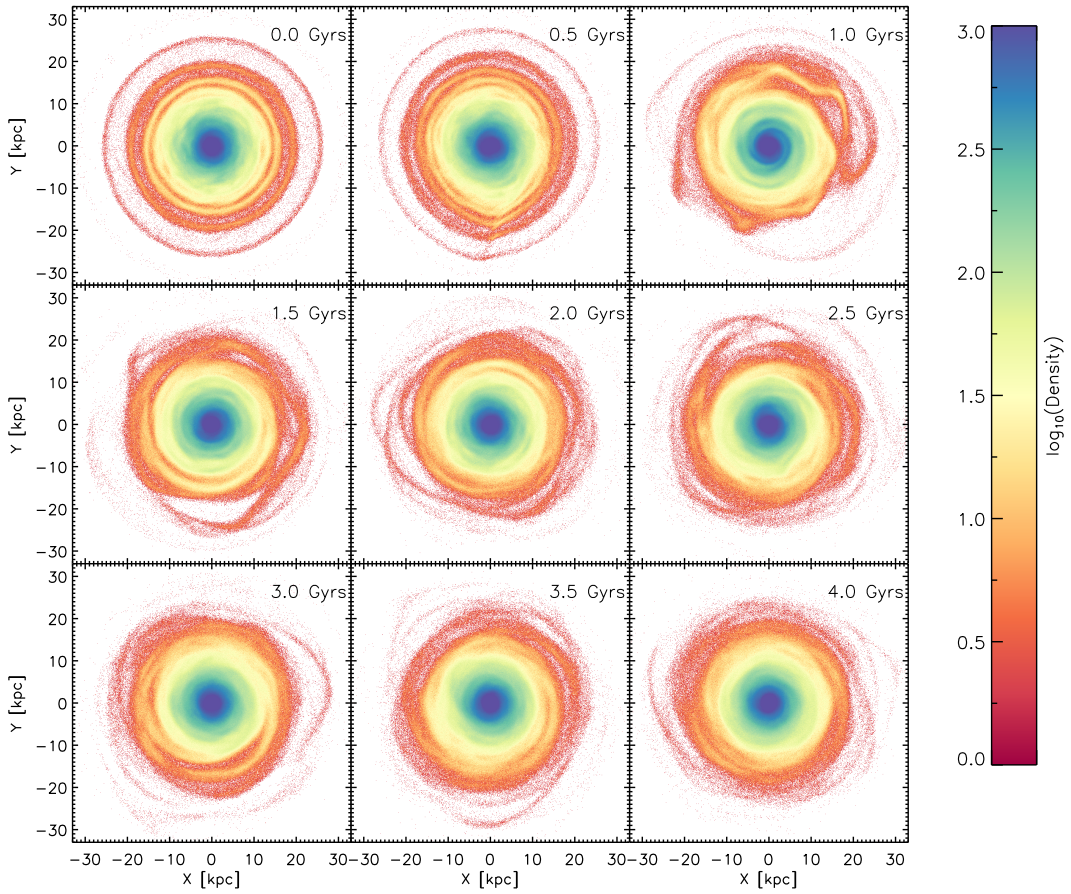

Figure 5.1.3: The projected number density plots for the Aq-F2-1e10 in x-y plane with logarithmic colour scaling. The simulation time is shown in the top–right side of each panel.

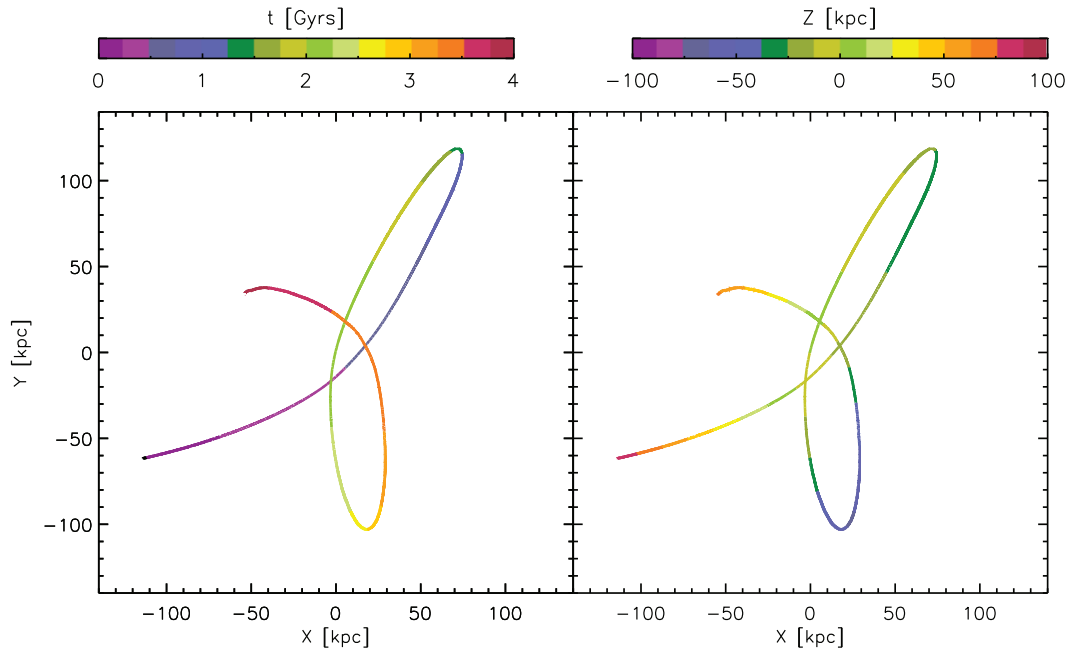

Figure 5.2.1: The top–down view of the Aq-F2-1e10 satellite's orbit. *right:* The colour coding represents the z coordinate of the satellite. *left:* The orbital time is shown using the colour code.

5.2 Vertical heating

In this section, we quantify the heating of the Galactic disc due to an infalling satellite. In order to visualise the satellite's orbit, the face–down view of the orbit is shown in Fig. 5.2.1. The colour coding of the right panel corresponds to the z–coordinate of the satellite, with the positive values for above the disc plane. For the left panel, the orbital time is colour coded. Initially, the object starts from $)x, y, z+[\ \ )$-115, -63, 100) kpc. During the first pericentric passage, the subhalo is located at $)x, y, z+[\ \ )$4.6, -9.5, -7.7) kpc.

Prior to the actual heating measurements, it is useful to investigate the mean behaviour of the disc. Fig. 5.2.2 displays the projected surface plot of the mean vertical velocity μ_{v_z} [$< v_z >$ of the disc at 1, 2, 3 and 4 Gyr, starting from the top left, for Aq-F2-1e10. It is worthwhile to mention, the isolated system shows no significant sign of average increase in v_z throughout the course of 4 Gyr, with maximum $< v_z > \ < 5$ kms^{-1}. The signature of the satellite's impact at $\approx$0.5 Gyr translates into the radial variation of $< v_z >$. Such distinct imprints are

only seen at $R > 10$ kpc. This quantity increases progressively towards the end of the simulation, reaching values as high as $\equiv 50$ kms^{-1}. After 3 Gyr, we notice a distinction between two halves of the disc, with one half possessing positive $< v_z >$, whilst the other half with mostly negative values. It is relevant to note, such values have already taken into account the correction for the disc's centre of density movement and tilting.

Fig. 5.2.3 shows the projected surface plot of the median z–coordinate normalised by radial distance, $z_{\rm median}/R$, of the disc for Aq-F2-1e10, at four different simulation times (1,2,3 and 4 Gyr). We chose the median over the mean, in order to reduce the contribution of few particles with extreme z values. Also, the normalisation with R is aimed to intensify the traces of impact in the inner regions of the disc. Once again, the isolated Aq-F2 run shows no sign of notable vertical motion. During the initial 2 Gyr at certain parts of the disc, we observe a radial transition between disc particles displaced above and below the plane. The contrast between positive and negative $z_{\rm median}/R$ at 4 Gyr, corresponds to the observed tilting of the disc (Fig. 5.1.2). This tilting reaches $z_{\rm median} \approx 5$ kpc at $R > 20$ kpc, which is significant ($\approx 4\,h$). The particles' reaction to the impact is more prompt in the vertical velocity space, compared to their positional z space. Comparing the bimodal behaviour of the disc at t [5 Gyr in Fig.5.2.2 and 5.2.3, it takes 1/4 of disc rotation for disc particles with increased/reduced $z_{\rm median}$ to get physically displaced, considering the rotation is anti–clockwise if viewed from above the plane.

The radial dependence of the median z–coordinate, $z_{\rm median}$, for the isolated (dashed) and with satellite (solid) simulations are shown in Fig. 5.2.4. Different colours represent simulation time for 0–4 Gyr. The disc is divided into 8 azimuthal slices, each with a size $\Lambda\,\phi$ [56°, ranging from -180° $< \phi <$ 180° (eq. 2.12). The range [0°, 90°) corresponds to the particles with positive x and y coordinates; while, particles with positive x and negative y lie within [-90°, 0°). The isolated system possesses an isotropic behaviour across the disc, with $z_{\rm median}$ values fluctuating around 0 kpc. The median z reaches maximum of ≈ 4 kpc at 4 Gyr. Comparing the values across the octants, we observe evidences for *warping* in the outer parts. Such phenomena causes an integral–sign shaped disc, if viewed edge on, rising above the plane on one side and falling below on the other side. For instance, the

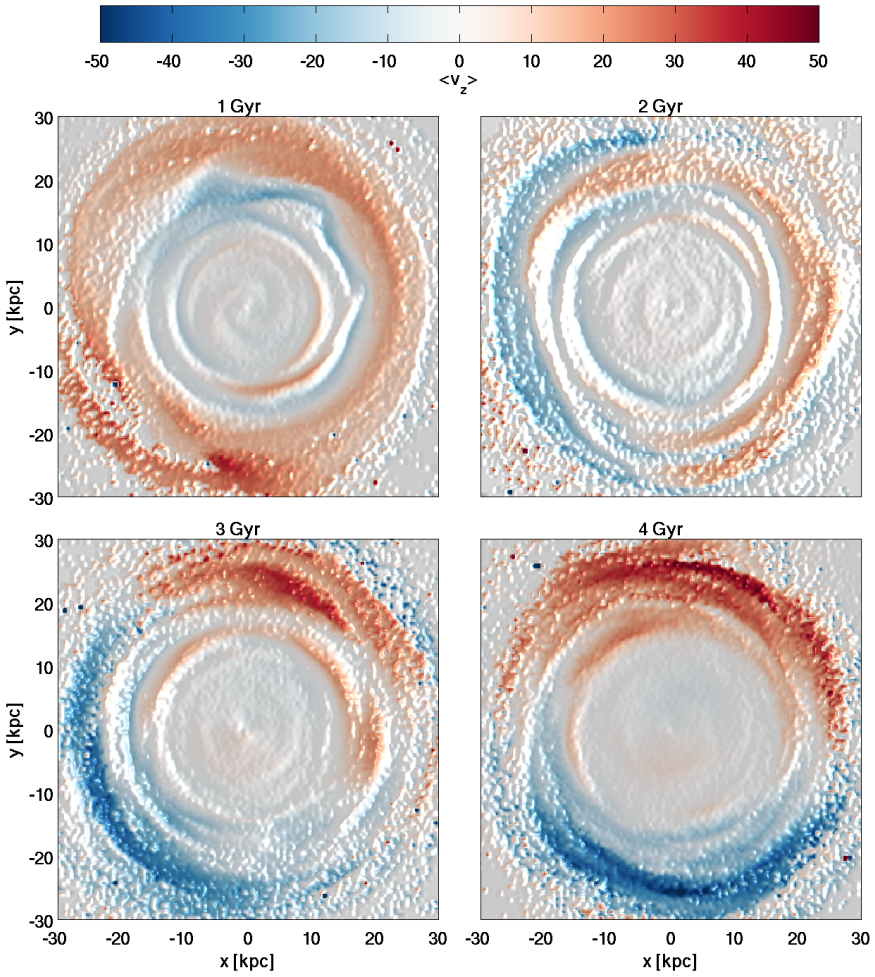

Figure 5.2.2: Projected surface plots of mean vertical velocity $< v_z >$, in kms^{-1}, of disc particles for Aq-F2-1e10. Starting from the top, the panels correspond to simulation times of 1, 2, 3 and 4 Gyr.

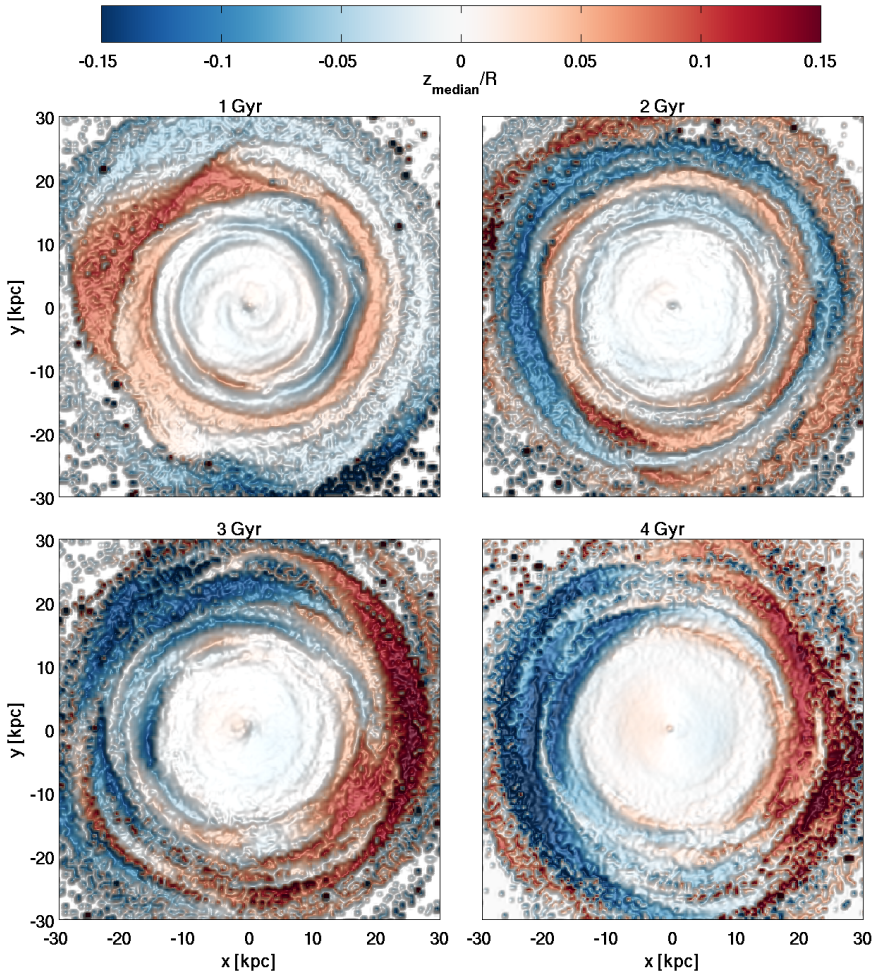

Figure 5.2.3: Projected surface plots of the median z–coordinate normalised by radial distance, $z_{\rm median}/R$, of disc particles for Aq-F2-1e10. Starting from the top, the panels correspond to simulation times of 1, 2, 3 and 4 Gyr.

[90°, 135°) and it's counter octant, [-90°, -45°), show similar $z_{\rm median}$ values but with opposite signs. Warps are also observed in external spiral galaxies, subject to interactions. Our results support the theory of Sagittarius dwarf galaxy being responsible for the Milky Way disc's warp (e.g. Reed 1996; Evans et al. 1998; Bailin 2003; Gómez et al. 2016a).

In recent years, a ring–like feature in the outer parts of the Galactic disc, known as Monoceros ring, has been subject of discussion. First discovered in the Sloan Digital Sky Survey (SDSS), this ring corresponds to one of the four peaks observed as part of a radially oscillatory behaviour in the midplane with radial range 10 $< R <$ 21 kpc (Newberg et al. 2002; Belokurov et al. 2006; Xu et al. 2015). It is believed to be located at $R \approx 16$ kpc. The vertical amplitude of these oscillations increases radially and reaches z values of 3 kpc. According to our simulation, we observe similar oscillatory pattern in the outer disc, caused by the presence of the satellite. The peaks at ≈ 15-16 kpc reach a vertical median height of 2-3 kpc, as observed for the Monoceros ring. Therefore, we can support the contribution of an infalling satellite towards formation of such features.

As previously discussed in chapter 3, in order to quantify the vertical heating of the Galactic disc, we take advantage of two quantities: $z_{\rm rms}$ (eq. 3.7) and σ_z^2, which represent the root-mean-square of disc thickness and the vertical velocity dispersion of the disc, respectively. Fig. 5.2.5 shows the time evolution of $\sigma_{z,t}^2 \quad \sigma_{z,0}^2$ for the disc particles, lying initially within 4 kpc of the first pericentre distance; $\sigma_{z,0}^2$ being the squared vertical velocity dispersion at t [1, when we add the satellite. The run with satellite is displayed as blue, while red corresponds to the isolated simulation. The colour scheme represents the average radial distance of the particles from the centre. Also, the moments of pericentric passages are marked with arrows. For Aq-F2-1e10 run, the first pericentre crossing causes a sudden significant jump in vertical velocity dispersion, reaching $\sigma_{z,t}^2 \quad \sigma_{z,0}^2 \approx 266$ km^{2}s^{-2}. However, these particles cool down dynamically via transfer of the vertical energy within a course of 0.4 Gyr, which roughly translates into the duration of one complete disc rotation at R [24 kpc. The impact displaces the particles and moves them as close as 7.5 kpc to the centre, although they shift back closer to their original position later on. Even in the absence of the satellite, the isolated disc retains a steadily rising vertical heating with ≈ 11.5 km^{2}s^{-2}Gyr^{-1}. This

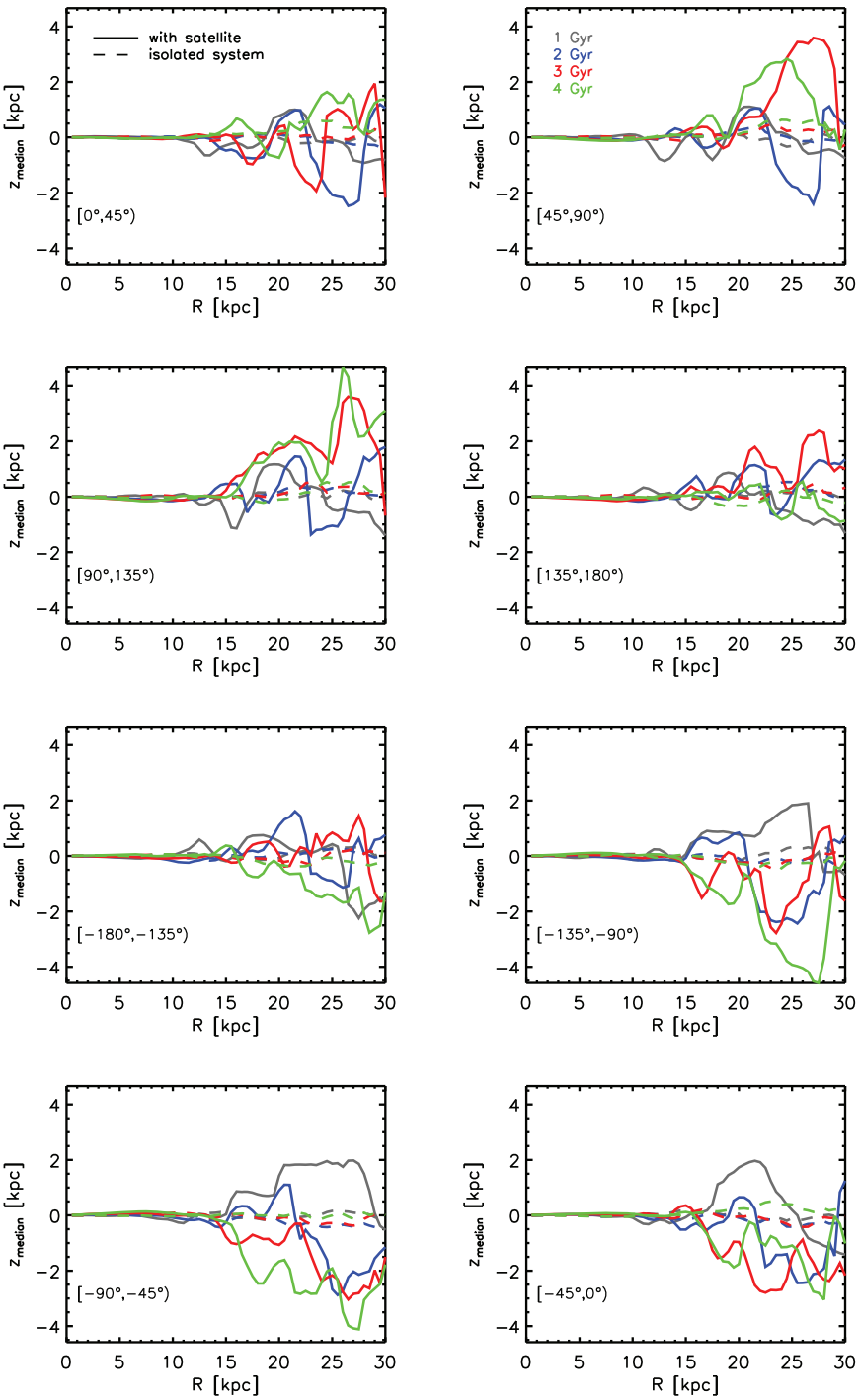

Figure 5.2.4: The radial dependence of $z_{\rm median}$ for the isolated (dashed) and with satellite (solid) simulations. Different colours correspond to t [0 to 4 Gyr. Also, the disc is divided into 8 octants according to the particles azimuthal angle ϕ with a range -180° $< \phi <$ 180°.

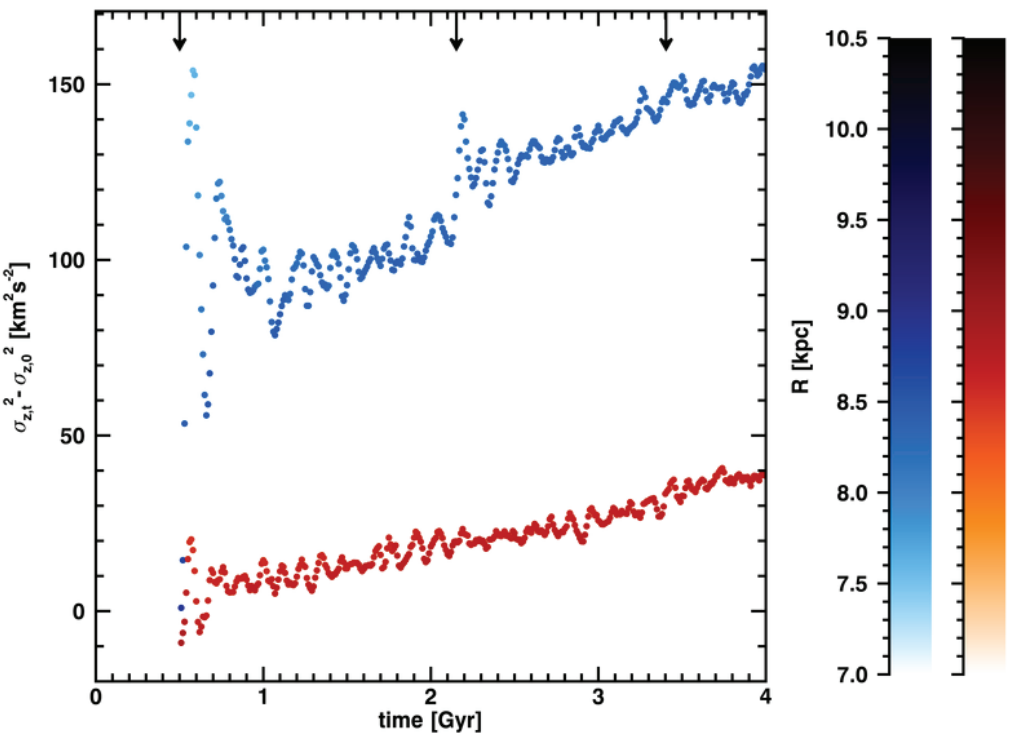

Figure 5.2.5: $\sigma^2_{z,t}$ $\sigma^2_{z,0}$ evolution with time for the particles lying initially within 4 kpc of the first pericentre, for the system with satellite (blue) and isolated (red). The colour bar represents the average radial distance of the particles from the centre. The pericentre passage times are marked with arrows.

supports the rational that secular evolution of spiral discs, results in heating of stars which are born dynamically cold. The magnitude of the impact from second and third pericentre passages decreases due to less bound mass residing within the satellite (≈12%), and the fact that it is more difficult to increase the velocity of hotter stars. The infalling satellite increases the vertical velocity dispersion of these stars by 110 km^{2}s^{-2}, compared to the isolated case, at the end of simulation.

The radial dependence of $z_{\rm rms,t}$ $z_{\rm rms,0}$ (top) and $\sigma^2_{z,t}$ $\sigma^2_{z,0}$ (bottom) is shown in Fig. 5.2.6 for system with satellite (solid) and isolated (dotted) runs. In the bottom panel, the filled diamond represents the observed vertical heating value of 288 km^{2}s^{-2} in the solar neighbourhood at t [5 Gyr (Holmberg et al., 2009); while, the empty diamond shows this value, taking into account a 0.5 Gyr delay. In the case of $z_{\rm rms}$, the isolated disc shows a steady constant profile throughout

the simulation, with a maximum thickening of 0.1 kpc in the outer part compared to t [1 Gyr. The most significant increase occurs after the first impact (1 Gyr) and we observe a thickening by 110% relative to the isolated disc at 15 kpc. The satellite's infall leads to a flaring in the outer disc regions (D'Onghia et al., 2016), reaching $\approx$ 1.9 kpc (180%) at 4 Gyr. For the vertical velocity dispersion, σ_z^2, both the isolated system and Aq-F2-1e10 have similar features, with a sharp decline within the inner 4 kpc and a flat distribution for $R > 5$ kpc. The sharp peak in the centre is mostly due to the presence of the bulge's potential. There exists a global vertical heating across the disc, in the absence of the satellite, with maximum of only $\approx$ 4% at R [22 kpc after 4 Gyr. The presence of the satellite fails at contributing enough energy to the vertical heating, in order to achieve the observed heating in the solar neighbourhood. The flat profile indicates a constant vertical heating, independent of the radius.

The projected surface plot of the quantity $\sigma^2_{z,t}$ $\sigma^2_{z,0}$ is displayed in Fig. 5.2.7 for our isolated (left) and Aq-F2-1e10 (right) runs, at four simulations epochs. The crossing results in vertical heating in the area of impact, which then spreads over the azimuthal range, due to the differential rotation of the disc. As the disc evolves, this energy transfers to the particles in the outer regions, since it requires less energy to increase their vertical velocity. The black annulus marks the position of the solar neighbourhood, $8.6 < R < 9.6$ kpc. The large value in the centre is common among both runs (also in Fig. 5.2.6). The significant heating in $R >$ 18 kpc is unable to reach the inner parts of the disc.

Fig. 5.2.8 shows radial dependence of vertical kinetic energy difference between time t and initial value per radial bin, $\Lambda\ \mathrm{kin}_z/\delta R$, for the isolated (dashed) and Aq-F2-1e10 (solid) simulations. This quantity is calculated according to eq. 5.1,

$$\frac{\Lambda\ \mathrm{kin}_z}{\delta R} [\quad \frac{\mathrm{kin}_{z,t} \quad \mathrm{kin}_{z,0}}{\delta R} [\quad \pi\,\Omega_{R,t}\,R\,)\sigma^2_{z,t} \quad \sigma^2_{z,0} \dotplus \tag{5.1}$$

The vertical heating is rather constant radially across the disc (Fig. 5.2.6). The $\Lambda\ \mathrm{kin}_z$ radial distribution reveals, less than $\approx$ 21% of the energy is deposited to the outer $R > 26$ kpc; although, possessing similar $\sigma^2_{z,t}$ $\sigma^2_{z,0}$. The presence of a bar–like feature for $R < 5$ kpc can, in principle, result in the sharp peak in $\Lambda\ \mathrm{kin}_z$. Therefore, this inner region should not be taken into account for the heating interpretations.

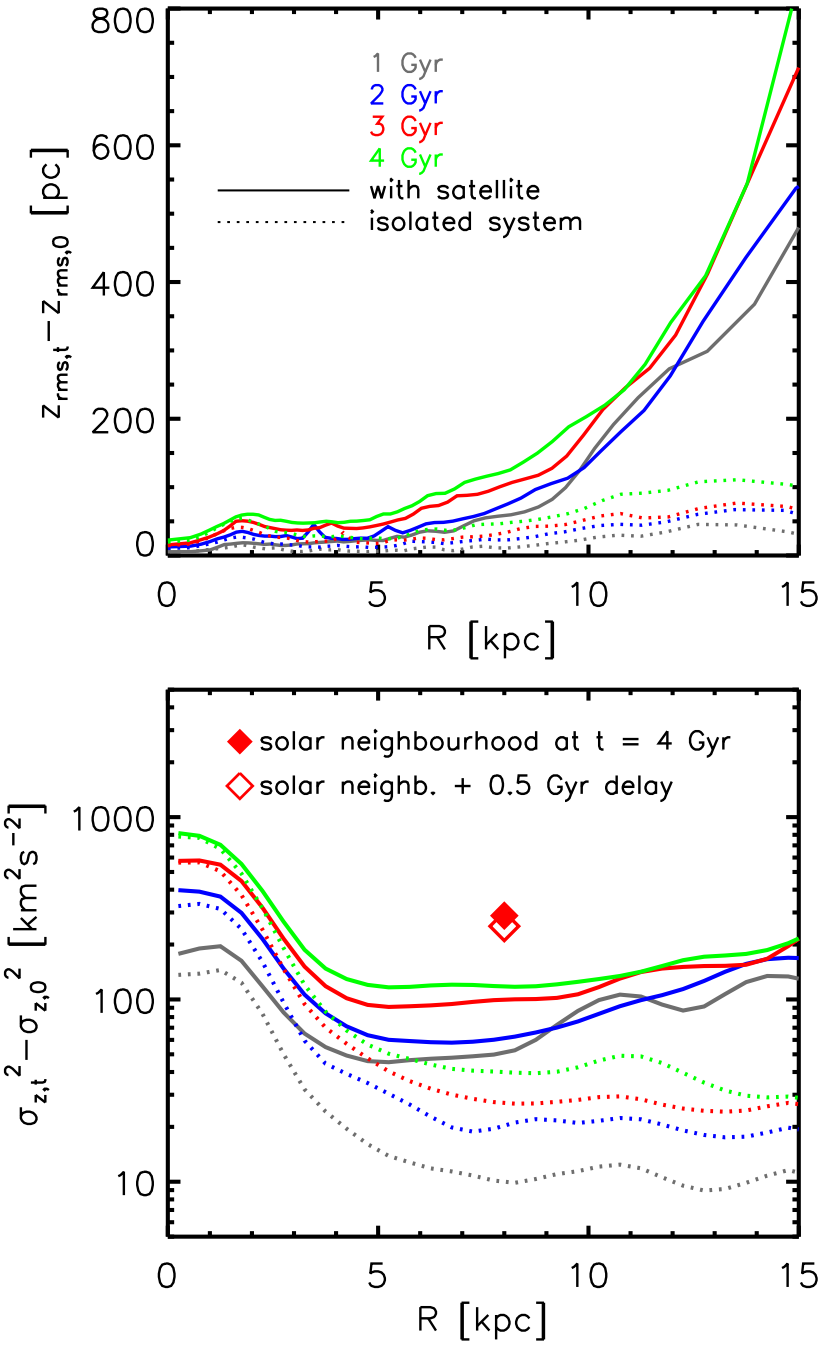

Figure 5.2.6: *Top:* Difference of root-mean-square of the disc height $z_{\rm rms}$ at t and 0 Gyr for systems with satellites (solid) and isolated (dashed) at 1, 2, 3 and 4 Gyr. *Bottom:* The difference of the disc vertical heating between t and 0 Gyr. Filled and open *diamonds* represent the observed value of vertical heating in the solar neighbourhood at 4 Gyr and the observed value with 0.5 Gyr delay.

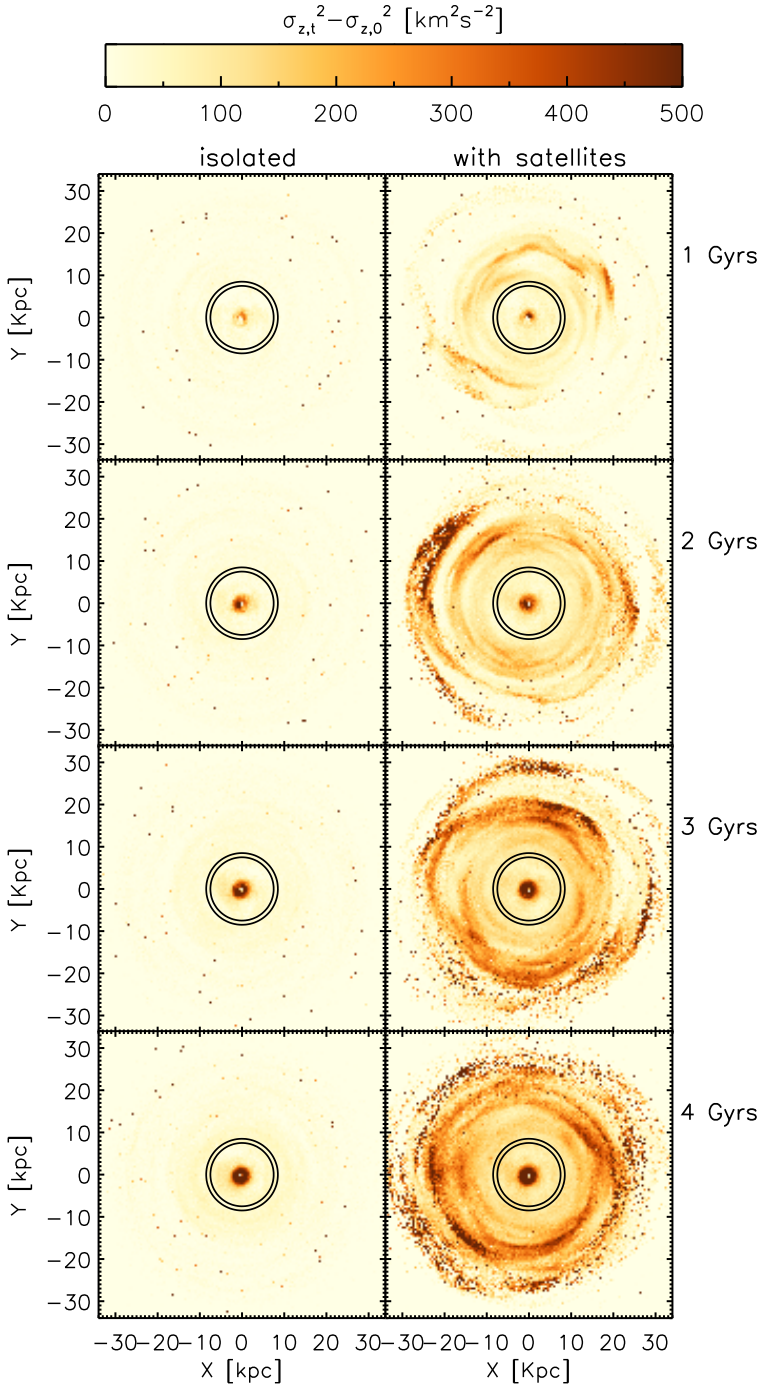

Figure 5.2.7: Projected surface plots of $\sigma^2_{z,t}$ $\sigma^2_{z,0}$ for disc particles in the case of the isolated (left) and with satellite (right) runs. Starting from the top, the panels correspond to simulation times of 1, 2, 3 and 4 Gyr. The annulus shows location of the solar neighbourhood, $8.6 < R < 9.6$ kpc.

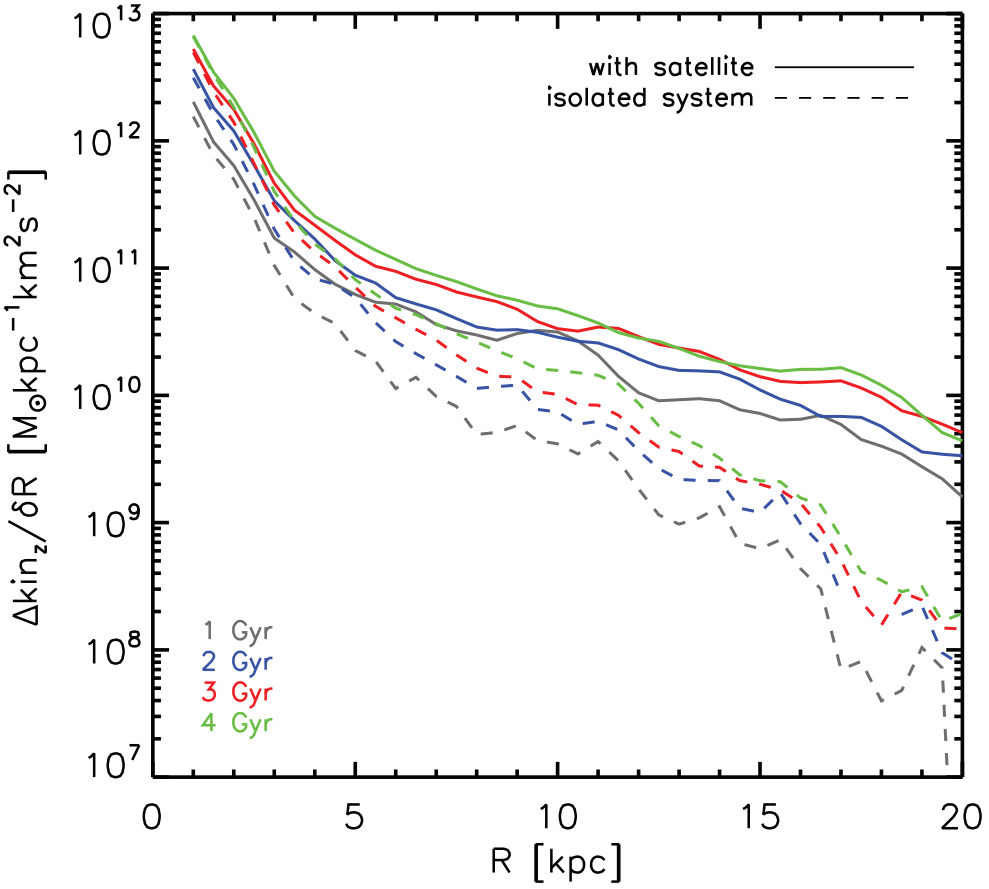

Figure 5.2.8: The radial dependence of vertical kinetic energy difference Λ kin_z between t and 0 Gyr,for isolated (dashed) and Aq-F2-1e10 (solid) runs. Different colours correspond to t [0 to 4 Gyr.

In comparison to the isolated run, the outer disc has a higher relative fraction of deposited vertical kinetic energy. After 1 Gyr, the energy profile stays steady and the evolution with time is insignificant. We determined the slope of the fitted line at 4 Gyr for $R > 5$ kpc and

$$\frac{\Lambda \text{ kin}_z}{\delta R} \; [\quad 7.87 \times 21^{11} \, 21^{\left(-\frac{R}{10 \text{ kpc}}\right)} \tag{5.2}$$

represents the line of best fit.

5.3 Instability

In addition to the heating, we would like to investigate the significance of the impact on mode excitation in the disc plane. We mostly focus on the contribution of such interactions, towards the process of bar formation, if any, and other unstable modes. The calculations performed in this section, follow the same recipe mentioned in chapter 4.

Fig. 5.3.1 represents the surface plots of the real component of Fourier radial velocity amplitude $V_R)R, t+$ in the case of m [3 mode, corresponding to the amplitude along the x-axis, calculated according to eq. 4.8 for the isolated (top) and Aq-F2-1e10 (bottom) runs. In case of the isolated disc, we observe weak imprints of the bar mode for $R < 5$ kpc, in the form of vertical blue/red strips. However, such oscillations are not strong and continuous. During the final 2 Gyr, there is a developing perturbation at $R \approx 15$ kpc, which winds up and slowly moves outward. Passage of the satellite, has a clear imprint via exciting m [3 density wave – blue vertical strip. Initially, this unstable mode has a relatively constant amplitude across the disc, within 0.1 Gyr of the impact. As the disc evolves, the perturbation takes the shape of a 2-armed spiral. During the process of winding up (the spiral arm's pitch angle gets smaller), the second impact occurs at t [3.2 Gyr. This creates a second generation of perturbation, superposed to already existing wave.

In order to more accurately quantify such modes, the following figures are aimed at exploring global modes via inspecting the time evolution of surface density $A_{\tilde{\Sigma}})t+$(red), radial (blue), vertical (gray) and tangential (green) velocity harmonics – $A_{\tilde{V}_R})t+$, $A_{\tilde{V}_z})t+$ and $A_{\tilde{V}_\phi})t+$ (eq. 4.11, 4.12, 4.13 and 4.14). The summation is done only over disc particles within the disc's scale radius h for Fig. 5.3.2, likely to contribute towards the bar; while, particles with $R > 15$ kpc are employed in the case of Fig. 5.3.3. For the inner disc, it appears that the impact does not generate any excited perturbation, since we only observe fluctuations around a mean value. There exists a slight rise in the vertical velocity amplitude (gray), which decays quickly after 0.5 Gyr. Once we perform this calculation for the outer disc, vertical velocity is the most prone to the impact. All the components experience an excitation due to the wave generated by the satellite

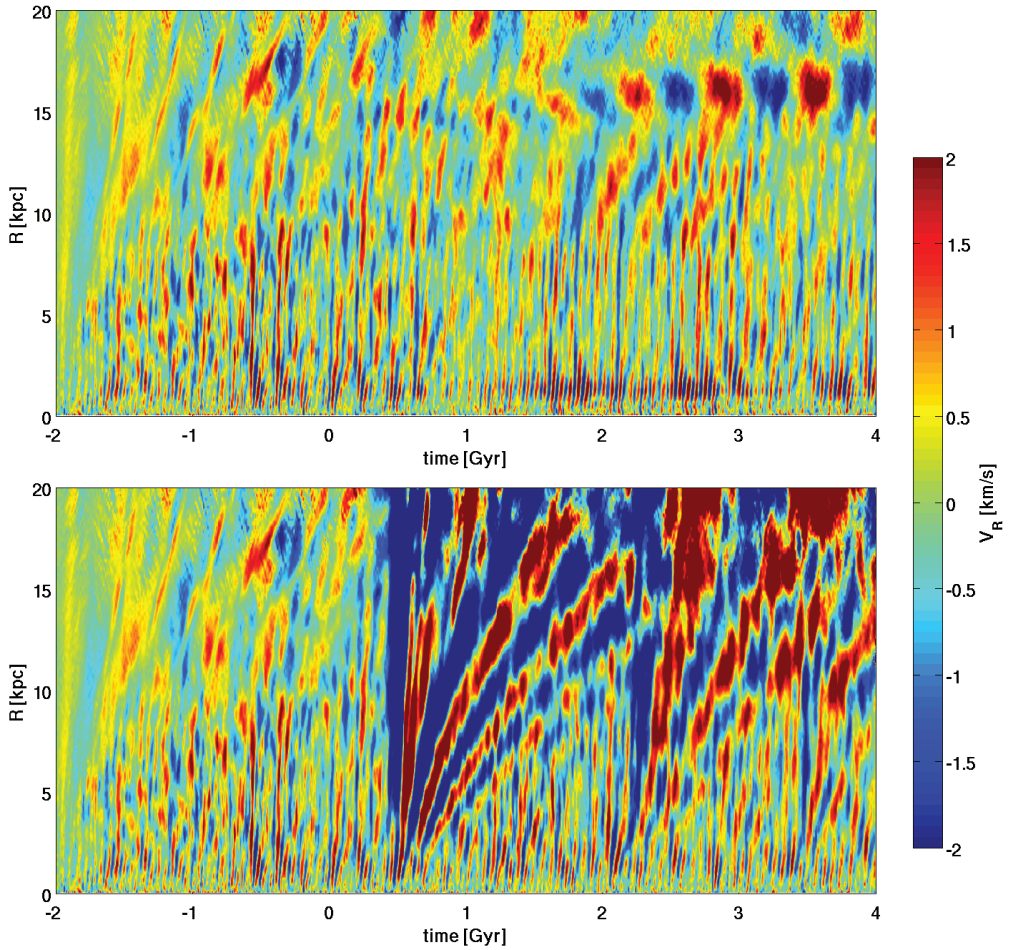

Figure 5.3.1: Surface plot of $V_R)R, t+$real component for m [3 harmonics, in the case of isolated (top) and Aq-F2-1e10 (bottom) runs across the disc's radial range. The colour map corresponds to the amplitude of the represented quantity.

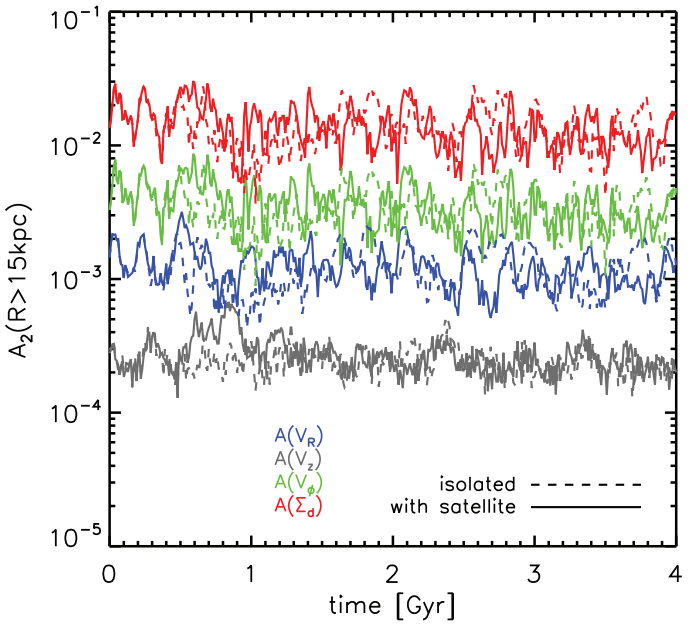

Figure 5.3.2: m [3 mode amplitude calculated using the Fourier transform of the disc surface density (red), radial (blue), vertical (gray) and tangential (green) velocity harmonics, in the case of isolated (dashed) and with satellite (solid) runs. Only disc particles with $R <$ h (scale radius of the disc) are incorporated for this calculation, in order to focus on the bar region.

crossing. Such rise lasts for $\approx$ 2 Gyr before decaying, in the case of $A_{\tilde{V}_R}$, $A_{\tilde{V}_\phi}$ and $A_{\tilde{\Sigma}}$. The vertical amplitude $A_{\tilde{V}_z}$ shows a constant excitation throughout the simulation, of the order of 10^{-4}. The second pericentre passage contributes only to minor radial motion, seen as a peak in $A_{\tilde{V}_R}$ at 2.1 Gyr (Fig. 5.3.1). It seems the m [3 perturbation is ring–like, with large spirality and no noticeable radial motion.

Minor mergers are commonly associated with triggering of odd modes, specially m [2 (Dubinski et al., 2009). For Fig. 5.3.4, disc particles with $R > 15$ kpc are used to compute Fourier transform of m [2 harmonics. The general behaviour is similar to m [3 mode, with an overall excitation of all components. The radial amplitude decays just after 0.5 Gyr, unlike the m [3 case that lasted for 1 Gyr. The contribution is long–lived for vertical velocity and corresponds to the observed disc warping (Gómez et al., 2016b). The perturbation appears as a wave with components in ϕ and z. At later times, the warp translates into an only vertical co–rotating oscillation. The z motion is dominated by the asymmetric m [2 mode by factor of $\approx$2.5.

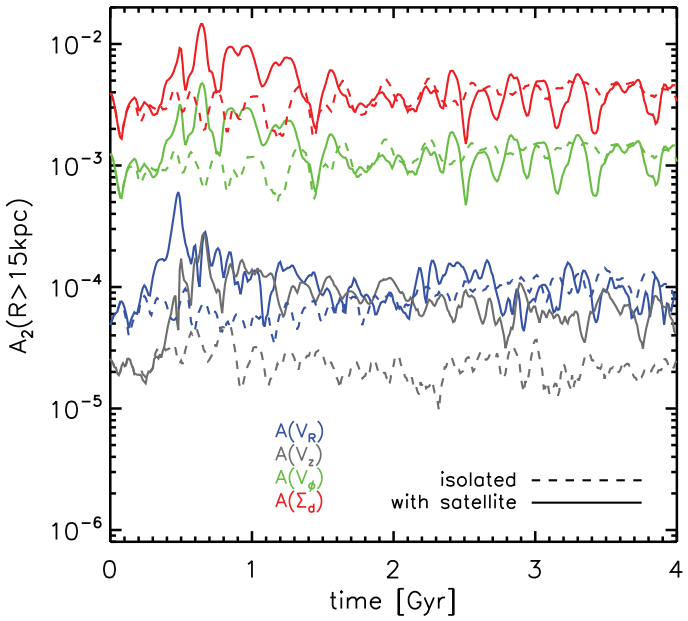

Figure 5.3.3: m [3 mode amplitude calculated using the Fourier transform of the disc surface density (red), radial (blue), vertical (black) and tangential (purple) velocity harmonics, in the case of isolated (dashed) and with satellite (solid) runs. Disc particles with $R > 15$ kpc are taken into account.

The contour levels in Fig. 5.3.5 correspond to the spectral maps of M_R harmonics (eq. 4.20) in radial space of m [3 (top) and m [2 (bottom) for Aq-F2-1e10, at t [1.67 Gyr. The filter time window has a width Λt [1.5 Gyr. The normalised pattern speed $^{-}{}_{p}$, in units of 100 kms^{-1}, is on the y-axis. The solid curves indicate the circular velocity $^{-})R+$profile, together with the inner and outer Lindblad resonances, $^{-})R+\equiv \kappa/3$. The dotted lines represent $^{-})R+\equiv \kappa/5$. The contours are spaced evenly in logarithmic scale and range from 1 to 100% of the maximum value. Also the highest amplitudes are identified with red crosses, which allows us to visualise the radial distribution of different modes. The m [3 mode is dominant in the region $4 < R < 12$ kpc and there exist multiple modes of different amplitudes, with peaks confined within $^{-})R+ \kappa/5$ and the outer Lindblad resonance. On the other hand, as concluded from Fig. 5.3.4, the m [2 instability leads in $R > 10$ kpc, with pattern speeds < 30 kms^{-1}.

The heating is more significant in the outer regions – $R > 21$ kpc – by a factor

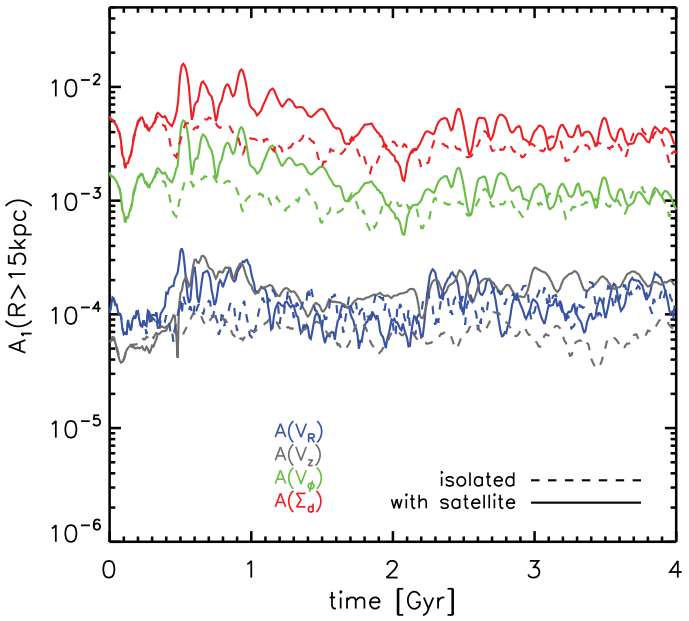

Figure 5.3.4: Time evolution of m [2 mode amplitude calculated using the Fourier transform of the disc surface density (red), radial (blue), vertical (gray) and tangential (green) velocity harmonics, in the case of isolated (dashed) and with satellite (solid) runs. Disc particles with $R > 15$ kpc are taken into account.

of 4–5 and is localised among certain azimuthal cuts. Although we observe a constant vertical heating across the disc, in the radial range $5 < R < 26$ kpc; there is a decreasing trend for the deposited vertical kinetic energy as we move away from the Galactic centre. Only a fraction of the total vertical kinetic energy lies in the outer disc. The passage of a massive perturber results in a combination of m [2 and m [3 unstable modes. The asymmetric m [2 mode is significant for distances greater than 15 kpc, and translates into the observed warp (≈ 5 kpc). In addition, oscillatory ring-like like features similar to the Monoceros ring (Xu et al., 2015), are seen in our simulations at $R > 21$ kpc.

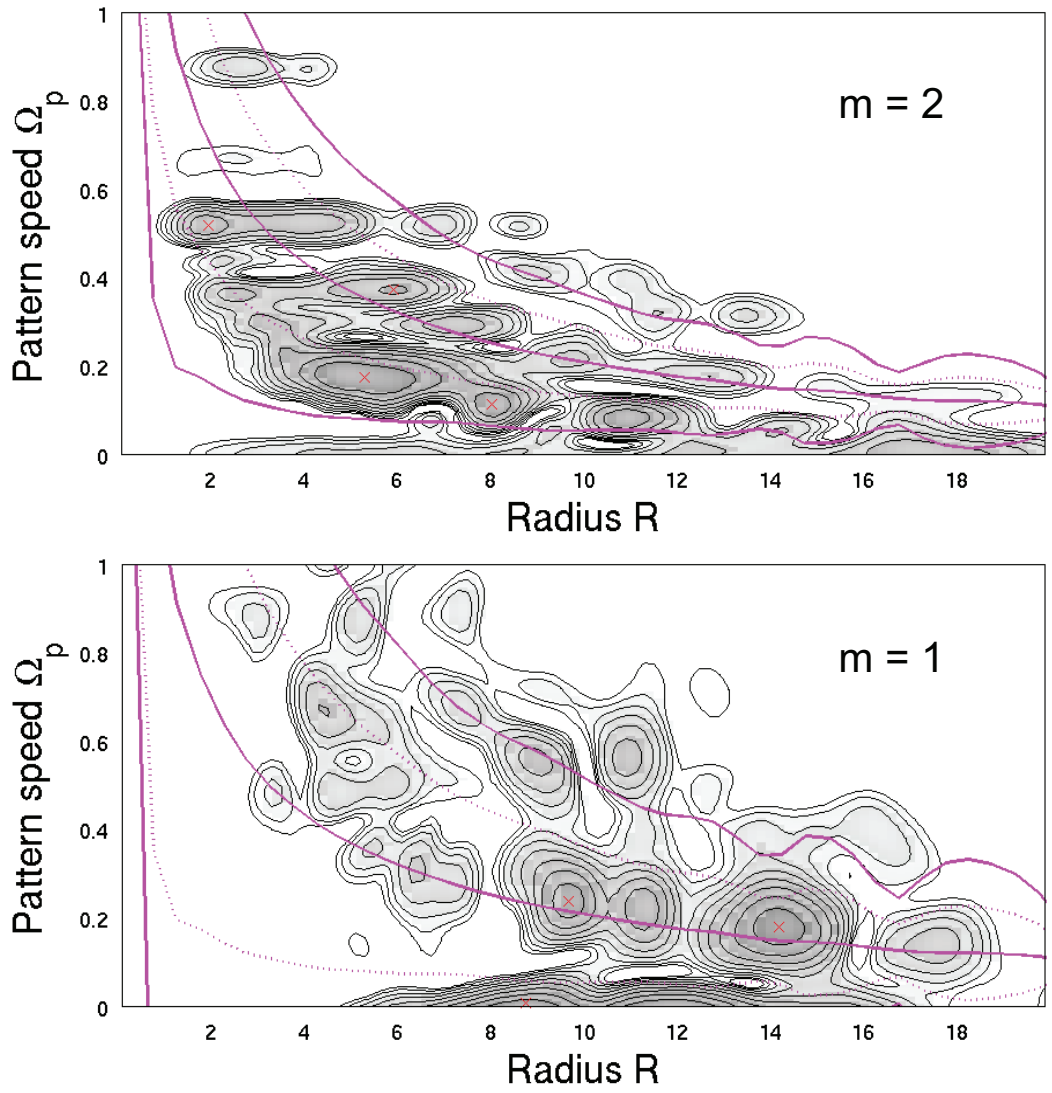

Figure 5.3.5: Spectral maps of M_R of m [3 (top) and m [2 (bottom) modes for Aq-F2-1e10, corresponding to t [6.7 Gyr with time window Λt [1.5 Gyr. The y-axis corresponds to the normalised pattern speed of instabilities. The contour levels range from 1 to 100%, evenly spaced in logarithmic scale. Also, the solid pink curves show the profile of circular velocity $^{-})R+_{\mp}$ together with the inner and outer Lindblad resonances, $^{-})R+\equiv \kappa/3$. The dotted lines represent $^{-})R+\equiv \kappa/5$. The red crosses mark the instabilities with maximum values.

"Raise your words, not voice. It is rain that grows flowers, not thunder."

- Jalaluddin Rumi

6 Summary & Outlook

6.1 Summary

Th ambition of this study was to understand the significance of the impact of satellites on the dynamics of the Milky Way disc. For this purpose, we used realistic initial conditions for the DM substructures from the cosmological simulations of Milky Way-like dark matter haloes. Such impacts are analysed in the form of vertical heating of the Galactic disc in the presence of satellite galaxies, together with excitation of unstable modes in the disc. This work benefits from four major assets: 1. N-body simulations that reach resolutions of 40 parsecs for the disc in the vertical direction, 2. initial conditions for the multi-component Milky Way galaxy, residing in much better equilibrium and steady state in the isolated case compared to previous works, 3. realistic initial conditions for DM substructures and 4. statistical set of initial conditions performed for the first time. Within the first part of the PhD, the vertical heating of the Galactic disc was investigated. This included an analysis of the properties of subhaloes from different simulation suites. In final part we studied the disc dynamics and the evolution of unstable modes due to interaction with satellite galaxies.

To have a statistically robust understanding of the satellites infall process, we used a distribution of subhaloes from seven cosmological simulations including six Aquarius simulations (at level 2 resolution) together with the Via Lactea II. We used the $z = 0$ snapshots containing a few hundred thousands DM subhaloes. The masses, velocities and positions of all the subhaloes were normalised using the ratio between the host DM halo masses (M_{200}) of the corresponding simulations and that of Aq-D2. The subhaloes at the low mass end of the distribution only consist of a few hundred particles, therefore we decided to consider only objects with the tidal mass $M_{\rm tid} \sim 10^6\ M_\odot$ for all our analysis (section 2.1). The fraction of total DM mass residing within substructures, $f_{\rm sub}$, is a measure of the clumpiness of the system and ranges from 5% for VLII to 14% within r_{50} (radius with mean density 50 times the background density) of the host halo. Such a range is an indication for the cosmic scatter of the DM mass distribution in different simulations. In all simulations, this fraction drops by three orders of magnitude as we move towards the inner parts of the main haloes.

The orbits of these subhaloes were integrated in the presence of their background host halo potential, to identify the crossed subhaloes which come closer than 25 kpc to the centre. The percentage fraction of these crossed subhaloes ranges from 6.9% to 14.5% (section 2.2). The cumulative subhalo mass distribution and the maximum circular velocity distributions of the crossed subhaloes show a similar slope as the total population for all the 7 simulations, implying the crossed sample is a good representative of the total. The crossed candidates located at $r > 100$ kpc contribute less than 20% to the total number of subhaloes at the corresponding radii, while more than 50% of the *total* crossed objects originate from this outer region. There exists a rising trend for the concentration of subhaloes $c_{\rm tid}$ with increasing distance from the host halo's centre. Crossed candidates located at $r > 100$ kpc have lower $c_{\rm tid}$ than the total population. Considering the large contribution of objects at this distance to the crossed sample together with higher mean concentration of the total sample, crossed candidates show a shift towards lower $c_{\rm tid}$ across the whole mass range by factor of 1.35. The full statistics of subhaloes are provided in Section 2.3.

The impact strength of these subhaloes is expected to scale $\propto M_{\rm tid}^2$, hence we chose only the crossed subhaloes with $M_{\rm tid} \sim 10^8\ M_\odot$ to use in our N-body simulations. Aq-F2 has the most number of candidates satisfying this criteria

with 24 subhaloes, while Aq-E2 has the least with only 12. Four subhaloes with $M_{\rm tid} \sim 10^9\ M_\odot$ reside in Aq-D2, while Aq-F2 is the only simulation that has one candidate with $M_{\rm tid} \sim 10^{10}\ M_\odot$. The initial conditions for our Milky Way galaxies were generated using the GalIC code (Yurin and Springel, 2014) with a thin exponential disc, a Hernquist bulge and a matching Hernquist DM halo for the original NFW host haloes (section 3.1). The parallelised N-body particle-mesh code SUPERBOX-10 was used to perform the simulations with three nested grids of different resolutions per galaxy. In the case of the disc, we used 10 million particles in order to suppress any unwanted perturbations caused by low number statistics in the disc. The isolated MW systems were evolved for 2 Gyr so that the components could adapt to their environment and also reach an equilibrium state. The subhalo candidates with $M_{\rm tid} \sim 10^8\ M_\odot$ for each simulation were inserted according to their initial positions and velocities extracted from the cosmological simulations. These systems were evolved for 2 Gyr, while the isolated cases were also simulated in parallel as control group.

The vertical heating of the galactic disc was determined by measuring the root-mean-square of the disc thickness $z_{\rm rms}$ and the vertical velocity dispersion squared σ_z^2 in the solar neighbourhood and across the disc. We observe a flaring in the outer parts of the disc where the mean value for the increase of the thickness due to satellites at R [26 kpc after 2 Gyr is about 100 pc with respect to the isolated case, including all seven simulations. However, if we exclude Aq-F2, the increase is only 30 pc. If we take into account the 2σ statistical dispersion around the mean, the thickness of the disc can reach 700 pc in the outer parts at 2 Gyr. It is important to note that it is easier to increase the vertical thickness of the particle distribution in the outer regions of the disc than in the inner parts, since these particles are less strongly bounded to the disc. The mean value of the heating, parametrized by, $\sigma_{z,t}^2$ - $\sigma_{z,0}^2$, at the end of our simulation drops strongly in the inner 4 kpc of the disc while becoming constant as we move outwards. This heating is 40 $\mathrm{km^2 s^{-2}}$, taking into account all the simulations, and less than 20 $\mathrm{km^2 s^{-2}}$ excluding Aq-F2. This means that the specific energy input is homogeneously distributed over the disc in the radial range 4-15 kpc. The isolated system also experiences self-heating of a similar value as the systems with satellites, neglecting Aq-F2 (section 3.4), showing that the impact of satellites is marginal.

According to the work done by Holmberg et al. (2009), the observed vertical

heating in the solar neighbourhood after 2 Gyr is expected to be $144\,\mathrm{km^2\,s^{-2}}$. The time evolution of the heating in the solar neighbourhood was analysed and a slowly increasing trend for $\sigma^2_{z,t}$ - $\sigma^2_{z,0}$ was observed in all our systems. For the first 0.4 Gyr a minimal heating was observed, since no massive satellite with $M_{\mathrm{tid}} \sim 5 \pm 10^8\ M_\odot$ crosses the disc within this period. However, the heating rate in the initial 1 Gyr is slightly higher than in the final 1 Gyr. The observed value of $144\,\mathrm{km^2\,s^{-2}}$ lies more than 3σ above the mean vertical heating taking into account all simulations. According to our analysis, the choice of orientation of the satellites distribution for the Aq-D2 case affects the measured vertical heating by less than 8% after 2 Gyr in the solar neighbourhood, which is lower than the self-heating of the isolated system. Thus, the orientation plays only a minor role in heating the disc vertically.

The measured heating from this analysis is sub-dominant and significantly smaller than in previous studies (e.g. Ardi et al. 2003; Kazantzidis et al. 2009). This mainly arises from the fact that our cosmological simulations do not include many subhaloes with $M_{\mathrm{tid}}/M_{\mathrm{disc}} > 0.2$, as was the case in other works, that are thought to heat the disc more significantly. Moreover, the DM clumpiness in Aquarius and VLII is much smaller than that in earlier cosmological simulations, as they suffered from lower mass resolution. The insufficient heating in our simulations could also be subject to further decrease if we allow for the presence of gas in the disc (Moster et al., 2010). Alternative mechanisms are more likely to dominate the heating of the disc. Heating by transient spiral arms or by disc growth via mass accretion are discussed in other works (e.g. Villalobos, Kazantzidis, and Helmi 2010; Martig, Minchev, and Flynn 2014). The increase of the disc surface density results in an enhanced σ_z, with contributions towards the heating ranging from less than 5% to 60% for increasing surface density, thus playing an important role in simulations which allow for disc growth. Coherent bending waves and buckling instabilities are other possible scenarios responsible for increasing the vertical dispersion of disc particles, although Toomre (1983) and Sellwood et al. (1998) have shown such mechanisms are inefficient in terms of reproducing the observed vertical heating. Also Lacey (1984) and Ida, Kokubo, and Makino (1993) found that the scattering of disc stars due to GMCs is able to redirect the peculiar velocities of stars out of the plane. However, the inputted energy is ineffective in increasing the velocity dispersion in the plane.

The results of this study show that the impact of the subhaloes on the vertical

heating of the Galactic disc is highly dependent on the high-mass end of the cosmological subhalo distribution – $M_{\rm tid} \sim 10^9\ M_\odot$. The differences between different simulations can be thought as cosmic variance calculated as the statistical dispersion around the mean value from all simulations. If we exclude the Aq-F2 simulation as the only simulation with one subhalo of $M_{\rm tid} \sim 7 \times 10^{10} M_\odot$, the impact of satellites reaches only the negligible value of 3 $\mathrm{km^2\,s^{-2}}$ at solar neighbourhood after 2 Gyr which is negligible. The best measure for the high mass satellites impact is the flaring of the disc, although no strong heating is measured. Such insignificant heating suggests that subhaloes are not responsible for the observed vertical heating of the thin disc. We conclude that 10-15% contribution to the observed heating may originate from the impact of subhaloes.

In addition to the heating of the Galactic disc, we were interested in excitation of modes in the disc plane. the importance of satellite infall on the process of bar-formation is discussed in chapter 4. The initial conditions for the MW galaxy were generated using the GalactICS code (Widrow et al., 2008). The bar unstable mode is present among all the runs, including the isolated case. The satellite crossing plays a role in terms of delaying or advancing the bar-formation. In order for a satellite to impact the bar-formation, the pericentric passage time is very important. Any incoming perturbation during the shot noise phase would not influence the bar mode; this is the regime where the amplitude of surface density harmonics is less than 1%. If such perturbations are induced between the end of the shot noise period T_1 and the early phase of the exponential growth T_2, they would delay/advance the bar mode. The fully-rescaled B-1 run with the most massive Aq-D2 crossed subhalo corresponds to earlier bar-formation compared to the isolated B-0m with pericentre passage time of 0.85 Gyr. On the other hand, mass-rescaled B-1m ($t_{\rm peri} \sim 1.7$ Gyr) results in a delay of ≈ 1.6 Gyr.

The analysis in chapter 3 was focused on the radial averaging of the heating due to satellites. The Aq-F2 run resulted in the the most significant heating, due to the satellite with $M_{\rm tid} \sim 7 \times 10^{10} M_\odot$. The localisation of the vertical heating was studied in chapter 5. The heating is more significant in the outer regions – $R > 21$ kpc – by factor of 4–5 and is localised among certain azimuthal cuts. Despite the constant heating for $5 < R < 26$ kpc, the deposited vertical kinetic energy decreases, moving away from the Galactic centre within this range. The disc is subject to warping of the order of ≈ 5 kpc in the outer parts. We also observe

a radial oscillatory behaviour for $R > 21$ kpc, similar to the observed features of the MW such as the Monoceros ring (Xu et al., 2015). The satellite impact is responsible for excitation of m [2 and 3 modes in the disc plane. The vertical velocity component of the asymmetric m [2 mode is dominant in the outer part (warping), while the rotation of the particles (V_ϕ) is influenced mostly by m [3. The excitation of surface density, radial and azimuthal velocity harmonics are short–lived and decay after ≈ 2 Gyr, although the warp survives longer.

6.2 Outlook

I would like to mention some of the further studies that can serve as suitable extensions to this work, such as addition of gas component to our simulations with the purpose of quantifying the impact of gas on the Galactic disc's vertical heating. Also, employing star-formation recipes and feedback processes would allow us to study the impact of infall on distribution of stars with different metallicities and kinematics. This heating analysis can be applied to an even larger sample of Milky Way-like cosmological haloes, such as the Caterpillar project with currently 24 Milky Way-size haloes and an estimated 60-70 haloes upon completion (Griffen et al., 2016).

The next stage of this work is an exploration of the remaining processes which contribute towards the Galactic disc heating, since we now have quantified the share from the infall of satellites using statistically relevant and high resolution analysis.

The impact of satellites on the bar-formation process is still subject of a more extensive analysis, in order to understand the true nature of such difference in bar development. Possible aspects include, phase locking between different modes and the phase shift of the satellite's orbit and the bar. Also, it is interesting to understand the connection between the energy of the excited perturbation induced by the satellite and the vertical heating of the disc. For future work, we would like to pursue a deeper study of the contribution of a massive perturber to the warping in the outer disc, and how such a feature translates into the localised heating.

References

Abadi, M. G., Navarro, J. F., Steinmetz, M., and Eke, V. R. "Simulations of Galaxy Formation in a Σ Cold Dark Matter Universe. I. Dynamical and Photometric Properties of a Simulated Disk Galaxy". *ApJ*, 591:499–514, 2003. URL http://adsabs.harvard.edu/abs/2003ApJ...591..499A.

Abadi, M. G., Navarro, J. F., and Steinmetz, M. "Stars beyond galaxies: the origin of extended luminous haloes around galaxies". *MNRAS*, 365:747–758, 2006. URL http://adsabs.harvard.edu/abs/2006MNRAS.365..747A.

Abraham, R. G., Merrifield, M. R., Ellis, R. S., et al. "The evolution of barred spiral galaxies in the Hubble Deep Fields North and South". *MNRAS*, 308:569–576, 1999. URL http://adsabs.harvard.edu/abs/1999MNRAS.308..569A.

Alam, S., Albareti, F. D., Allende Prieto, C., et al. "The Eleventh and Twelfth Data Releases of the Sloan Digital Sky Survey: Final Data from SDSS–III". *ApJS*, 219:12, 2015. URL http://adsabs.harvard.edu/abs/2015ApJS..219...12A.

Allgood, B., Flores, R. A., Primack, J. R., Kravtsov, A. V., Wechsler, R. H., Faltenbacher, A., and Bullock, J. S. "The shape of dark matter haloes: dependence on mass, redshift, radius and formation". *MNRAS*, 367:1781–1796, 2006. URL http://adsabs.harvard.edu/abs/2006MNRAS.367.1781A.

Alpher, R. A., Follin, J. W., and Herman, R. C. "Physical Conditions in the Initial Stages of the Expanding Universe". *Physical Review*, 92:1347–1361, 1953. URL http://adsabs.harvard.edu/abs/1953PhRv...92.1347A.

Araki, S. *"A Theoretical Study of the Stability of Disk Galaxies and Planetary Rings."*. PhD thesis, MIT, 1985. URL http://adsabs.harvard.edu/abs/1985PhDT.....32A.

Ardi, E., Tsuchiya, T., and Burkert, A. "Constraints of the Clumpiness of Dark Matter Halos through Heating of the Disk Galaxies". *ApJ*, 596:204–215, 2003. URL http://adsabs.harvard.edu/abs/2003ApJ...596..204A.

Athanassoula, E. "On the nature of bulges in general and of box/peanut bulges in particular: input from N–body simulations". *MNRAS*, 358:1477–1488, 2005. URL http://adsabs.harvard.edu/abs/2005MNRAS.358.1477A.

Athanassoula, E. and Sellwood, J. A. "Bi–symmetric instabilities of the Kuz'min/Toomre disc". *MNRAS*, 221:213–232, 1986. doi: 10.1093/mnras/221.2.213. URL http://adsabs.harvard.edu/abs/1986MNRAS.221..213A.

Bailin, J. "Evidence for Coupling between the Sagittarius Dwarf Galaxy and the Milky Way Warp". *ApJL*, 583:L79–L82, 2003. URL http://adsabs.harvard.edu/abs/2003ApJ...583L..79B.

Barnes, J. and Hut, P. "A hierarchical O(N log N) force-calculation algorithm". *Nature*, 324:446–449, 1986. URL http://adsabs.harvard.edu/abs/1986Natur.324..446B.

Baugh, C. M., Cole, S., and Frenk, C. S. "Faint galaxy counts as a function of morphological type in a hierarchical merger model". *MNRAS*, 282:L27–L32, 1996. URL http://adsabs.harvard.edu/abs/1996MNRAS.282L..27B.

Becker, R. H., Fan, X., White, R. L., et al. "Evidence for Reionization at $z \approx 7$: Detection of a Gunn-Peterson Trough in a z [7.39 Quasar". *AJ*, 122:2850–2857, 2001. URL http://adsabs.harvard.edu/abs/2001AJ....122.2850B.

Bédorf, J., Gaburov, E., and Portegies Zwart, S. "Bonsai: A GPU Tree–Code". volume 453, page 325, 2012a. URL http://adsabs.harvard.edu/abs/2012ASPC..453..325B.

Bédorf, J., Gaburov, E., and Portegies Zwart, S. "Bonsai: N–body GPU tree–code", 2012b. URL http://adsabs.harvard.edu/abs/2012ascl.soft12001B.

Belokurov, V., Zucker, D. B., Evans, N. W., et al. "The Field of Streams: Sagittarius and Its Siblings". *ApJL*, 642:L137–L140, 2006. URL http://adsabs.harvard.edu/abs/2006ApJ...642L.137B.

Bertschinger, E. "Simulations of Structure Formation in the Universe". *ARA&A*, 36:599–654, 1998. URL http://adsabs.harvard.edu/abs/1998ARA%26A..36..599B.

Bien, R., Brandt, T., and Just, A. "Simulating sinking satellites with superbox–10". *MNRAS*, 428:1631–1642, 2013. URL http://adsabs.harvard.edu/abs/2013MNRAS.428.1631B.

Binney, J. and Tremaine, S. *"Galactic Dynamics: Second Edition"*. Princeton University Press, 2008. URL http://adsabs.harvard.edu/abs/2008gady.book....B.

Bird, J. C., Kazantzidis, S., and Weinberg, D. H. "Radial mixing in galactic discs: the effects of disc structure and satellite bombardment". *MNRAS*, 420:913–925, 2012. URL http://adsabs.harvard.edu/abs/2012MNRAS.420..913B.

Bissantz, N. and Gerhard, O. "Spiral arms, bar shape and bulge microlensing in the Milky Way". *MNRAS*, 330:591–608, 2002. URL http://adsabs.harvard.edu/abs/2002MNRAS.330..591B.

Bland-Hawthorn, J. and Gerhard, O. "The Galaxy in Context: Structural, Kinematic and Integrated Properties". *arXiv*, 2016. URL http://adsabs.harvard.edu/abs/2016arXiv160207702B.

Blitz, L. and Spergel, D. N. "Direct evidence for a bar at the Galactic center". *ApJ*, 379:631–638, 1991. URL http://adsabs.harvard.edu/abs/1991ApJ...379..631B.

Bond, N. A., Ivezić, Ž., Sesar, B., et al. "The Milky Way Tomography wić with SDSS. III. Stellar Kinematics". *ApJ*, 716:1–29, 2010. URL http://adsabs.harvard.edu/abs/2010ApJ...716....1B.

Borne, K. D., Bushouse, H., Colina, L., et al. A Morphological Classification Scheme for ULIRGs. *Ap&SS*, 266:137–142, 1999. URL http://adsabs.harvard.edu/abs/1999Ap%26SS.266..137B.

Bournaud, F., Combes, F., Jog, C. J., and Puerari, I. "Lopsided spiral galaxies: evidence for gas accretion". *A&A*, 438:507–520, 2005. URL http://adsabs.harvard.edu/abs/2005A%26A...438..507B.

Bovy, J., Rix, H.-W., Hogg, D. W., et al. "The Vertical Motions of Mono–abundance Sub–populations in the Milky Way Disk". *ApJ*, 755:115, 2012a. URL http://adsabs.harvard.edu/abs/2012ApJ...755..115B.

Bovy, J., Rix, H.-W., Liu, C., et al. "The Spatial Structure of Mono–abundance Sub–populations of the Milky Way Disk". *ApJ*, 753:148, 2012b. URL http://adsabs.harvard.edu/abs/2012ApJ...753..148B.

Boylan-Kolchin, M., Springel, V., White, S. D. M., et al. "Resolving cosmic structure formation with the Millennium–II Simulation". *MNRAS*, 398:1150–1164, 2009. URL http://adsabs.harvard.edu/abs/2009MNRAS.398.1150B.

Brooks, A. M., Kuhlen, M., Zolotov, A., and Hooper, D. "A Baryonic Solution to the Missing Satellites Problem". *ApJ*, 765:22, 2013. URL http://adsabs.harvard.edu/abs/2013ApJ...765...22B.

Brown, W. R., Geller, M. J., Kenyon, S. J., et al. "Mapping the Inner Halo of the Galaxy with 2MASS–Selected Horizontal–Branch Candidates". *AJ*, 127:1555–1566, 2004. URL http://adsabs.harvard.edu/abs/2004AJ....127.1555B.

Bullock, J. S., Dekel, A., Kolatt, T. S., et al. "A Universal Angular Momentum Profile for Galactic Halos". *ApJ*, 555:240–257, 2001. URL http://adsabs.harvard.edu/abs/2001ApJ...555..240B.

Carlberg, R. G. "The vertical structure of galactic disks". *ApJ*, 322:59–63, 1987. URL http://adsabs.harvard.edu/abs/1987ApJ...322...59C.

Christensen, C. R., Governato, F., Quinn, T., et al. "The effect of models of the interstellar media on the central mass distribution of galaxies". *MNRAS*, 440:2843–2859, 2014. URL http://adsabs.harvard.edu/abs/2014MNRAS.440.2843C.

Clowe, D., Gonzalez, A., and Markevitch, M. "Weak–Lensing Mass Reconstruction of the Interacting Cluster 1E 0657–558: Direct Evidence for the Existence of Dark Matter". *ApJ*, 604:596–603, 2004. URL http://adsabs.harvard.edu/abs/2004ApJ...604..596C.

Cooper, A. P., Parry, O. H., Lowing, B., et al. "Formation of in situ stellar haloes in Milky Way–mass galaxies". *MNRAS*, 454:3185–3199, 2015. URL http://adsabs.harvard.edu/abs/2015MNRAS.454.3185C.

Davis, M., Efstathiou, G., Frenk, C. S., and White, S. D. M. "The evolution of large-scale structure in a universe dominated by cold dark matter". *ApJ*, 292:371–394, 1985. URL http://adsabs.harvard.edu/abs/1985ApJ...292..371D.

de Grijs, R. and Peletier, R. F. "Tracing the vertical composition of disc galaxies through colour gradients". *MNRAS*, 313:800–814, 2000. URL http://adsabs.harvard.edu/abs/2000MNRAS.313..800D.

de Vaucouleurs, G. "Interpretation of velocity distribution of the inner regions of the Galaxy". volume 20 of *IAU Symposium*, page 195, 1964. URL http://adsabs.harvard.edu/abs/1964IAUS...20..195D.

Deason, A. J., Belokurov, V., and Evans, N. W. "The Milky Way stellar halo out to 40 kpc: squashed, broken but smooth". *MNRAS*, 416:2903–2915, 2011. URL http://adsabs.harvard.edu/abs/2011MNRAS.416.2903D.

Debattista, V. P., Carollo, C. M., Mayer, L., and Moore, B. "The Kinematic Signature of Face–On Peanut–shaped Bulges". *ApJ*, 628:678–694, 2005. URL http://adsabs.harvard.edu/abs/2005ApJ...628..678D.

Dehnen, W. and Binney, J. "Mass models of the Milky Way". *MNRAS*, 294:429, 1998. URL http://adsabs.harvard.edu/abs/1998MNRAS.294..429D.

Diemand, J., Kuhlen, M., and Madau, P. "Early Supersymmetric Cold Dark Matter Substructure". *ApJ*, 649:1–13, 2006. URL http://adsabs.harvard.edu/abs/2006ApJ...649....1D.

Diemand, J., Kuhlen, M., and Madau, P. "Formation and Evolution of Galaxy Dark Matter Halos and Their Substructure". *ApJ*, 667:859–877, 2007. URL http://adsabs.harvard.edu/abs/2007ApJ...667..859D.

Diemand, J., Kuhlen, M., Madau, P., Zemp, M., Moore, B., Potter, D., and Stadel, J. "Clumps and streams in the local dark matter distribution". *Nature*, 454: 735–738, 2008. URL http://adsabs.harvard.edu/abs/2008Natur.454..735D.

D'Onghia, E., Madau, P., Vera-Ciro, C., et al. "Excitation of Coupled Stellar Motions in the Galactic Disk by Orbiting Satellites". *ApJ*, 823:4, 2016. URL http://adsabs.harvard.edu/abs/2016ApJ...823....4D.

Dubinski, J., Berentzen, I., and Shlosman, I. "Anatomy of the Bar Instability in Cuspy Dark Matter Halos". *ApJ*, 697:293–310, 2009. URL http://adsabs.harvard.edu/abs/2009ApJ...697..293D.

Dwek, E., Arendt, R. G., Hauser, M. G., et al. "Morphology, near–infrared luminosity, and mass of the Galactic bulge from COBE DIRBE observations". *ApJ*, 445: 716–730, 1995. URL http://adsabs.harvard.edu/abs/1995ApJ...445..716D.

Einstein, A. "Zur Elektrodynamik bewegter Körper". *Annalen der Physik*, 322: 891–921, 1905. URL http://adsabs.harvard.edu/abs/1905AnP...322..891E.

Einstein, A. "Die Feldgleichungen der Gravitation". *Sitzungsberichte der Königlich Preußischen Akademie der Wissenschaften (Berlin)*, pages 844–847, 1915. URL http://adsabs.harvard.edu/abs/1915SPAW.......844E.

Einstein, A. "Kosmologische Betrachtungen zur allgemeinen Relativitätstheorie". *Sitzungsberichte der Königlich Preußischen Akademie der Wissenschaften (Berlin)*, pages 142–152, 1917. URL http://adsabs.harvard.edu/abs/1917SPAW.......142E.

Eisenstein, D. J. and Hu, W. "Power Spectra for Cold Dark Matter and Its Variants". *ApJ*, 511:5–15, 1999. URL http://adsabs.harvard.edu/abs/1999ApJ...511....5E.

Elmegreen, B. G. "Galactic Bulge Formation as a Maximum Intensity Starburst". *ApJ*, 517:103–107, 1999. URL http://adsabs.harvard.edu/abs/1999ApJ...517..103E.

Evans, N. W., Gyuk, G., Turner, M. S., and Binney, J. "The LMC Microlensing Events: Evidence for a Warped and Flaring Milky Way Disk?". *ApJL*, 501:L45–L49, 1998. URL http://adsabs.harvard.edu/abs/1998ApJ...501L..45E.

Faccioli, L., Smith, M. C., Yuan, H.-B., et al. "RR Lyrae in XSTPS: The Halo Density Profile in the North Galactic Cap". *ApJ*, 788:105, 2014. URL http://adsabs.harvard.edu/abs/2014ApJ...788..105F.

Falco, E. E., Kochanek, C. S., and Muñoz, J. A. "Limits on Cosmological Models from Radio–selected Gravitational Lenses". *ApJ*, 494:47–59, 1998. URL http://adsabs.harvard.edu/abs/1998ApJ...494...47F.

Fellhauer, M., Kroupa, P., Baumgardt, H., Bien, R., Boily, C. M., Spurzem, R., and Wassmer, N. "SUPERBOX - an efficient code for collisionless galactic dynamics". *NewA*, 5:305–326, 2000. URL http://adsabs.harvard.edu/abs/2000NewA....5..305F.

Flynn, C., Holmberg, J., Portinari, L., Fuchs, B., and Jahreiß, H. "On the mass–to–light ratio of the local Galactic disc and the optical luminosity of the Galaxy". *MNRAS*, 372:1149–1160, 2006. URL http://adsabs.harvard.edu/abs/2006MNRAS.372.1149F.

Font, A. S., Navarro, J. F., Stadel, J., and Quinn, T. "Halo Substructure and Disk Heating in a Σ Cold Dark Matter Universe". *ApJ*, 563:L1–L4, 2001. URL http://adsabs.harvard.edu/abs/2001ApJ...563L...1F.

Font, A. S., McCarthy, I. G., Crain, R. A., et al. "Cosmological simulations of the formation of the stellar haloes around disc galaxies". *MNRAS*, 416:2802–2820, 2011. URL http://adsabs.harvard.edu/abs/2011MNRAS.416.2802F.

Freeman, K. C. In Sundelius, B., editor, *"Dynamics of Disc Galaxies"*, page 15. Göteborgs Univ., 1991. URL http://adsabs.harvard.edu/abs/1991dodg.conf...15F.

Friedmann, A. "Über die Krümmung des Raumes". *Zeitschrift fur Physik*, 10:377–386, 1922. URL http://adsabs.harvard.edu/abs/1922ZPhy...10..377F.

Fuchs, B., Dettbarn, C., Rix, H.-W., et al. "The Kinematics of Late-Type Stars in the Solar Cylinder Studied with SDSS Data". *AJ*, 137:4149–4159, 2009. URL http://adsabs.harvard.edu/abs/2009AJ....137.4149F.

Gamow, G. "Expanding Universe and the Origin of Elements". *Physical Review*, 70:572–573, 1946. URL http://adsabs.harvard.edu/abs/1946PhRv...70..572G.

Gerhard, O. "Pattern speeds in the Milky Way.". *"Memorie della Societa Astronomica Italiana Supplementi"*, 18:185, 2011. URL http://adsabs.harvard.edu/abs/2011MSAIS..18..185G.

Ghigna, S., Moore, B., Governato, F., Lake, G., Quinn, T., and Stadel, J. "Dark matter haloes within clusters". *MNRAS*, 300:146–162, 1998. URL http://adsabs.harvard.edu/abs/1998MNRAS.300..146G.

Gillessen, S., Eisenhauer, F., Trippe, S., Alexander, T., Genzel, R., Martins, F., and Ott, T. "Monitoring Stellar Orbits Around the Massive Black Hole in the Galactic Center". *ApJ*, 692:1075–1109, 2009. URL http://adsabs.harvard.edu/abs/2009ApJ...692.1075G.

Gilmore, G. and Reid, N. "New light on faint stars. III – Galactic structure towards the South Pole and the Galactic thick disc". *MNRAS*, 202:1025–1047, 1983. URL http://adsabs.harvard.edu/abs/1983MNRAS.202.1025G.

Gilmore, G., Randich, S., Asplund, M., et al. "The Gaia–ESO Public Spectroscopic Survey". *The Messenger*, 147:25–31, 2012. URL http://adsabs.harvard.edu/abs/2012Msngr.147...25G.

Goldreich, P. and Lynden-Bell, D. "II. Spiral arms as sheared gravitational instabilities". *MNRAS*, 130:125, 1965. URL http://adsabs.harvard.edu/abs/1965MNRAS.130..125G.

Gómez, F. A., White, S. D. M., Grand, R. J. J., et al. "Warps and waves in fully cosmological models of galactic discs". *ArXiv e-prints*, June 2016a. URL http://adsabs.harvard.edu/abs/2016arXiv160606295G.

Gómez, F. A., White, S. D. M., Marinacci, F., and others. "A fully cosmological model of a Monoceros–like ring". *MNRAS*, 456:2779–2793, 2016b. URL http://adsabs.harvard.edu/abs/2016MNRAS.456.2779G.

Gonzalez, O. A. and Gadotti, D. "The Milky Way Bulge: Observed Properties and a Comparison to External Galaxies". *Galactic Bulges*, 418:199, 2016. URL http://adsabs.harvard.edu/abs/2016ASSL..418..199G.

Governato, F., Willman, B., Mayer, L., et al. "Forming disc galaxies in ΣCDM simulations". *MNRAS*, 374:1479–1494, 2007. URL http://adsabs.harvard.edu/abs/2007MNRAS.374.1479G.

Griffen, B. F., Ji, A. P., Dooley, G. A., et al. "The Caterpillar Project: A Large Suite of Milky Way Sized Halos". *ApJ*, 818:10, 2016. URL http://adsabs.harvard.edu/abs/2016ApJ...818...10G.

Hernández-Toledo, H. M., Avila-Reese, V., Conselice, C. J., and Puerari, I. "The Structural Properties of Isolated Galaxies, Spiral-Spiral Pairs, and Mergers: The Robustness of Galaxy Morphology during Secular Evolution". *AJ*, 129:682–697, 2005. URL http://adsabs.harvard.edu/abs/2005AJ....129..682H.

Hernquist, L. "Structure of merger remnants. I – Bulgeless progenitors". *ApJ*, 400: 460–475, 1992. URL http://adsabs.harvard.edu/abs/1992ApJ...400..460H.

Hinshaw, G., Larson, D., and Komatsu, E. e. a. "Nine-year Wilkinson Microwave Anisotropy Probe (WMAP) Observations: Cosmological Parameter Results". *ApJS*, 208:19, 2013. URL http://adsabs.harvard.edu/abs/2013ApJS..208...19H.

Hockney, R. W. and Eastwood, J. W. *"Computer simulation using particles"*. Bristol: Hilger, 1988. URL http://adsabs.harvard.edu/abs/1988csup.book.....H.

Hohl, F. "Integration Methods where Force is Obtained from the Smoothed Gravitational Field. *Ap&SS*, 14:168–178, 1971. URL http://adsabs.harvard.edu/abs/1971Ap%26SS..14..168H.

Holmberg, J., Nordström, B., and Andersen, J. "The Geneva–Copenhagen survey of the Solar neighbourhood II. New uvby calibrations and rediscussion of stellar ages, the G dwarf problem, age–metallicity diagram, and heating mechanisms of the disk". *A&A*, 475:519–537, 2007. URL http://adsabs.harvard.edu/abs/2007A%26A...475..519H.

Holmberg, J., Nordström, B., and Andersen, J. "The Geneva–Copenhagen survey of the solar neighbourhood. III. Improved distances, ages, and kinematics". *A&A*, 501:941–947, 2009. URL http://adsabs.harvard.edu/abs/2009A%26A...501..941H.

Hopkins, P. F., Hernquist, L., Cox, T. J., Younger, J. D., and Besla, G. "The Radical Consequences of Realistic Satellite Orbits for the Heating and Implied Merger Histories of Galactic Disks". *ApJ*, 688:757–769, 2008. URL http://adsabs.harvard.edu/abs/2008ApJ...688..757H.

Howard, C. D., Rich, R. M., Reitzel, D. B., et al. "The Bulge Radial Velocity Assay (BRAVA). I. Sample Selection and a Rotation Curve". *ApJ*, 688:1060–1077, 2008. URL http://adsabs.harvard.edu/abs/2008ApJ...688.1060H.

Hubble, E. "A Relation between Distance and Radial Velocity among Extra-Galactic Nebulae". *Proceedings of the National Academy of Science*, 15:168–173, 1929. URL http://adsabs.harvard.edu/abs/1929PNAS...15..168H.

Ibata, R. A., Gilmore, G., and Irwin, M. J. "A dwarf satellite galaxy in Sagittarius". *Nature*, 370:194–196, 1994. URL http://adsabs.harvard.edu/abs/1994Natur.370..194I.

Ibata, R. A., Wyse, R. F. G., Gilmore, G., et al. "The Kinematics, Orbit, and Survival of the Sagittarius Dwarf Spheroidal Galaxy". *AJ*, 113:634–655, 1997. URL http://adsabs.harvard.edu/abs/1997AJ....113..634I.

Ida, S., Kokubo, E., and Makino, J. "The Origin of Anisotropic Velocity Dispersion of Particles in a Disc Potential". *MNRAS*, 263:875, 1993. URL http://adsabs.harvard.edu/abs/1993MNRAS.263..875I.

Ivezić, Ž., Sesar, B., Jurić, M., et al. "The Milky Way Tomography with SDSS. II. Stellar Metallicity". *ApJ*, 684:287–325, 2008. URL http://adsabs.harvard.edu/abs/2008ApJ...684..287I.

Julian, W. H. and Toomre, A. "Non–Axisymmetric Responses of Differentially Rotating Disks of Stars". *ApJ*, 146:810, 1966. URL http://adsabs.harvard.edu/abs/1966ApJ...146..810J.

Jurić, M., Ivezić, Ž., Brooks, A., et al. "The Milky Way Tomography with SDSS. I. Stellar Number Density Distribution". *ApJ*, 673:864–914, 2008. URL http://adsabs.harvard.edu/abs/2008ApJ...673..864J.

Just, A. and Jahreiß, H. “Towards a fully consistent Milky Way disc model – I. The local model based on kinematic and photometric data”. *MNRAS*, 402:461–478, 2010. URL http://adsabs.harvard.edu/abs/2010MNRAS.402..461J.

Just, A., Möllenhoff, C., and Borch, A. “An evolutionary disc model of the edge-on galaxy NGC 5907”. *A&A*, 459:703=–716, 2006. URL http://adsabs.harvard.edu/abs/2006A%26A...459..703J.

Just, A., Khan, F. M., Berczik, P., Ernst, A., and Spurzem, R. “Dynamical friction of massive objects in galactic centres”. *MNRAS*, 411:653–674, 2011. URL http://adsabs.harvard.edu/abs/2011MNRAS.411..653J.

Kannan, R., Macciò, A. V., Pasquali, A., Moster, B. P., and Walter, F. “Interaction between Dark Matter Sub-halos and a Galactic Gaseous Disk”. *ApJ*, 746:10, 2012. URL http://adsabs.harvard.edu/abs/2012ApJ...746...10K.

Kauffmann, G., White, S. D. M., and Guiderdoni, B. “The Formation and Evolution of Galaxies Within Merging Dark Matter Haloes”. *MNRAS*, 264:201, 1993. URL http://adsabs.harvard.edu/abs/1993MNRAS.264..201K.

Kazantzidis, S., Bullock, J. S., Zentner, A. R., Kravtsov, A. V., and Moustakas, L. A. “Cold Dark Matter Substructure and Galactic Disks. I. Morphological Signatures of Hierarchical Satellite Accretion”. *ApJ*, 688:254–276, 2008. URL http://adsabs.harvard.edu/abs/2008ApJ...688..254K.

Kazantzidis, S., Zentner, A. R., Kravtsov, A. V., Bullock, J. S., and Debattista, V. P. “Cold Dark Matter Substructure and Galactic Disks. II. Dynamical Effects of Hierarchical Satellite Accretion”. *ApJ*, 700:1896–1920, 2009. URL http://adsabs.harvard.edu/abs/2009ApJ...700.1896K.

Kent, S. M., Dame, T. M., and Fazio, G. “Galactic structure from the Spacelab infrared telescope. II – Luminosity models of the Milky Way”. *ApJ*, 378:131–138, 1991. URL http://adsabs.harvard.edu/abs/1991ApJ...378..131K.

Khoperskov, A. V., Just, A., Korchagin, V. I., and Jalali, M. A. “High resolution simulations of unstable modes in a collisionless disc”. *A&A*, 473:31–40, 2007. URL http://adsabs.harvard.edu/abs/2007A%26A...473...31K.

Klypin, A., Kravtsov, A. V., Valenzuela, O., and Prada, F. “Where Are the Missing Galactic Satellites?”. *ApJ*, 522:82–92, 1999. URL http://adsabs.harvard.edu/abs/1999ApJ...522...82K.

Kormendy, J. ”Rotation of the bulge components of barred galaxies”. *ApJ*, 257: 75–88, 1982. URL http://adsabs.harvard.edu/abs/1982ApJ...257...75K.

Kravtsov, A. V., Klypin, A. A., and Khokhlov, A. M. “Adaptive Refinement Tree: A New High–Resolution N–Body Code for Cosmological Simulations”. *ApJS*, 111: 73–94, 1997. URL http://adsabs.harvard.edu/abs/1997ApJS..111...73K.

Kuijken, K. and Dubinski, J. "Nearly Self–Consistent Disc / Bulge / Halo Models for Galaxies". *MNRAS*, 277:1341, 1995. URL http://adsabs.harvard.edu/abs/1995MNRAS.277.1341K.

Kuijken, K. and Gilmore, G. "The Mass Distribution in the Galactic Disc – Part III – the Local Volume Mass Density". *MNRAS*, 239:651–664, 1989. URL http://adsabs.harvard.edu/abs/1989MNRAS.239..651K.

Lacey, C. G. "The influence of massive gas clouds on stellar velocity dispersions in galactic discs". *MNRAS*, 208:687–707, 1984. URL http://adsabs.harvard.edu/abs/1984MNRAS.208..687L.

Lee, Y. S., Beers, T. C., An, D., et al. "Formation and Evolution of the Disk System of the Milky Way: [α/Fe] Ratios and Kinematics of the SEGUE G–dwarf Sample". *ApJ*, 738:187, 2011. URL http://adsabs.harvard.edu/abs/2011ApJ...738..187L.

Lemaître, G. "Un Univers homogène de masse constante et de rayon croissant rendant compte de la vitesse radiale des nébuleuses extra-galactiques". *Annales de la Société Scientifique de Bruxelles*, 47:49–59, 1927. URL http://adsabs.harvard.edu/abs/1927ASSB...47...49L.

Lemaître, G. "The Beginning of the World from the Point of View of Quantum Theory". *Nature*, 127:706, 1931. URL http://adsabs.harvard.edu/abs/1931Natur.127..706L.

Liddle, A. and Loveday, J. *"The Oxford Companion to Cosmology"*. June 2009. URL http://adsabs.harvard.edu/abs/2009occ..book.....L.

Lora, V., Grebel, E. K., Sánchez-Salcedo, F. J., and Just, A. "Sextans' Cold Substructures as a Dynamical Judge: Core, Cusp, or MOND?". *ApJ*, 777:65, 2013. URL http://adsabs.harvard.edu/abs/2013ApJ...777...65L.

Lotz, J. M., Jonsson, P., Cox, T. J., and Primack, J. R. "The effect of mass ratio on the morphology and time-scales of disc galaxy mergers". *MNRAS*, 404:575–589, 2010. URL http://adsabs.harvard.edu/abs/2010MNRAS.404..575L.

Loveday, J., Peterson, B. A., Efstathiou, G., and Maddox, S. J. "The Stromlo-APM Redshift Survey. I – The luminosity function and space density of galaxies". *ApJ*, 390:338–344, 1992. URL http://adsabs.harvard.edu/abs/1992ApJ...390..338L.

Majewski, S. R., Skrutskie, M. F., Weinberg, M. D., and Ostheimer, J. C. "A Two Micron All Sky Survey View of the Sagittarius Dwarf Galaxy. I. Morphology of the Sagittarius Core and Tidal Arms". *ApJ*, 599:1082–1115, 2003. URL http://adsabs.harvard.edu/abs/2003ApJ...599.1082M.

Mark, J. W.-K. "The Spiral Wave of our Galaxy near Inner Lindblad Resonance". *Proceedings of the National Academy of Science*, 68:2095–2098, 1971. URL http://adsabs.harvard.edu/abs/1971PNAS...68.2095M.

Mark, J. W.-K. "On density waves in galaxies. I – Source terms and action conservation". *ApJ*, 193:539–559, 1974. URL http://adsabs.harvard.edu/abs/1974ApJ...193..539M.

Martig, M., Minchev, I., and Flynn, C. "Dissecting simulated disc galaxies – I. The structure of mono-age populations". *MNRAS*, 442:2474–2486, 2014. URL http://adsabs.harvard.edu/abs/2014MNRAS.442.2474M.

Martínez-Delgado, D., Butler, D. J., Rix, H.-W., et al. "The Closest View of a Dwarf Galaxy: New Evidence on the Nature of the Canis Major Overdensity". *ApJ*, 633: 205–209, 2005. URL http://adsabs.harvard.edu/abs/2005ApJ...633..205M.

McCarthy, I. G., Font, A. S., Crain, R. A., et al. "Global structure and kinematics of stellar haloes in cosmological hydrodynamic simulations". *MNRAS*, 420:2245–2262, 2012. URL http://adsabs.harvard.edu/abs/2012MNRAS.420.2245M.

Miller, R. H., Prendergast, K. H., and Quirk, W. J. "Numerical Experiments on Spiral Structure". *ApJ*, 161:903, 1970. URL http://adsabs.harvard.edu/abs/1970ApJ...161..903M.

Minchev, I., Famaey, B., Quillen, A. C., Dehnen, W., Martig, M., and Siebert, A. "Radial migration does little for Galactic disc thickening". *A&A*, 548:A127, 2012. URL http://adsabs.harvard.edu/abs/2012A%26A...548A.127M.

Minchev, I., Chiappini, C., and Martig, M. "Chemodynamical evolution of the Milky Way disk. II. Variations with Galactic radius and height above the disk plane". *A&A*, 572:A92, 2014. URL http://adsabs.harvard.edu/abs/2014A%26A...572A..92M.

Minniti, D. and Zoccali, M. "The Galactic bulge: a review". volume 245 of *IAU Symposium*, pages 323–332, 2008. URL http://adsabs.harvard.edu/abs/2008IAUS..245..323M.

Mo, H. J., Mao, S., and White, S. D. M. "The formation of galactic discs". *MNRAS*, 295:319–336, 1998. URL http://adsabs.harvard.edu/abs/1998MNRAS.295..319M.

Moetazedian, R. and Just, A. "Impact of cosmological satellites on the vertical heating of the Milky Way disc". *MNRAS*, 459:2905–2924, 2016. URL http://adsabs.harvard.edu/abs/2016MNRAS.459.2905M.

Moore, B., Ghigna, S., Governato, F., Lake, G., Quinn, T., Stadel, J., and Tozzi, P. "Dark Matter Substructure within Galactic Halos". *ApJ*, 524:L19–L22, 1999. URL http://adsabs.harvard.edu/abs/1999ApJ...524L..19M.

Moster, B. P., Macciò, A. V., Somerville, R. S., Johansson, P. H., and Naab, T. "Can gas prevent the destruction of thin stellar discs by minor mergers?". *MNRAS*, 403:1009–1019, 2010. URL http://adsabs.harvard.edu/abs/2010MNRAS.403.1009M.

Nagai, D. and Kravtsov, A. V. "The Radial Distribution of Galaxies in Σ Cold Dark Matter Clusters". *ApJ*, 618:557–568, 2005. URL http://adsabs.harvard.edu/abs/2005ApJ...618..557N.

Navarro, J. F., Frenk, C. S., and White, S. D. M. "Accretion of Satellite Galaxies and the Density of the Universe". *MNRAS*, 267:L1, 1994. URL http://adsabs.harvard.edu/abs/1994MNRAS.267L...1N.

Navarro, J. F., Frenk, C. S., and White, S. D. M. "A Universal Density Profile from Hierarchical Clustering". *ApJ*, 490:493–508, 1997. URL http://adsabs.harvard.edu/abs/1997ApJ...490..493N.

Ness, M., Freeman, K., Athanassoula, E., et al. "ARGOS – III. Stellar populations in the Galactic bulge of the Milky Way". *MNRAS*, 430:836–857, 2013. URL http://adsabs.harvard.edu/abs/2013MNRAS.430..836N.

Newberg, H. J., Yanny, B., Rockosi, C., et al. "The Ghost of Sagittarius and Lumps in the Halo of the Milky Way". *ApJ*, 569:245–274, 2002. URL http://adsabs.harvard.edu/abs/2002ApJ...569..245N.

Newton, I. *"Philosophiae Naturalis Principia Mathematica. Auctore Js. Newton"*. 1687. URL http://adsabs.harvard.edu/abs/1687pnpm.book.....N.

Noguchi, M. "Close encounter between galaxies. II - Tidal deformation of a disc galaxy stabilized by massive halo". *MNRAS*, 228:635–651, 1987. URL http://adsabs.harvard.edu/abs/1987MNRAS.228..635N.

Nordström, B., Mayor, M., Andersen, J., Holmberg, J., Pont, F., Jørgensen, B. R., Olsen, E. H., Udry, S., and Mowlavi, N. "The Geneva–Copenhagen survey of the Solar neighbourhood. Ages, metallicities, and kinematic properties of ≈14 000 F and G dwarfs". *A&A*, 418:989–1019, 2004. URL http://adsabs.harvard.edu/abs/2004A%26A...418..989N.

O'Dwyer, I. J., Eriksen, H. K., and Wandelt, B. D. e. a. "Bayesian Power Spectrum Analysis of the First–Year Wilkinson Microwave Anisotropy Probe Data". *ApJ*, 617:L99–L102, 2004. URL http://adsabs.harvard.edu/abs/2004ApJ...617L..99O.

Okamoto, T., Gao, L., and Theuns, T. "Mass loss of galaxies due to an ultraviolet background". *MNRAS*, 390:920–928, 2008. URL http://adsabs.harvard.edu/abs/2008MNRAS.390..920O.

Ostriker, J. P. and Peebles, P. J. E. "A Numerical Study of the Stability of Flattened Galaxies: or, can Cold Galaxies Survive?". *ApJ*, 186:467–480, 1973. URL http://adsabs.harvard.edu/abs/1973ApJ...186..467O.

Padmanabhan, T. *"Structure Formation in the Universe"*. Cambridge University Press, 1993. URL http://adsabs.harvard.edu/abs/1993sfu..book.....P.

Peebles, P. J. E. "Large-scale background temperature and mass fluctuations due to scale-invariant primeval perturbations". *ApJ*, 263:L1–L5, 1982. URL http://adsabs.harvard.edu/abs/1982ApJ...263L...1P.

Peebles, P. J. E. and Yu, J. T. "Primeval Adiabatic Perturbation in an Expanding Universe". *ApJ*, 162:815, 1970. URL http://adsabs.harvard.edu/abs/1970ApJ...162..815P.

Penzias, A. A. and Wilson, R. W. "A Measurement of Excess Antenna Temperature at 4080 Mc/s". *ApJ*, 142:419–421, 1965. URL http://adsabs.harvard.edu/abs/1965ApJ...142..419P.

Perryman, M. A. C., Lindegren, L., Kovalevsky, J., et al. "The HIPPARCOS Catalogue". *A&A*, 323:L49–L52, 1997. URL http://adsabs.harvard.edu/abs/1997A%26A...323L..49P.

Persic, M. and Salucci, P. "The baryon content of the universe". *MNRAS*, 258:14P–18P, 1992. URL http://adsabs.harvard.edu/abs/1992MNRAS.258P..14P.

Picaud, S. and Robin, A. C. "3D outer bulge structure from near infrared star counts". *A&A*, 428:891–903, 2004. URL http://adsabs.harvard.edu/abs/2004A%26A...428..891P.

Planck Collaboration, Ade, P. A. R., Aghanim, N., Alves, M. I. R., Armitage-Caplan, C., Arnaud, M., Ashdown, M., Atrio-Barandela, F., Aumont, J., Aussel, H., and et al. "Planck 2013 results. I. Overview of products and scientific results". *A&A*, 571:A1, 2014. URL http://adsabs.harvard.edu/abs/2014A%26A...571A...1P.

Planck Collaboration, Ade, P. A. R., Aghanim, N., and Arnaud, M. e. a. "Planck 2015 results. XIII. Cosmological parameters". *arXiv*, 2015. URL http://adsabs.harvard.edu/abs/2015arXiv150201589P.

Polyachenko, E. "Swing amplification and global modes reciprocity in models with cusps". *ArXiv e-prints, accepted to Baltic Astronomy*, 2016. URL http://adsabs.harvard.edu/abs/2016arXiv160801776P.

Polyachenko, E. V. "The eigenvalue problem for integrable gravitating systems with application to galactic discs". *MNRAS*, 357:559–564, 2005. URL http://adsabs.harvard.edu/abs/2005MNRAS.357..559P.

Polyachenko, E. V., Berczik, P., and Just, A. "On the bar formation mechanism in galaxies with cuspy bulges". *MNRAS*, 2016. URL http://adsabs.harvard.edu/abs/2016MNRAS.tmp.1036P.

Press, W. H., Teukolsky, S. A., Vetterling, W. T., and Flannery, B. P. *"Numerical Recipes in C (2Nd Ed.): The Art of Scientific Computing"*. Cambridge University Press, New York, NY, USA, 1992.

Quillen, A. C., Minchev, I., Bland-Hawthorn, J., and Haywood, M. "Radial mixing in the outer Milky Way disc caused by an orbiting satellite". *MNRAS*, 397:1599–1606, 2009. URL http://adsabs.harvard.edu/abs/2009MNRAS.397.1599Q.

Quinn, P. J. and Goodman, J. "Sinking satellites of spiral systems". *ApJ*, 309:472–495, 1986. URL http://adsabs.harvard.edu/abs/1986ApJ...309..472Q.

Quinn, P. J., Hernquist, L., and Fullagar, D. P. "Heating of galactic disks by mergers". *ApJ*, 403:74–93, 1993. URL http://adsabs.harvard.edu/abs/1993ApJ...403...74Q.

Read, J. I., Lake, G., Agertz, O., and Debattista, V. P. "Thin, thick and dark discs in ΣCDM". *MNRAS*, 389:1041–1057, 2008. URL http://adsabs.harvard.edu/abs/2008MNRAS.389.1041R.

Reed, B. C. "Evidence for a Warped Distribution of OB Stars in the Southern Milky Way". *AJ*, 111:804, 1996. URL http://adsabs.harvard.edu/abs/1996AJ....111..804R.

Reid, M. J., Menten, K. M., and Brunthaler, A. e. a. "Trigonometric Parallaxes of High Mass Star Forming Regions: The Structure and Kinematics of the Milky Way". *ApJ*, 783:130, 2014. URL http://adsabs.harvard.edu/abs/2014ApJ...783..130R.

Riess, A. G., Filippenko, A. V., and Challis, P. e. a. "Observational Evidence from Supernovae for an Accelerating Universe and a Cosmological Constant". *AJ*, 116:1009–1038, 1998. URL http://adsabs.harvard.edu/abs/1998AJ....116.1009R.

Robertson, H. P. "On the Foundations of Relativistic Cosmology". *Proceedings of the National Academy of Science*, 15:822–829, 1929. URL http://adsabs.harvard.edu/abs/1929PNAS...15..822R.

Rojas-Arriagada, A., Recio-Blanco, A., Hill, V., et al. "The Gaia–ESO Survey: metallicity and kinematic trends in the Milky Way bulge". *A&A*, 569:A103, 2014. URL http://adsabs.harvard.edu/abs/2014A%26A...569A.103R.

Ruchti, G. R., Read, J. I., and Feltzing, S. e. a. "The Gaia–ESO Survey: a quiescent Milky Way with no significant dark/stellar accreted disc". *MNRAS*, 450:2874–2887, 2015. URL http://adsabs.harvard.edu/abs/2015MNRAS.450.2874R.

Sachs, R. K. and Wolfe, A. M. "Perturbations of a Cosmological Model and Angular Variations of the Microwave Background". *ApJ*, 147:73, 1967. URL http://adsabs.harvard.edu/abs/1967ApJ...147...73S.

Schechter, P. "An analytic expression for the luminosity function for galaxies.". *ApJ*, 203:297–306, 1976. URL http://adsabs.harvard.edu/abs/1976ApJ...203..297S.

Seabroke, G. M. and Gilmore, G. "Revisiting the relations: Galactic thin disc age–velocity dispersion relation". *MNRAS*, 380:1348–1368, 2007. URL http://adsabs.harvard.edu/abs/2007MNRAS.380.1348S.

Sellwood, J. A. "Most Real Bars are Not Made by the Bar Instability". volume 197 of *Astronomical Society of the Pacific Conference Series*, page 3, 2000. URL http://adsabs.harvard.edu/abs/2000ASPC..197....3S.

Sellwood, J. A. "Relaxation in N-body Simulations of Disk Galaxies". *ApJ*, 769: L24, 2013. URL http://adsabs.harvard.edu/abs/2013ApJ...769L..24S.

Sellwood, J. A. "Secular evolution in disk galaxies". *RvMP*, 86:1–46, 2014. URL http://adsabs.harvard.edu/abs/2014RvMP...86....1S.

Sellwood, J. A., Nelson, R. W., and Tremaine, S. "Resonant Thickening of Disks by Small Satellite Galaxies". *ApJ*, 506:590–599, 1998. URL http://adsabs.harvard.edu/abs/1998ApJ...506..590S.

Sérsic, J. L. *"Atlas de galaxias australes"*. 1968. URL http://adsabs.harvard.edu/abs/1968adga.book.....S.

Siegel, M. H., Majewski, S. R., Reid, I. N., and Thompson, I. B. "Star Counts Redivivus. IV. Density Laws through Photometric Parallaxes". *ApJ*, 578:151–175, 2002. URL http://adsabs.harvard.edu/abs/2002ApJ...578..151S.

Silk, J. "Fluctuations in the Primordial Fireball". *Nature*, 215:1155–1156, 1967. URL http://adsabs.harvard.edu/abs/1967Natur.215.1155S.

Sinha, R. P. "Survey of neutral hydrogen in the galactic center region". *A&A*, 37:403–463, 1979. URL http://adsabs.harvard.edu/abs/1979A%26AS...37..403S.

Smith, B. J., Price, S. D., and Baker, R. I. "The COBE DIRBE Point Source Catalog". *ApJ*, 154:673–704, 2004. URL http://adsabs.harvard.edu/abs/2004ApJS..154..673S.

Smoot, G. F., Bennett, C. L., and Kogut, A. e. a. "Structure in the COBE differential microwave radiometer first-year maps". *ApJ*, 396:L1–L5, 1992. URL http://adsabs.harvard.edu/abs/1992ApJ...396L...1S.

Somerville, R. S. and Davé, R. "Physical Models of Galaxy Formation in a Cosmological Framework". *ARA&A*, 53:51–113, 2015. URL http://adsabs.harvard.edu/abs/2015ARA%26A..53...51S.

Sommer-Larsen, J., Götz, M., and Portinari, L. "Galaxy Formation: Cold Dark Matter, Feedback, and the Hubble Sequence". *ApJ*, 596:47–66, 2003. URL http://adsabs.harvard.edu/abs/2003ApJ...596...47S.

Sparke, L. S. and Gallagher, J. S., III. *"Galaxies in the Universe – 2nd Edition"*. Cambridge University Press, 2007. URL http://adsabs.harvard.edu/abs/2007gaun.book.....S.

Spriangel, V. "E pur si muove: Galilean–invariant cosmological hydrodynamical simulations on a moving mesh". *MNRAS*, 401:791–851, 2010. URL http://adsabs.harvard.edu/abs/2010MNRAS.401..791S.

Springel, V. "The cosmological simulation code GADGET–2". *MNRAS*, 364:1105–1134, 2005. URL http://adsabs.harvard.edu/abs/2005MNRAS.364.1105S.

Springel, V. "Smoothed Particle Hydrodynamics in Astrophysics". *ARA&A*, 48:391–430, 2010. URL http://adsabs.harvard.edu/abs/2010ARA%26A..48..391S.

Springel, V., White, S. D. M., Tormen, G., and Kauffmann, G. "Populating a cluster of galaxies – I. Results at [formmu2]z=0". *MNRAS*, 328:726–750, 2001. URL http://adsabs.harvard.edu/abs/2001MNRAS.328..726S.

Springel, V., Di Matteo, T., and Hernquist, L. "Modelling feedback from stars and black holes in galaxy mergers". *MNRAS*, 361:776–794, 2005a. URL http://adsabs.harvard.edu/abs/2005MNRAS.361..776S.

Springel, V., White, S. D. M., Jenkins, A., et al. "Simulations of the formation, evolution and clustering of galaxies and quasars". *Nature*, 435:629–636, 2005b. URL http://adsabs.harvard.edu/abs/2005Natur.435..629S.

Springel, V., Wang, J., Vogelsberger, M., Ludlow, A., Jenkins, A., Helmi, A., Navarro, J. F., Frenk, C. S., and White, S. D. M. "The Aquarius Project: the subhaloes of galactic haloes". *MNRAS*, 391:1685–1711, 2008. URL http://adsabs.harvard.edu/abs/2008MNRAS.391.1685S.

Steinmetz, M. "Numerical Simulations of Galaxy Formation". *Astrophysics & Space Science*, 269:513–532, 1999. URL http://adsabs.harvard.edu/abs/1999Ap%26SS.269..513S.

Steinmetz, M., Zwitter, T., Siebert, A., et al. "The Radial Velocity Experiment (RAVE): First Data Release". *AJ*, 132:1645–1668, 2006. URL http://adsabs.harvard.edu/abs/2006AJ....132.1645S.

Stewart, K. R., Bullock, J. S., Wechsler, R. H., Maller, A. H., and Zentner, A. R. "Merger Histories of Galaxy Halos and Implications for Disk Survival". *ApJ*, 683: 597–610, 2008. URL http://adsabs.harvard.edu/abs/2008ApJ...683..597S.

Sunyaev, R. A. and Zeldovich, Y. B. "Small-Scale Fluctuations of Relic Radiation". *Ap&SS*, 7:3–19, 1970. URL http://adsabs.harvard.edu/abs/1970Ap%26SS...7....3S.

Teyssier, R. "RAMSES: A new N–body and hydrodynamical code". Astrophysics Source Code Library, 2010. URL http://adsabs.harvard.edu/abs/2010ascl.soft11007T.

Toomre, A. "What amplifies the spirals". In *Structure and Evolution of Normal Galaxies*, pages 111–136, 1981. URL http://adsabs.harvard.edu/abs/1981seng.proc..111T.

Toomre, A. "Theories of WARPS". In *Internal Kinematics and Dynamics of Galaxies*, volume 100 of *IAU Symposium*, pages 177–185, 1983. URL http://adsabs.harvard.edu/abs/1983IAUS..100..177T.

Toomre, A. and Toomre, J. "Galactic Bridges and Tails". *ApJ*, 178:623–666, 1972. URL http://adsabs.harvard.edu/abs/1972ApJ...178..623T.

Torbet, E., Devlin, M. J., and Dorwart, W. B. e. a. "A Measurement of the Angular Power Spectrum of the Microwave Background Made from the High Chilean Andes". *ApJ*, 521:L79–L82, 1999. URL http://adsabs.harvard.edu/abs/1999ApJ...521L..79T.

Tóth, G. and Ostriker, J. P. "Galactic disks, infall, and the global value of Omega". *ApJ*, 389:5–26, 1992. URL http://adsabs.harvard.edu/abs/1992ApJ...389....5T.

Valenti, E., Zoccali, M., Gonzalez, O. A., et al. "Stellar density profile and mass of the Milky Way bulge from VVV data". *A&A*, 587:L6, 2016. URL http://adsabs.harvard.edu/abs/2016A%26A...587L...6V.

van den Bergh, S., Abraham, R. G., Ellis, R. S., et al. "A Morphological Catalog of Galaxies in the Hubble deep Field". *AJ*, 112:359, 1996. URL http://adsabs.harvard.edu/abs/1996AJ....112..359V.

van der Marel, R. P., Besla, G., Cox, T. J., et al. "The M31 Velocity Vector. III. Future Milky Way M31–M33 Orbital Evolution, Merging, and Fate of the Sun". *ApJ*, 753:9, 2012. URL http://adsabs.harvard.edu/abs/2012ApJ...753...9V.

Velázquez, H. and White, S. D. M. "Sinking satellites and the heating of galaxy discs". *MNRAS*, 304:254–270, 1999. URL http://adsabs.harvard.edu/abs/1999MNRAS.304..254V.

Vera-Ciro, C., D'Onghia, E., Navarro, J., and Abadi, M. "The Effect of Radial Migration on Galactic Disks". *ApJ*, 794:173, 2014. URL http://adsabs.harvard.edu/abs/2014ApJ...794..173V.

Vesperini, E. and Weinberg, M. D. "Perturbations of Spherical Stellar Systems during Flyby Encounters". *ApJ*, 534:598–623, 2000. URL http://adsabs.harvard.edu/abs/2000ApJ...534..598V.

Villalobos, Á. and Helmi, A. "Simulations of minor mergers - I. General properties of thick discs". *MNRAS*, 391:1806–1827, 2008. URL http://adsabs.harvard.edu/abs/2008MNRAS.391.1806V.

Villalobos, Á., Kazantzidis, S., and Helmi, A. "Thick–disk Evolution Induced by the Growth of an Embedded Thin Disk". *ApJ*, 718:314–330, 2010. URL http://adsabs.harvard.edu/abs/2010ApJ...718..314V.

Vogelsberger, M., Genel, S., Springel, V., Torrey, P., Sijacki, D., Xu, D., Snyder, G., Nelson, D., and Hernquist, L. "Introducing the Illustris Project: simulating the coevolution of dark and visible matter in the Universe". *MNRAS*, 444:1518–1547, 2014. URL http://adsabs.harvard.edu/abs/2014MNRAS.444.1518V.

Wadsley, J. W., Stadel, J., and Quinn, T. "Gasoline: a flexible, parallel implementation of TreeSPH". *New Astronomy*, 9:137–158, 2004. URL http://adsabs.harvard.edu/abs/2004NewA....9..137W.

Wainscoat, R. J., Freeman, K. C., and Hyland, A. R. "The optical and near-infrared distribution of light in the edge-on galaxy IC 2531". *ApJ*, 337:163–190, 1989. URL http://adsabs.harvard.edu/abs/1989ApJ...337..163W.

Walker, A. G. "On the formal comparison of Milne's kinematical system with the systems of general relativity". *MNRAS*, 95:263–269, 1935. URL http://adsabs.harvard.edu/abs/1935MNRAS..95..263W.

Walker, I. R., Mihos, J. C., and Hernquist, L. "Quantifying the Fragility of Galactic Disks in Minor Mergers". *ApJ*, 460:121, 1996. URL http://adsabs.harvard.edu/abs/1996ApJ...460..121W.

Watkins, L. L., Evans, N. W., Belokurov, V., et al. "Substructure revealed by RRLyraes in SDSS Stripe 82". *MNRAS*, 398:1757–1770, 2009. URL http://adsabs.harvard.edu/abs/2009MNRAS.398.1757W.

Weiland, J. L., Arendt, R. G., Berriman, G. B., et al. "COBE diffuse infrared background experiment observations of the galactic bulge". *ApJ*, 425:L81–L84, 1994. URL http://adsabs.harvard.edu/abs/1994ApJ...425L..81W.

White, S. D. M. and Rees, M. J. "Core condensation in heavy halos – A two–stage theory for galaxy formation and clustering". *MNRAS*, 183:341–358, 1978. URL http://adsabs.harvard.edu/abs/1978MNRAS.183..341W.

Widrow, L. M. “Distribution Functions for Cuspy Dark Matter Density Profiles”. *ApJS*, 131:39–46, 2000. URL http://adsabs.harvard.edu/abs/2000ApJS..131...39W.

Widrow, L. M., Pym, B., and Dubinski, J. ”Dynamical Blueprints for Galaxies”. *ApJ*, 679:1239–1259, 2008. URL http://adsabs.harvard.edu/abs/2008ApJ...679.1239W.

Woods, D. F. and Geller, M. J. “Minor Galaxy Interactions: Star Formation Rates and Galaxy Properties”. *AJ*, 134:527–540, 2007. URL http://adsabs.harvard.edu/abs/2007AJ....134..527W.

Woods, D. F., Geller, M. J., and Barton, E. J. “Tidally Triggered Star Formation in Close Pairs of Galaxies: Major and Minor Interactions”. *AJ*, 132:197–209, 2006. URL http://adsabs.harvard.edu/abs/2006AJ....132..197W.

Xu, Y., Newberg, H. J., Carlin, J. L., et al. ”Rings and Radial Waves in the Disk of the Milky Way”. *ApJ*, 801:105, 2015. URL http://adsabs.harvard.edu/abs/2015ApJ...801..105X.

Xue, X.-X., Rix, H.-W., Ma, Z., et al. “The Radial Profile and Flattening of the Milky Way’s Stellar Halo to 80 kpc from the SEGUE K–giant Survey”. *ApJ*, 809: 144, 2015. URL http://adsabs.harvard.edu/abs/2015ApJ...809..144X.

Yanny, B., Rockosi, C., Newberg, H. J., et al. ”SEGUE: A Spectroscopic Survey of 240,000 Stars with g = 14–20”. *AJ*, 137:4377–4399, 2009. URL http://adsabs.harvard.edu/abs/2009AJ....137.4377Y.

York, D. G., Adelman, J., Anderson, J. E., Jr., et al. ”The Sloan Digital Sky Survey: Technical Summary”. *AJ*, 120:1579–1587, 2000. URL http://adsabs.harvard.edu/abs/2000AJ....120.1579Y.

Yurin, D. and Springel, V. “An iterative method for the construction of N–body galaxy models in collisionless equilibrium”. *MNRAS*, 444:62–79, 2014. URL http://adsabs.harvard.edu/abs/2014MNRAS.444...62Y.

Zaritsky, D. and Rix, H.-W. ”Lopsided Spiral Galaxies and a Limit on the Galaxy Accretion Rate”. *ApJ*, 477:118–127, 1997. URL http://adsabs.harvard.edu/abs/1997ApJ...477..118Z.

Zinchenko, I. A., Berczik, P., Grebel, E. K., et al. ”On the Influence of Minor Mergers on the Radial Abundance Gradient in Disks of Milky–Way–like Galaxies”. *ApJ*, 806:267, 2015. URL http://adsabs.harvard.edu/abs/2015ApJ...806..267Z.

Zoccali, M., Lecureur, A., Barbuy, B., et al. “Oxygen abundances in the Galactic bulge: evidence for fast chemical enrichment”. *A&A*, 457:L1–L4, 2006. URL http://adsabs.harvard.edu/abs/2006A%26A...457L...1Z.

Zwicky, F. “Die Rotverschiebung von extragalaktischen Nebeln”. *Helvetica Physica Acta*, 6:110–127, 1933. URL http://adsabs.harvard.edu/abs/1933AcHPh...6..110Z.